UNIVERSITY OF CALIFORNIA
RIVERSIDE

Probing Properties and Mechanisms of Protons in Materials and Interfaces for Energy Storage Systems Using First-Principles Methodology

A Dissertation submitted in partial satisfaction
of the requirements for the degree of

Doctor of Philosophy

in

Chemical and Environmental Engineering

by

Lihua Xu

June 2020

Dissertation Committee:
Dr. De-en Jiang, Co-Chairperson
Dr. Juchen Guo, Co-Chairperson
Dr. Jianzhong Wu

The Dissertation of Lihua Xu is approved:

_____

_____

Committee Co-Chairperson

_____

Committee Co-Chairperson

University of California, Riverside

COPYRIGHT ACKNOWLEDGEMENT

The text and figures in Chapter 3, in part or full, are a reprint of the materials from "Understanding Hydrogen in Perovskites from First Principles", *Computational Materials Science*, 2020, 174, 109461 by Lihua Xu, and De-en Jiang. The co-author (Dr. De-en Jiang) directed and supervised the research that forms the basis of this chapter.

The text and figures in Chapter 4, in part or full, are a reprint of the materials from "First Principles Insights into the Heterostructures of MXene and TiO_2" (*In preparation*), by Lihua Xu, De-en Jiang, and et al. The co-author (Dr. De-en Jiang) directed and supervised the research that forms the basis of this chapter.

The text and figures in Chapter 5, in part or full, are a reprint of the materials from "Proton Dynamics and Interfacial Properties in Single Water Layer Confined by Graphene-MXene and MXene-MXene" (*In preparation*), Lihua Xu, De-en Jiang, and et al. The co-author (Dr. De-en Jiang) directed and supervised the research that forms the basis of this chapter.

ACKNOWLEDGMENTS

This is the most challenging part for me in this dissertation because I cannot express my greatest appreciation with few words to all the people who helped me during my 4-year Ph.D. research as well as career journey.

First and foremost, I would like to express my sincere gratitude to my advisor, Prof. De-en Jiang, for invaluable guidance, great supervision, and continuous support during my research studies. Without him, my research and this thesis would not have come to fruition and possible. I would also like to thank my committee members, Dr. Juchen Guo for constructive comments and suggestions during my research proposal defense, and Dr. Jianzhong Wu for helping me explore the field of engineering chemistry. Thank you to many professors who inspired and encouraged me at the University of California, Riverside, Dr. Jinyong Liu, Dr. Alex Greaney, Dr. Kelley C. Barsanti, and Dr. Ian Wheeldon.

I would also like to pay my respects to each and every member of "The Computational Materials Chemistry" Group for a variety of knowledge and immense assistance with presentations, researches, papers, and posters. I would like to thank Yangyunli Sun, and Victor Fung for all the help when I had technical problems regarding research mechanisms and calculations. A special thanks to Kristen Wang for her generous help outside research, my oral English, and being always giving ear to me. For helping to solve millions of problems and bouncing countless ideas back and forth, I would like to

thank all my group members. Furthermore, I would like to thank Prof. De-en Jiang again for providing such a wonderful and healthy group atmosphere, and I really enjoyed my researches and all kinds of group-retreats.

In addition, I would like to thank Dr. Niranjan Vasant Ilawe and Sarah I. Allec for the unparalleled guidance and encouragement during the initial two years of my graduate journey when I was introduced to the field of quantum theories and calculations. For helping me tackle numerous coding problems and offering immeasurable help in understanding computational methodologies, I would like to give Dr. Chao Lian and Zulfikhar A. Ali an earnest acknowledgment. I want to thank Sharmishta Bardhan for her kind introduction to the area of applying machine learning (ML) algorithms to handle environmental chemistry issues. Likewise, I am grateful to all my friends with years-of-loyalty for their company and supports.

Furthermore, I want to deliver my sincere appreciations for the financial support from the University of California, Riverside and Fluid Interface Reactions, Structures, and Transport (FIRST) Center, an Energy Frontier Research Center funded by the U.S. Department of Energy (DOE), Office of Science, Office of Basic Energy Sciences. I would also like to thank the computational resource from the National Energy Research Scientific Computing Center (NERSC). Finally, my heartful appreciations will be given to my parents and my identical twin sister (with whom I shared so much growing up) for their constant encouragement and everything they provide. It has been bumpy at times, but their confidence in me has enhanced my ability to get through it all and succeed in the end. Last but not least, my sincere acknowledgment is going to my boyfriend, Chao Yi, for his

unconditional support and love through the ups and downs during my graduate journey. Thanks for *everything* that helped me get to this day.

DEDICATED TO

My parents, Weidong Xu and Haitao Zhou for making me who I am.

My twin sister, Lijing Xu for constant encouragement and support.

And all my family members for the love and confidence in me.

ABSTRACT OF THE DISSERTATION

Probing Properties and Mechanisms of Protons in Materials and Interfaces for Energy Storage Systems Using First-Principles Methodology

by

Lihua Xu

Doctor of Philosophy, Graduate Program in Chemical and Environmental Engineering,
University of California, Riverside, June 2020
Dr. De-en Jiang, Co-Chairperson
Dr. Juchen Guo, Co-Chairperson

The fast progress in renewable energy sources, emerging electronics, and electrical automobiles stimulate the development of next-generation energy storage devices. Among them, supercapacitors, possessing high power and high energy density, caught rabid attention worldwide. Theoretical studies on the electrode compositions, geometries, and interfaces delivered useful information on various material properties, which was essential for approaching high-performance supercapacitors. Recent computational screening techniques suggest potential electrode materials for future experimental designs and device fabrications. So far, transition metal oxides (TMO), carbon-based materials, and the newly discovered 2D MXenes, etc. were regarded as the promising supercapacitor electrodes due

to their high theoretical capacitance, larger surface areas, and multiple constituents. In the first part of this dissertation, density functional theory (DFT) was employed to analyze the structure, energetics, and transport of hydrogen in 3d/4d transition metal perovskites (ABO_3). The B-O bonding contributions before and after H absorption were unveiled. While simple chemical descriptors, allowing comprehensive searches for candidate proton-conductor perovskites with little computational cost, were provided. Likewise, the interfacial properties for the heterostructures MXene ($Ti_3C_2T_x$ and Ti_2CT_x with T=-O, -OH, a mixture of -F and -O)/(pure or N-doped) anatase-TiO_2 (101) were evaluated via DFT. We found that surface functional groups of MXene dramatically impacted the interfacial electronic charge transfers and interfacial configurations. In addition, the N-doped surface-O of TiO_2 changed the electronic and geometric properties of these hybrid composites. Besides basic understandings of various material properties, perceiving energy storage mechanisms behind different types of supercapacitors is also a welcoming topic. In the second part of this dissertation, *ab-initio* molecular dynamics (AIMD) were utilized to study the proton transport performances at the mono water layer confined by Graphene-$Ti_3C_2O_2$ (dissimilar interface) and $Ti_3C_2O_2$-$Ti_3C_2O_2$ (similar interface) with different intercalated-proton concentrations. The results showed that interfacial properties, as well as proton diffusion behavior, played a significant role in the faster proton surface-redox and transport process. Ultimately, this dissertation explores the fundamental knowledge of the recent sprout popular metal-oxides (perovskites), MXene-based composite electrode materials for supercapacitor applications. Meanwhile, we offered a theoretical

interpretation of energy storage mechanisms for proton intercalated MXene-based layered interfaces.

Table of Contents

List of Figures

List of Tables

Chapter 1

Introduction

1.1 Motivations

Nowadays, theoretical computational studies have been extensively applied in tremendous researches. Theoretical simulations not only can provide deep understandings or explanations to material properties at the micro-, nano-, or atom-sized level, but also can make predictions of physical (or chemical) properties as well as active processes on various materials and mechanisms. Thereby, computational work, to some extent, can help guide future experimental researches. In this way, a significant amount of time, energetics, and costs can be saved during experimental investigations and designs. Owning to the fast development of computer hardware and advanced numerical algorithms, continuous and enormous efforts have been dedicated to boosting and promoting the development of

computational tools. Particularly, over the past century, a noticeable amount of progress has been made to quantum chemical tools in providing theoretical supports in almost all scientific areas (chemistry, physics, biology,[1–3] etc.).

There was a long developing history for quantum simulation techniques. From the perspective of methodologies, we have wave-function based and electron-density based methods. Currently, semi-empirical and *ab-initio* quantum simulation approaches play critical roles in modern computational chemistry. To improve the accuracy in describing electron/molecular interactions, etc., many energy corrections, parameters, and additional functional terms were involved in quantum theories. Based on this, various codes were produced to make quantum simulation packages address more specific chemical/physical systems. Thus, a wide range of matter from electron to atom, from molecules to crystals, from the surface (interface) to bulk, from liquid to solid-state, etc., can be examined. Besides, through mimicking experimental ambiance, the dynamic motion, or the chemical reactions of molecules/atoms can also be modeled via computational simulations.

So far, among all the quantum chemical techniques used, density functional theory (DFT) has been argued as one of the most accurate and efficient approaches for predicting electronic properties. Thousands of publications can be found online regarding the use of DFT to investigate the electronic and thermodynamic properties of different crystal compositions,[4,5] the conformation-screening of certain nano-materials[6–8] and biomaterials (e.g. peptides[9]), the transition-state or transition-pathway search of surface catalyst reactions,[10,11] etc. However, there are still some concrete shortcomings of DFT methods — the most-mentioned one is the extremely high computational cost for large-scale systems

(LSS), especially, the biosystem or polymers containing long molecular chains with hundreds or thousands of atoms.

The industrial revolution shapes the modern world. The intensive use of fossil fuels as the primary energy source has caused many issues, such as environmental pollutions, and the global greenhouse effect, etc. Moreover, they are not sustainable, which leads to today's energy crises. To replace those traditional energy sources, environmental-friendly renewable energy technologies from hydropower, tidal, wind power, solar energy, and geothermal were developed. To store these energies, it is essential to create energy storage materials and devices with long-lifetime, high-energy and high-power densities. Meanwhile, the enormous potential market for technology including electric vehicles, portable and wearable electronic devices, and smart grids. also simulates the demands for more advanced power storage devices. For further promoting performances of present energy storage systems, creating the next generation energy storage materials has become an exceedingly popular topic in recent decades. However, basic understandings of the mechanisms and properties for these energy storage systems is still elusive (details will be pointed out in the subsequent section 1.2). In addition to tremendous efforts from experimental trials, computational methods have been applied to understand the rationales behind phenomena such as charge transfer behavior and particle transfer phenomenon. In return, they also provide insights to achieve effective experimental layouts.

In this dissertation, I used DFT methods to explore a series of properties of two potential capacitor materials — perovskites and MXene-based composites. The proton

transport mechanisms in the single water layer confined by MXene-based layered interfaces were also investigated.

1.2 Background Introduction

1.2.1 Energy storage systems

To effectively store renewable energy, vast attention has been focused on the new-generation high-performance electrochemical energy storage (EES) devices. There are two primary EES: one is the battery, and the other is the electrochemical capacitor (EC). The major differences between them are the charging processes and device structure designs. For batteries, the charging behavior is mainly by bulk intercalations or redox reactions. They usually have very high-energy-density. ECs, on the other hand, store energy primarily by electrode surface ion-adsorption or redox/intercalation reactions, and usually, they have a good power density.[12] Thanks to the hybridization approach[13] and extensive usage of nano-level design strategies, the demarcation between batteries and ECs become more and more ambiguous. Scientists are devoted to obtaining devices, like capacitors, with a combination of both high-energy density and high-power delivery. The terminology used to describe these devices is “supercapacitors” (SCs).

Supercapacitors store energy either by the formation of electrical double layer at the electrodes (or electrolyte interface), typically known as the electric double-layer capacitor (EDLC) or by the pseudo-capacitance mechanism.[14] In the next section, we will describe these two types of charge storage concepts. Here, it is worth mentioning that pseudo-capacitors outperform EDLCs in energy density, particularly about tens of times

greater in electronic charging storage. Furthermore, pseudo-capacitors display superior properties of high-specific conductivity, cyclic stability, faster charge-discharge responses, etc. As forecasted by numerous market and economic investigations, the global supercapacitors market is expected to witness significant growth over the following decades. In 2019, the market price was about $834 million, and it is expected to reach ~$2664 million by 2025 with a CAGR (compound annual growth rate) of more than 20% during 2020-2025.[15]

To further improve the efficiency and performance of supercapacitors, the understandings of material properties, as well as the underlying energy storage mechanisms, would be the central tasks at this moment. Fortunately, various experimental and theoretical scientists have already been in these fields.

1.2.2 Structure of the typical supercapacitors

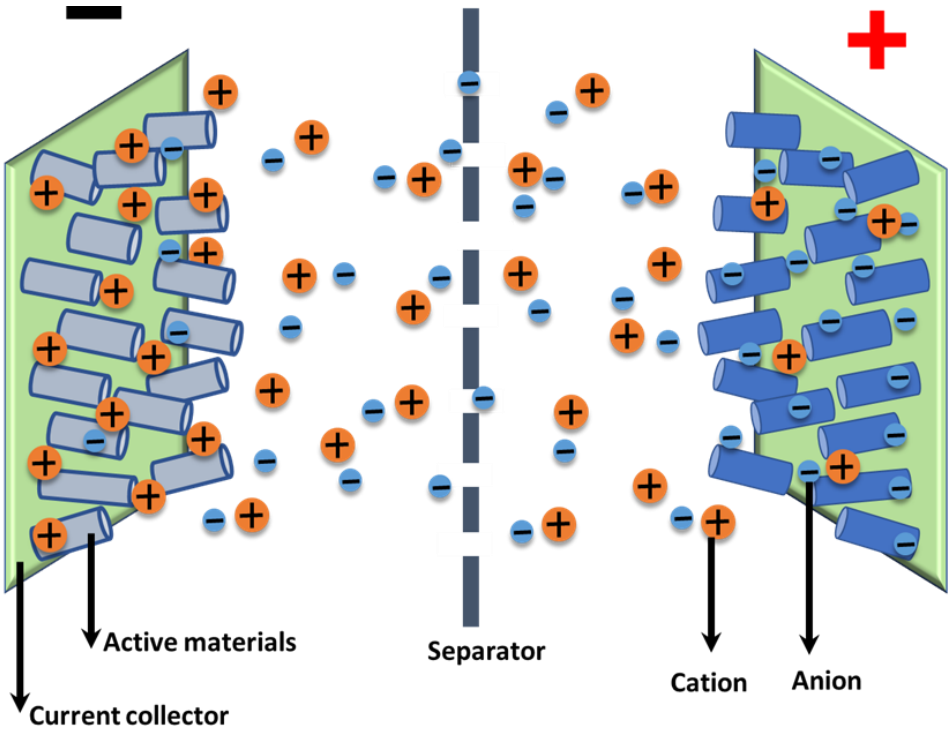

Figure 1.1 Configuration diagram illustration of a typical supercapacitor.

Figure 1.1 is the configuration illustration of a typical supercapacitor. A pair of parallel-plate working electrodes are comprised of active materials deposited on current collectors. These two electrodes are isolated by an electrolyte (cations and ions) solution and an ion-permeable membrane separator.

For EDLCs, the charge storage mechanism is relying on the physical adsorption/desorption processes of the electrolyte ions at the electrode interface.[16] The resultant capacitor performance is highly dependent on accessible surface regions of the electrodes.[14] Hundreds of multi-dimensional materials were under explorations to increase the specific surface areas (SSA). Though some of these materials (mainly the carbon-based

electrode materials like the carbon nanotubes, active carbon, graphene, carbon composites, etc.) have been commercialized, the adsorption/desorption physical processes are prolonged in terms of ion partitioning and device packing.[17] On the contrary to EDLCs, chemical processes dominate the energy storage mechanisms of pseudo-capacitors. More specifically, the chemical processes involve reversible redox reactions on interfaces or reversible ion (protons, metal/molecular ions, etc.) intercalation/de-intercalation in electrodes (e.g. bulk crystal, layered structures).

Among all materials utilized for supercapacitors applications, carbon-based materials, transition metal oxide (TMO), hydroxide, and conductive polymers, etc. are the most extensively studied categories until now. Also, creating and searching for more appropriate electrode materials is a core mission toward our final goal.

1.2.3 Transition metal oxide (TMO) based materials

Transition metal oxides[18,19] (TMO) are broadly studied in many fields since their abundant reserves and easy approachability. TMOs (e.g. RuO_2, MnO_2, Co_3O_4) are deemed as promising supercapacitor materials due to the intriguing characteristics, such as excellent energy output, high theoretical specific capacitance, larger surface area, and multiple constituents. Despite this, they also have their restrictions (e.g. MnO_2: poor ionic and electrical conductivities;[20] RuO_2: agglomeration of particles[21]) that hamper their performance in supercapacitors. To overcome these limitations, various metal-oxide based composites have been produced. It is noteworthy that different preparation methods may also lead to vastly deviated capacitor performance.[17]

Charitra et al. employed a hydrothermal method to prepare hydrous RuO_2 with multi-walled carbon nanotubes and reported a high specific capacitance of up to 1585 F/g.[22] Jhao et al. found that co-axial RuO_x/graphene nanofibers (GNF) allowed more electrolyte ions to diffuse into the inner active sites while maintaining a high areal capacitance 53.76 mF/cm^2 and good cycling stability 83% after 5000 cycles.[23] Via electrodeposition preparation of Co_3O_4-MnO_2-NiO ternary hybrid nanotubes, Singh et al. reported an excellent capacitor performance 2525 F/g because of the fast ion penetration through well-aligned tubes.[24] Guo et al. fabricated electrodes based on porous gully-network Co_3O_4 nanowires (NW) directly grown on Ni foams.[25] With the advantages of large surface area, open channels for ion transport, volume-change adaptability during electrochemical reactions, the capacity performance improved greatly as the specific capacity goes to 582.8 C/g at 1 A/g and 93.1% capacity retained over 25000 cycles. Many recent reviews have given comprehensive summaries on metal-oxide based materials,[16,17,19,26] and numerous researches are still ongoing. Moreover, by different chemical manipulations: i) element doping;[27–29] ii) oxygen deficiency,[30–32] the enhancement of capacitor performance can also be achieved.

Perovskite oxides (ABO_3) containing 3d or 4d transition metals are also potential electrode materials. They have many unique properties, such as electrochemical and thermal stability, high conductivity, ferromagnetism phenomenon, and pyroelectric effect. Studies on using perovskite oxides as the anode for supercapacitors sprout up after the year 2014 when Mefford et al. unveiled the charge storage process via oxygen-anion-intercalation in $LaMnO_3$.[33]

Besides these TMO related materials, new 2D transition metal carbides, nominally MXene, have come into sight over the last couple of years.

1.2.4 2D transition metal carbides/nitrides (MXene)

The frequently mentioned two-dimensional (2D) materials — graphene, is known to possess outstanding properties and has been applied in various research areas.[34] Over the years, many new 2D materials have been developed. MXenes, discovered in 2011,[35] has emerged as a fantastic 2D layered materials and captured considerable attention in diverse scientific aspects.[36] MXenes are mainly composed of transition metal carbides, nitrides or carbonitrides with a general formula $M_{n+1}X_nT_x$ (M = d-block transition metal, e.g., Ti, Mo, Nb; n = 1,2, or 3; X = N and/or C; T = surface functional groups, e.g., -O, -OH, -F, -Cl). They are synthesized via selective chemical etching the "A"-group element from the MAX (the parent ternary carbide or nitride with "A" being the element in group IIIA or IVA) phases, e.g., $Ti_3AlC_2 \rightarrow Ti_3C_2T_x$ (layered MAX →2D MXene).[35,37–39]

Owning to the attractive feature-combination of high metallic conductivity, high ion transport, low diffusion barrier, larger surface area, and ease of functionalization, MXene-based materials have been exploited as the electrode materials for different energy storage systems. Among all the current available 30+ highly conductive MXene materials,[40,41] $Ti_{n+1}C_n$-based MXene has been argued to have exceptional values of capacitance in aqueous electrolytes and excellent performance at an ultrahigh rate up to 1000 V/s.

MXene-based electrodes for supercapacitor applications were firstly explored by Gogotsi's group in 2013.[42] The spontaneous electrochemical intercalation of cations (e.g. Na^+, K^+, Mg^{2+}, NH_4^+, and Al^{3+}) from aqueous salt solution into 2D MXene layered structures, offering devices with higher capacitance. When applying the H_2SO_4 acidic environment, Lukatskaya et al. reported great enhancement of the capacity and found that reversible redox reactions at or near the surface of MXene (Ti_3C_2) play a dominant role[43] (more like a pseudo-capacitor) in charging/discharging. Meanwhile, through tuning MXene surface functional groups, the behavior of supercapacitors will differ.[6,44] Hence, the ion intercalation/transport and the reversible redox reactions both contribute to the electrochemical performance in MXene-based electrode supercapacitors.

Since the self-restacking issue of pure MXene nanosheets[45] hampered its practical applications, by hybridizing with other materials, the MXene-based composites have become the alternatives. The incorporating materials range from carbon-based materials, metal oxides, to polymers, etc. Yan et al. prepared MXene/reduced graphene oxide (rGO)[46,47] electrodes that can generate more electrochemical active sites and deliver a high volumetric capacitance of 1040 F/cm^3 at 2mV/s. Through the introduction of MXene/carbon-nanotubes (CNT) paper electrodes,[45] Zhao et al. gained good volumetric capacitance 345 F/cm^3 at 5mV/s and long-cycle lives (almost no degradation within 10000 cycles). Moreover, Rakhi et al. reported that nanocrystalline ε-MnO_2 whiskers coated on MXene nanosheet[48] displayed superior specific capacitance with ~88% retention after 10000 cycles in comparison with the pure MXene-based symmetric supercapacitor.

1.2.5 Electrolyte ions

Besides studying the electrode materials, the electrolytes (the ions) are also the main factors sensitively influencing the performance of energy storage devices.[16] It has also been found that the charge storage ways differed depending on the electrolytes. Wang's groups studied the electrochemical processes of $Ti_3C_2T_x$ electrodes in sulfate ion-containing aqueous electrolytes with three different cations (H+, Mg+, NH_4+) using *in-situ* Raman spectroscopy.[49] They found that only the hydronium in H_2SO_4 electrolyte will bond with or dissociate from the -O terminations on $Ti_3C_2T_x$ electrodes during discharging/charging processes, leading to the valence state variations of the Ti (redox reaction) and resulting in superior performance.

More specifically, changing the ion-size and concentration of electrolytes may also modify the supercapacitor behavior. Furthermore, the electrical window of the solvent is another important factor impacting the energy density of the supercapacitors. A problem that arises here is how to obtain faster ion transport in response to the electrode charge and simultaneously achieve high energy density. However, we still lack fundamental understandings of the transport behavior and material properties in supercapacitors. There are several publications showing fast proton transfer through the Grotthuss mechanism, frequent surface redox reactions within the MXene-confined interfaces,[50,51] or dynamic water behavior within 1D CNT,[52,53] but that is not enough. Many studies are still surther exploring the essence of the energy storage mechanisms to better serve the next-generation energy storage systems.

1.2.6 Computational works

Many significant problems are needed to be answered in the supercapacitor field including: i) What are the best system and material to use for ion (or proton) transport? ii) How will different systems affect transport mechanisms? iii) How can redox reactions in certain capacitor systems be enhanced?

To provide additional insights into these problems, many simulation works have been carried out. Zhan et al. conducted a computational screening of the pseudocapacitive $M_{n+1}X_nT_x$ (MXene) electrodes in H_2SO_4 electrolyte by considering the electronic structure, magnetism, and hydrogen adsorption energy, which indicated that nitrides tend to have better capacitive performance than carbides.[8] Li et al. explored various interfacial properties of different stacking of MXene/graphene heterostructures, providing comprehensive structure and property information for potential MXene-based composite electrodes.[4] Moreover, Sun et al. used the *ab-initio* Molecular dynamics (AIMD) methods to probe proton surface-redox and transfer within MXene-confined thin water layers. They concluded that the proton-intercalation processes (e.g. proton migration from the bulk electrolyte into MXene galleries) would be one of the bottlenecks for ionic-transport and charging procedures.[50]

In this dissertation, we will use first-principle methods to explore not only the geometric, energetic, electronic, and interfacial properties for various potential energy storage materials but also the mechanisms of hydrogen/proton transport inside bulk systems or within confined-interfaces.

1.3 Outline

Chapter 2 begins with an introduction of the theories for the computational methods, density-functional theory (DFT), and *ab-initio* Molecular dynamics (AIMD). Detailed mathematical formulas, as well as the parameters and corrections, will also be described. Afterwards, several main data analyzing tools that we applied during our studies will be discussed thoroughly. Finally, the software and coding packages used will be presented.

In chapter 3, we apply the DFT approach to study the structure, energetic, electronic, and kinetic properties of the hydrogen inside various cube-based-perovskites ABO_3. Meanwhile, we unravel the natural chemical bonding information for the B-O bonds influenced by the hydrogen atom using the crystal orbital Hamiltonian population (COHP). In addition, useful descriptors between the energetic properties, the integral COHP, and the specific material parameter (the electro-negativity difference ΔX_{B-A}) will be elaborated. This work provides fundamental insights into the hydrogen intercalation and transport through perovskites.

Chapter 4 explains the detailed study of interfacial properties of MXene (Ti_2CX_2/$Ti_3C_2X_2$)/anatase TiO_2 (101) (a-TiO_2) heterostructures with different surface termination groups of MXene (X= 100% -O, 100% -OH, a mixture of 90% -O and 10% -F). We also include the structures of the N-doped surface-O of TiO_2 during examinations. In this study, we analyzed the interlayer distances, the charge transfer behavior for providing basic understandings for these potential supercapacitor materials.

Chapter 5 contains a comprehensive mechanism analysis for proton transfer and surface-redox within mono water layer interfaces confined by Graphene-MXene and MXene-MXene. In this study, we focused on the -O terminated MXene since it will change to the hydroxyl group (-OH) upon surface redox processes. We demonstrated that the intercalated-proton concentration, the interface configurations, and the interfacial properties are all the factors affecting the proton transport in confined systems. This work provides more insights into proton involved energy storage mechanisms within MXene-based 2D interfaces.

Chapter 6 concludes this dissertation by summarizing all the findings. The appendix at the end consists of home-made computer codes used for computing and analyzing various properties.

Besides the supplemental information for each work, important abbreviations and a list of formulas will also be included in the supporting information attached to that chapter.

Supporting Information

1.S1 Abbreviations

DFT	Density functional theory
LSS	Large-scale systems
EES	Electrochemical energy storage
EC	Electrochemical capacitors
EDLC	Electric Double Layer Capacitor

SC	Supercapacitor
CAGR	Compound annual growth rate
SSA	Specific surface areas
TMO	Transition metal oxide
GNF	Graphene nanofibers
NW	Nanowires
2D	Two-dimensional
1D	One-dimensional
CNT	Carbon-nanotubes
rGO	Reduced-graphene oxide
AIMD	*ab-initio* Molecular dynamics
COHP	Crystal orbital Hamiltonian population

References

(1) van Mourik, T.; Bühl, M.; Gaigeot, M.-P. Density Functional Theory across Chemistry, Physics and Biology. *Philos Trans A Math Phys Eng Sci* **2014**, *372* (2011). https://doi.org/10.1098/rsta.2012.0488.

(2) Harris, S.; Kendon, V. M. Quantum-Assisted Biomolecular Modelling. *Proc. R. Soc. A* **2010**, *368* (1924), 3581–3592. https://doi.org/10.1098/rsta.2010.0087.

(3) Dorner, R.; Goold, J.; Vedral, V. Towards Quantum Simulations of Biological Information Flow. *Interface Focus* **2012**, *2* (4), 522–528. https://doi.org/10.1098/rsfs.2011.0109.

(4) Li, R.; Sun, W.; Zhan, C.; Kent, P. R. C.; Jiang, D. Interfacial and Electronic Properties of Heterostructures of MXene and Graphene. *Phys. Rev. B* **2019**, *99* (8), 085429. https://doi.org/10.1103/PhysRevB.99.085429.

(5) Xu, L.; Jiang, D. Understanding Hydrogen in Perovskites from First Principles. *Computational Materials Science* **2020**, *174*, 109461. https://doi.org/10.1016/j.commatsci.2019.109461.

(6) Zhan, C.; Sun, W.; Xie, Y.; Jiang, D.; Kent, P. R. C. Computational Discovery and Design of MXenes for Energy Applications: Status, Successes, and Opportunities. *ACS Appl. Mater. Interfaces* **2019**, *11* (28), 24885–24905. https://doi.org/10.1021/acsami.9b00439.

(7) Fung, V.; Wu, Z.; Jiang, D. New Bonding Model of Radical Adsorbate on Lattice Oxygen of Perovskites. *J. Phys. Chem. Lett.* **2018**, *9* (21), 6321–6325. https://doi.org/10.1021/acs.jpclett.8b02749.

(8) Zhan, C.; Sun, W.; Kent, P. R. C.; Naguib, M.; Gogotsi, Y.; Jiang, D. Computational Screening of MXene Electrodes for Pseudocapacitive Energy Storage. *J. Phys. Chem. C* **2019**, *123* (1), 315–321. https://doi.org/10.1021/acs.jpcc.8b11608.

(9) Wałęsa, R.; Broda, M. A. The Influence of Solvent on Conformational Properties of Peptides with Aib Residue—a DFT Study. *J Mol Model* **2017**, *23* (12), 349. https://doi.org/10.1007/s00894-017-3508-4.

(10) Hu, G.; Wu, Z.; Jiang, D. First Principles Insight into H_2 Activation and Hydride Species on TiO_2 Surfaces. *J. Phys. Chem. C* **2018**, *122* (35), 20323–20328. https://doi.org/10.1021/acs.jpcc.8b05251.

(11) Fung, V.; Tao, F. (Feng); Jiang, D. Low-Temperature Activation of Methane on Doped Single Atoms: Descriptor and Prediction. *Phys. Chem. Chem. Phys.* **2018**, *20* (35), 22909–22914. https://doi.org/10.1039/C8CP03191F.

(12) Simon, P.; Gogotsi, Y. Materials for Electrochemical Capacitors. *Nat Mater* **2008**, *7* (11), 845–854. https://doi.org/10.1038/nmat2297.

(13) Dubal, D. P.; Ayyad, O.; Ruiz, V.; Gómez-Romero, P. Hybrid Energy Storage: The Merging of Battery and Supercapacitor Chemistries. *Chem Soc Rev* **2015**, *44* (7), 1777–1790. https://doi.org/10.1039/c4cs00266k.

(14) Conway, B. E. *Electrochemical Supercapacitors: Scientific Fundamentals and Technological Applications*; Springer US, 1999. https://doi.org/10.1007/978-1-4757-3058-6.

(15) Supercapacitors Market | Growth, Trends, and Forecast (2020-2025) https://www.mordorintelligence.com/industry-reports/supercapacitor-market.

(16) Ray, A.; Roy, A.; Saha, S.; Das, S. Transition Metal Oxide-Based Nano-Materials for Energy Storage Application. *Science, Technology and Advanced Application of Supercapacitors* **2018**. https://doi.org/10.5772/intechopen.80298.

(17) Wang, T.; Chen, H. C.; Yu, F.; Zhao, X. S.; Wang, H. Boosting the Cycling Stability of Transition Metal Compounds-Based Supercapacitors. *Energy Storage Materials* **2019**, *16*, 545–573. https://doi.org/10.1016/j.ensm.2018.09.007.

(18) Xian Jian; Shiyu Liu; Yuqi Gao; Wei Tian; Zhicheng Jiang; Xiangyun Xiao; Hui Tang; Liangjun Yin. Carbon-Based Electrode Materials for Supercapacitor: Progress, Challenges and Prospective Solutions. *JEE* **2016**, *4* (2). https://doi.org/10.17265/2328-2223/2016.02.004.

(19) Mohd Abdah, M. A. A.; Azman, N. H. N.; Kulandaivalu, S.; Sulaiman, Y. Review of the Use of Transition-Metal-Oxide and Conducting Polymer-Based Fibres for High-Performance Supercapacitors. *Materials & Design* **2020**, *186*, 108199. https://doi.org/10.1016/j.matdes.2019.108199.

(20) Yu, N.; Yin, H.; Zhang, W.; Liu, Y.; Tang, Z.; Zhu, M.-Q. High-Performance Fiber-Shaped All-Solid-State Asymmetric Supercapacitors Based on Ultrathin MnO_2 Nanosheet/Carbon Fiber Cathodes for Wearable Electronics. *Advanced Energy Materials* **2016**, *6* (2), 1501458. https://doi.org/10.1002/aenm.201501458.

(21) Xu, Y.; Wei, J.; Tan, L.; Yu, J.; Chen, Y. A Facile Approach to $NiCoO_2$ Intimately Standing on Nitrogen Doped Graphene Sheets by One-Step Hydrothermal Synthesis for Supercapacitors. *J. Mater. Chem. A* **2015**, *3* (13), 7121–7131. https://doi.org/10.1039/C5TA00298B.

(22) Chaitra, K.; Sivaraman, P.; Vinny, R. T.; Bhatta, U. M.; Nagaraju, N.; Kathyayini, N. High Energy Density Performance of Hydrothermally Produced Hydrous Ruthenium Oxide/Multiwalled Carbon Nanotubes Composite: Design of an Asymmetric Supercapacitor with Excellent Cycle Life. *Journal of Energy Chemistry* **2016**, *25* (4), 627–635. https://doi.org/10.1016/j.jechem.2016.04.012.

(23) Jhao, J.-J.; Lin, C.-H.; Yeh, T.-K.; Wu, H.-C.; Tsai, M.-C.; Hsieh, C.-K. The Coaxial Nanostructure of Ruthenium Oxide Thin Films Coated onto the Vertically Grown Graphitic Nanofibers for Electrochemical Supercapacitor. *Surface and Coatings Technology* **2017**, *320*, 263–269. https://doi.org/10.1016/j.surfcoat.2017.01.006.

(24) Singh, A. K.; Sarkar, D.; Karmakar, K.; Mandal, K.; Khan, G. G. High-Performance Supercapacitor Electrode Based on Cobalt Oxide–Manganese Dioxide–Nickel Oxide Ternary 1D Hybrid Nanotubes. *ACS Appl. Mater. Interfaces* **2016**, *8* (32), 20786–20792. https://doi.org/10.1021/acsami.6b05933.

(25) Guo, C.; Yin, M.; Wu, C.; Li, J.; Sun, C.; Jia, C.; Li, T.; Hou, L.; Wei, Y. Highly Stable Gully-Network Co_3O_4 Nanowire Arrays as Battery-Type Electrode for Outstanding Supercapacitor Performance. *Front. Chem.* **2018**, *6*. https://doi.org/10.3389/fchem.2018.00636.

(26) An, C.; Zhang, Y.; Guo, H.; Wang, Y. Metal Oxide-Based Supercapacitors: Progress and Prospectives. *Nanoscale Adv.* **2019**, *1* (12), 4644–4658. https://doi.org/10.1039/C9NA00543A.

(27) Genc, R.; Alas, M. O.; Harputlu, E.; Repp, S.; Kremer, N.; Castellano, M.; Colak, S. G.; Ocakoglu, K.; Erdem, E. High-Capacitance Hybrid Supercapacitor Based on Multi-Colored Fluorescent Carbon-Dots. *Sci Rep* **2017**, *7*. https://doi.org/10.1038/s41598-017-11347-1.

(28) Tian, Q.; Wang, X.; Huang, G.; Guo, X. Nanostructured $(Co, Mn)_3O_4$ for High Capacitive Supercapacitor Applications. *Nanoscale Res Lett* **2017**, *12*. https://doi.org/10.1186/s11671-017-1977-0.

(29) Dong, R.; Ye, Q.; Kuang, L.; Lu, X.; Zhang, Y.; Zhang, X.; Tan, G.; Wen, Y.; Wang, F. Enhanced Supercapacitor Performance of Mn_3O_4 Nanocrystals by Doping Transition-Metal Ions. *ACS Appl. Mater. Interfaces* **2013**, *5* (19), 9508–9516. https://doi.org/10.1021/am402257y.

(30) Li, T.; Beidaghi, M.; Xiao, X.; Huang, L.; Hu, Z.; Sun, W.; Chen, X.; Gogotsi, Y.; Zhou, J. Ethanol Reduced Molybdenum Trioxide for Li-Ion Capacitors. *Nano Energy* **2016**, *26*, 100–107. https://doi.org/10.1016/j.nanoen.2016.05.004.

(31) Kim, H.-S.; Cook, J. B.; Lin, H.; Ko, J. S.; Tolbert, S. H.; Ozolins, V.; Dunn, B. Oxygen Vacancies Enhance Pseudocapacitive Charge Storage Properties of MoO_{3-x}. *Nature Materials* **2017**, *16* (4), 454–460. https://doi.org/10.1038/nmat4810.

(32) Xiao, X.; Ding, T.; Yuan, L.; Shen, Y.; Zhong, Q.; Zhang, X.; Cao, Y.; Hu, B.; Zhai, T.; Gong, L.; Chen, J.; Tong, Y.; Zhou, J.; Wang, Z. L. WO_{3-x}/MoO_{3-x} Core/Shell Nanowires on Carbon Fabric as an Anode for All-Solid-State Asymmetric Supercapacitors. *Advanced Energy Materials* **2012**, *2* (11), 1328–1332. https://doi.org/10.1002/aenm.201200380.

(33) Mefford, J. T.; Hardin, W. G.; Dai, S.; Johnston, K. P.; Stevenson, K. J. Anion Charge Storage through Oxygen Intercalation in $LaMnO_3$ Perovskite Pseudocapacitor Electrodes. *Nat Mater* **2014**, *13* (7), 726–732. https://doi.org/10.1038/nmat4000.

(34) Ke, Q.; Wang, J. Graphene-Based Materials for Supercapacitor Electrodes – A Review. *Journal of Materiomics* **2016**, *2* (1), 37–54. https://doi.org/10.1016/j.jmat.2016.01.001.

(35) Naguib, M.; Kurtoglu, M.; Presser, V.; Lu, J.; Niu, J.; Heon, M.; Hultman, L.; Gogotsi, Y.; Barsoum, M. W. Two-Dimensional Nanocrystals Produced by Exfoliation of Ti_3AlC_2. *Advanced Materials* **2011**, *23* (37), 4248–4253. https://doi.org/10.1002/adma.201102306.

(36) Gogotsi, Y.; Anasori, B. The Rise of MXenes. *ACS Nano* **2019**, *13* (8), 8491–8494. https://doi.org/10.1021/acsnano.9b06394.

(37) Naguib, M.; Mashtalir, O.; Carle, J.; Presser, V.; Lu, J.; Hultman, L.; Gogotsi, Y.; Barsoum, M. W. Two-Dimensional Transition Metal Carbides. *ACS Nano* **2012**, *6* (2), 1322–1331. https://doi.org/10.1021/nn204153h.

(38) Li, S.-Y.; Wang, W.-P.; Duan, H.; Guo, Y.-G. Recent Progress on Confinement of Polysulfides through Physical and Chemical Methods. *Journal of Energy Chemistry* **2018**, *27* (6), 1555–1565. https://doi.org/10.1016/j.jechem.2018.04.014.

(39) Anasori, B.; Lukatskaya, M. R.; Gogotsi, Y. 2D Metal Carbides and Nitrides (MXenes) for Energy Storage. *Nature Reviews Materials* **2017**, *2* (2), 1–17. https://doi.org/10.1038/natrevmats.2016.98.

(40) Lukatskaya, M. R.; Kota, S.; Lin, Z.; Zhao, M.-Q.; Shpigel, N.; Levi, M. D.; Halim, J.; Taberna, P.-L.; Barsoum, M. W.; Simon, P. Ultra-High-Rate Pseudocapacitive Energy Storage in Two-Dimensional Transition Metal Carbides. *Nature Energy* **2017**, *2* (8), 17105. http://dx.doi.org/10.1038/nenergy.2017.105

(41) Pomerantseva, E.; Bonaccorso, F.; Feng, X.; Cui, Y.; Gogotsi, Y. Energy Storage: The Future Enabled by Nanomaterials. *Science* **2019**, *366* (6468). https://doi.org/10.1126/science.aan8285.

(42) Lukatskaya, M. R.; Mashtalir, O.; Ren, C. E.; Dall'Agnese, Y.; Rozier, P.; Taberna, P. L.; Naguib, M.; Simon, P.; Barsoum, M. W.; Gogotsi, Y. Cation Intercalation and High Volumetric Capacitance of Two-Dimensional Titanium Carbide. *Science* **2013**, *341* (6153), 1502–1505. https://doi.org/10.1126/science.1241488.

(43) Lukatskaya, M. R.; Bak, S.-M.; Yu, X.; Yang, X.-Q.; Barsoum, M. W.; Gogotsi, Y. Probing the Mechanism of High Capacitance in 2D Titanium Carbide Using In Situ X-Ray Absorption Spectroscopy. *Advanced Energy Materials* **2015**, *5* (15), 1500589. https://doi.org/10.1002/aenm.201500589.

(44) Hart, J. L.; Hantanasirisakul, K.; Lang, A. C.; Anasori, B.; Pinto, D.; Pivak, Y.; van Omme, J. T.; May, S. J.; Gogotsi, Y.; Taheri, M. L. Control of MXenes' Electronic Properties through Termination and Intercalation. *Nature Communications* **2019**, *10* (1), 1–10. https://doi.org/10.1038/s41467-018-08169-8.

(45) Zhao, M.-Q.; Ren, C. E.; Ling, Z.; Lukatskaya, M. R.; Zhang, C.; Aken, K. L. V.; Barsoum, M. W.; Gogotsi, Y. Flexible MXene/Carbon Nanotube Composite Paper with High Volumetric Capacitance. *Advanced Materials* **2015**, *27* (2), 339–345. https://doi.org/10.1002/adma.201404140.

(46) Zhao, C.; Wang, Q.; Zhang, H.; Passerini, S.; Qian, X. Two-Dimensional Titanium Carbide/RGO Composite for High-Performance Supercapacitors. *ACS Appl. Mater. Interfaces* **2016**, *8* (24), 15661–15667. https://doi.org/10.1021/acsami.6b04767.

(47) Yan, J.; Ren, C. E.; Maleski, K.; Hatter, C. B.; Anasori, B.; Urbankowski, P.; Sarycheva, A.; Gogotsi, Y. Flexible MXene/Graphene Films for Ultrafast Supercapacitors with Outstanding Volumetric Capacitance. *Advanced Functional Materials* **2017**, *27* (30), 1701264. https://doi.org/10.1002/adfm.201701264.

(48) Rakhi, R. B.; Ahmed, B.; Anjum, D.; Alshareef, H. N. Direct Chemical Synthesis of MnO2 Nanowhiskers on Transition-Metal Carbide Surfaces for Supercapacitor Applications. *ACS Appl. Mater. Interfaces* **2016**, *8* (29), 18806–18814. https://doi.org/10.1021/acsami.6b04481.

(49) Hu, M.; Li, Z.; Hu, T.; Zhu, S.; Zhang, C.; Wang, X. High-Capacitance Mechanism for $Ti_3C_2T_x$ MXene by in Situ Electrochemical Raman Spectroscopy Investigation. *ACS Nano* **2016**, *10* (12), 11344–11350. https://doi.org/10.1021/acsnano.6b06597.

(50) Sun, Y.; Zhan, C.; Kent, P. R. C.; Naguib, M.; Gogotsi, Y.; Jiang, D. Proton Redox and Transport in MXene-Confined Water. *ACS Appl. Mater. Interfaces* **2020**, *12* (1), 763–770. https://doi.org/10.1021/acsami.9b18139.

(51) Miyake, T.; Rolandi, M. Grotthuss Mechanisms: From Proton Transport in Proton Wires to Bioprotonic Devices. *J. Phys.: Condens. Matter* **2015**, *28* (2), 023001. https://doi.org/10.1088/0953-8984/28/2/023001.

(52) Joseph, S.; Aluru, N. R. Why Are Carbon Nanotubes Fast Transporters of Water? *Nano Lett.* **2008**, *8* (2), 452–458. https://doi.org/10.1021/nl072385q.

(53) Melillo, M.; Zhu, F.; Snyder, M. A.; Mittal, J. Water Transport through Nanotubes with Varying Interaction Strength between Tube Wall and Water. *J. Phys. Chem. Lett.* **2011**, *2* (23), 2978–2983. https://doi.org/10.1021/jz2012319.

Chapter 2

Computational Methods and Theories

2.1 Born-Oppenheimer (BO) approximation

The key problem that quantum methods aim to address is to compute the properties of materials from first principles. This amounts to solving static (time-independent) many-body Schrödinger equation:

$$\hat{H}_{total}\Psi_{total}(\vec{r},\vec{R}) = E\Psi_{total}(\vec{r},\vec{R}) \tag{2.1}$$

$$\hat{H}_{total} = \hat{T}_{ele} + \hat{T}_{Nuc} + \hat{V}_{ele-ele} + \hat{V}_{Nuc-ele} + \hat{V}_{Nuc-Nuc} \tag{2.2}$$

where the Hamiltonian ($\hat{H}$) is the sum of the kinetic and potential energy operators for electrons and nuclei, $\vec{r}$, and $\vec{R}$ denote the electronic and nuclear coordinates, respectively.

However, solving the Schrödinger equation both analytically and numerically is always extremely difficult and often impractical. Various theories have been established to approximate the solution. Among all, the most commonly used approximation is Born-Oppenheimer (BO) approximation[1]: The nucleus in a molecule are stationary with respect to electrons, which is not only because they are heavier than electrons but also the electrons can respond "instantaneously" to the changes of nucleus position. This assumption allows one to decouple the electronic motion from the nuclear motion:

$$\Psi_{total}(\vec{r},\vec{R}) = \Psi_{ele}(\vec{r},\vec{R})\Psi_{Nuc}(\vec{R}) \tag{2.3}$$

Hence, we can separate the electronic and nuclear coordinates. Then, the energy of a molecule can be estimated by solving the electronic Schrödinger equation:

$$\hat{H}_{ele}\Psi_{ele}(\vec{r},\vec{R}) = E_{ele}\Psi_{ele}(\vec{r},\vec{R}) \tag{2.4}$$

$$\hat{H}_{ele} = \hat{T}_{ele} + \hat{V}_{ele-ele} + \hat{V}_{ext} \tag{2.5}$$

where $\Psi_{ele}(\vec{r},\vec{R})$ is the electronic wavefunctions, and $\hat{H}_{ele}$ is the electronic Hamiltonian, the $\hat{T}_{ele}$, $\hat{V}_{ele-ele}$ and $\hat{V}_{ext}$ (including the $\hat{V}_{Nuc-Nuc}$ and $\hat{V}_{Nuc-ele}$ terms) are the kinetic, electron-electron, and potential energy operators, respectively.

As it is beyond our current or foreseeable tools to solve the Schrödinger equation of complex systems with more than a few electrons exactly, many methods have been developed to achieve accurate estimates with a reasonable computational cost. Usually, higher accuracy means an increase in computational cost. Generally, there are two broad classes[2] of methods to solve the time-independent Schrödinger equation:

A) The wavefunction-based approaches:[3]

   a) Variational principle: Hartree-Fock (HF), Configuration interaction (CI), etc.

b) Perturbational theory: Møller-Plesset, etc.

B) Density-based approaches: Density Functional Theory (DFT), etc.

Both classes used the strategy of simplifying the original complicated many-body problems towards substituting with many single-particle equations. Since this thesis mainly focuses on DFT, detailed theories will be discussed in the subsequent sections after the following short summary of the wavefunction-based approaches.

Among many wavefunction-based approaches, the most famous one is the Hartree-Fock (HF) methodology, in which the electronic wavefunction of the system is approximated by a single slater determinant of a set of orthonormal single-particle orbitals. Based on the mean-field approximation, HF treats each electron separately and takes the effect of all other electrons into consideration. As a matter of fact, the electron-motions are correlated and instantly avoid each other, indicating that electrons are further apart from each other than what the HF describes. Thus, in the HF equation, the explicit description of the electron-electron interactions is missing. To make up for this drawback, many upgraded methods (so-called post-HF methods) such as the configuration interaction (CI), the Møller-Plesset perturbational theory, or the gold-standard coupled-cluster (CC) method were founded.

In contrast to the wavefunction-based approach, the wavefunction is not explicitly written in the electron density-based approaches. In addition, the most significant difference between the two means settled on the side of accounting the electron-correlations. In section 2.2, I will concentrate on the most potent and popular electron density-based methods to date — Density Functional Theory (DFT).

2.2 Density Functional Theory (DFT)

Presently, Density Functional Theory (DFT) is the most promising and successful approach to compute the structure and electronic properties in a variety of materials. The applications for DFT range from atoms, molecules to solid- and liquid- systems. Additionally, DFT can predict a significant number of material properties, such as chemical molecular structures, vibrational/thermodynamic phenomenon, atomization/ionization energies, electronic/magnetic properties, optical spectra, and reaction paths.[4,5] Overall, DFT has been increasingly implemented as an exploratory technique for materials discovery and computational experiments in the fields of condensed matter physics, quantum chemistry, materials engineering, or even more distant fields: biology, and mineralogy, etc.

2.2.1 Basic theories

The concept of density functional can be traced back to the 1920s of the studies done by Thomas[6] (1926) and Fermi[7] (1928), who came with the idea of expressing the system energy as a function of the total electron density. There are two main advantages for DFT compared with Hartree-Fock (HF) methods:[8] 1) The computation of exchange-correlation (XC) functional significantly lowers the computational cost (from 3N spatial coordinates of N strongly interacting electrons for the many-body formalism Schrödinger equation to a simpler mathematically equivalent 3-dimensional theory of non-interacting electrons) and improves the accuracy; 2) The automatic inclusion of the electron

correlation. The goal of DFT is to design functionals connecting the electron density $\rho(\vec{r})$ with energy.

$$\rho(\vec{r}) = N \int \cdots \int |\Psi_{ele}(\vec{r}, \vec{r}_1, \vec{r}_2, \cdots, \vec{r}_N)|^2 \, d\vec{r} d\vec{r}_1 \cdots d\vec{r}_N \tag{2.6}$$

where *N* is the total number of electrons. The stage for the DFT referred here was set by two theorems published by Hohenberg and Kohn in 1964:[9]

Theorem 1 *The ground-state properties of a many-electron system depend only on the electron density*

$$E_0 = E[\rho_0(\vec{r})] \tag{2.7}$$

Theorem 2 *The true ground state density minimizes the total energy (i.e. the variational principle)*

$$E[\rho_t(\vec{r})] \geq E[\rho_0(\vec{r})] \tag{2.8}$$

where $\rho_t(\vec{r})$ is the trial electronic density, $E[\rho_0(\vec{r})]$ is the true ground-state energy, and $\rho_0(\vec{r})$ is the ground state density. After further approximating the electrons as non-interacting, the electronic wavefunction can be constructed as a Slater determinant[10] from a set of single-electron orbitals. Hence, the Schrödinger equation can be written as:

$$\left(-\frac{\hbar^2}{2m}\nabla^2 + v_{eff}(\vec{r})\right)\Phi_i(\vec{r}) = \epsilon_i \Phi_i(\vec{r}) \tag{2.9}$$

$$v_{eff}(\vec{r}) = v_{ext}(\vec{r}) + \int \frac{\rho_0(\vec{r}')}{|\vec{r} - \vec{r}'|} d\vec{r}' + \frac{\delta E_{XC}[\rho_0(\vec{r})]}{\delta \rho_0(\vec{r})} \tag{2.10}$$

where $v_{eff}(\vec{r})$ is the effective or Kohn-Sham potential,[11,12] $v_{ext}(\vec{r})$ is the external potential, acting on the electron-nuclei interaction and emerging as a functional of the electron density. The middle term in Eq. (2.10) is the inter-electronic repulsion. The sum

of two terms $\left(-\frac{\hbar^2}{2m}\nabla^2 + \int \frac{\rho_0(\vec{r}')}{|\vec{r}-\vec{r}'|}d\vec{r}'\right)$ in the Hamiltonian can be viewed as the density functional for the kinetic and Coulombic interactions. The last term in Eq. (2.10) is the exchange-correlation potential, which hides all difficulties from many-body effects. From the computational point of view, the electron density $\rho(\vec{r})$ of the system is computed from the single-electron orbitals Φ_i as following:

$$\rho_0(\vec{r}) = \sum_i^N \Phi_i^*(\vec{r})\Phi_i(\vec{r}) \tag{2.11}$$

From the Kohn-Sham approach,[12] the total energy can be decomposed into the kinetic energy (T_0), the potential energy (coulombic (J) and external (V_{ext}) energy) and exchange-correlation energy (E_{XC}):

$$E(\rho_0(\vec{r})) = T_0(\rho_0(\vec{r})) + J(\rho_0(\vec{r})) + \int v_{ext}(\vec{r})\rho_0(\vec{r})d\vec{r} + E_{XC}(\rho_0(\vec{r})) \tag{2.12}$$

It is important to point out that both of T_0 and J are given by known expressions. Since they both depend on the $\rho_0(\vec{r})$, a self-consistent field procedure should be applied to solve the Kohn-Sham equations. However, the exact form of E_{XC} is unknown, and various degrees of approximation methods have been devised.

2.2.2 The exchange-correlation approximation

The quantity of the exchange-correlation energy E_{XC} can be further split into the exchange-energy functional (E_X) and correlation-energy functional (E_C) as:[13]

$$E_{XC}(\rho_0(\vec{r})) = E_X(\rho_0(\vec{r})) + E_C(\rho_0(\vec{r})) \tag{2.13}$$

Since the Kohn-Sham orbitals closely resemble the Hartree-Fock orbitals, the dominating differences between Kohn-Sham and Hartree-Fock equations are the terms of the local electron exchange energy and an additional electron correlation energy. In practice, modeling the combination of E_X and E_C yields better results due to the inner error-cancellation. So far, the most applied approximations for XC functional have been the local-density approximation (LDA) and the generalized gradient approximation (GGA[14]). Both approximations rely on the homogeneous-electron-gas model.[15,16]

Local Density Approximation (LDA)

The local density approximation (LDA) is the basis of all approximate XC functionals. LDA utilizes only the electron density, ($\rho_0(\vec{r})$), at spatial point $\vec{r}$ to determine that point XC energy density. For this reason, the exchange part may have an analytical solution. But for the correlation part, there exist different versions of approximations, and the most well-known one is the quantum Monte Carlo calculations, where the part is obtained through parameterizing and fitting.[15,17] In the systems with more homogeneous electron density (e.g. the homogeneous solid metals), the structural properties (e.g. bond-length, -angle, vibrational frequency) predicted by the LDA method are comparable to the experimental values. However, materials are inhomogeneous in reality, so LDA tends to overestimate the bond strength in various practical solids or molecules.

Generalized Gradient Approximation (GGA)

Through introducing the electron density-gradient ($\nabla\rho_0(\vec{r})$) as an independent variable, the generalized gradient approximation (GGA) outperform LDA in predicting cohesive energy, atomization, energy barrier, structure properties, etc. The commonly

applied GGA-functional are the Perdew-Wang from 1991 (PW91[18]) and Perdew-Burke-Ernzerhof (PBE[14]). They are both "parameter-free", meaning that newly determined parameters would be added to satisfy certain exact theoretical conditions of the XC potential. Although the accuracy of the GGA is based on the system-dependent error-cancellation, GGA is still very popular in chemistry applications, especially those of metal oxides.

2.2.3 Pseudopotentials (PP) & Projected Augmented Wave (PAW)

The success of the post-DFT methodology is largely attributed to the treatment of the core electrons. Via introducing the concept of pseudopotential (PP), the core electrons, as well as the nucleus, were treated with an ionic pseudopotential since the core electrons are assumed to change very little with the environments.[19] The relative few valence electrons are described by nodeless pseudo-wavefunctions due to their chemically active motion near the core regions. Moreover, it is also important to note that the PP method bounds to the periodic boundary conditions rigorously. Even though all information on the charge density and wavefunctions near the nucleus may be lost, PP is still a crucial concept for plane-wave total energy methods. The PP approach reduces the complexity of the Schrödinger equation and, to some degree, help decrease the computational cost with concomitant greater accuracy.

In the 1990s, Blöchl proposed the calculations of hyperfine pseudopotential parameters using the projector augmented wave methods (PAW).[20,21] This method separates the wave function into two segments: i) a partial-wave expansion within an atom-

centered sphere; ii) the envelope functions outside the spheres. This method has been further improved and implemented in various codes, like the Vienna *Ab initio* Simulation Package (VASP),[21,22] Electronic Structure Code for Materials Properties and Processes (ESTCoMPP, R. Berger et al., Proceedings of the NIC-Workshop "Molecular Dynamics on Parallel Computers", Jülich, 08.-10. Februar 1999, World Scientific 1999), etc.

2.2.4 Blöch's theorem & Plane-wave Basis sets

In Blöch's theorem,[23] the wavefunction of the infinite crystal is expressed in terms of the wavefunctions at the reciprocal of the Bravais lattice. The periodicity of the unit cell would be employed so that only the electrons in the cell would be calculated. Therefore, the wavefunction is the combination of the lattice-periodic part and a wavelike part:

$$\psi_i(\vec{r}) = exp(i\vec{k} \cdot \vec{r}) u_i(\vec{r}) \tag{2.14}$$

The first term is the plane-wave part in which $\vec{k}$ is the wave vector confined by the Brillouin zone. The second term is the periodic part:

$$u_i(\vec{r}) = \sum_G c_{i,\vec{G}}\, exp(i\vec{G} \cdot \vec{r}) \tag{2.15}$$

where $c_{i,\vec{G}}$ and $\vec{G}$ is the plane wave coefficients and the reciprocal lattice vectors, respectively. This equation needs to meet the requirement $\overrightarrow{G} \cdot \vec{L} = 2m\pi$ (m: integer, $\vec{L}$: the lattice vector). With Eq. (2.15), Eq. (2.14) can be rearranged as:

$$\psi_i(\vec{r}) = \sum_G c_{i,\vec{k}+\vec{G}}\, exp\{i(\vec{k} + \vec{G}) \cdot \vec{r}\} \tag{2.16}$$

Hence, a greater efficiency can be obtained when mapping the infinite-number electron problem onto a finite number of electronic wavefunctions.[24] By sampling reasonable k-points[25] and choosing an appropriate cut-off energy, improved precision can be achieved during calculations.

2.3 *Ab-initio* Molecular Dynamics (AIMD)

In the molecular dynamics (MD) scheme, the central question is: how can interatomic interactions be described over time? For the classical molecular dynamics (CMD), predefined potentials, force fields, etc., are commonly used. Thus, CMD can be applied to large-scale systems. However, since most force fields do not involve quantum effects, it is necessary to turn to the *Ab-initio* molecular dynamics method (AIMD).[26,27]

2.3.1 Basic theories

By performing Quantum Mechanics (QM) calculations to determine the interatomic interactions, the forces acting on the nuclei are computed "on-the-fly" using electronic structure calculations. The generated atomic trajectories are used for further analysis.[28] The electronic degrees of freedom are active during the dynamical simulations. The family of methods based on this approach is referred to as *Ab-initio* Molecular Dynamics (AIMD). In its most ideal form with the Born-Oppenheimer approximation, it is assumed that the system is only composed of N_{nuc} nuclei and N electrons, and that the dynamics of the nuclei can be treated classically on the ground-state electronic surface.[29]

The total Hamiltonian is shown in Eq. (2.2). If $\vec{R}_1, \cdots, \vec{R}_{N_{nuc}} \equiv \vec{R}$ denote the nuclear position, the classical dynamics of the nuclei is given by an equation of motion:

$$M_I \ddot{\vec{R}}_I = -\nabla_I [\varepsilon_0(\vec{R}) + V_{N_{nuc}}(\vec{R})] \tag{2.17}$$

where $\varepsilon_0(\vec{R})$ is the ground-state energy eigenvalue at the nuclear configuration $\vec{R}$. Since it is hard to solve the ground–state electronic problem exactly, ie. $\hat{H}_{ele}\Psi_0(\vec{r}, \vec{R}) = \varepsilon_0(\vec{R})\Psi_0(\vec{r}, \vec{R})$, DFT is commonly applied.[8,29]

AIMD methodology has been successfully applied to a large variety of physical, chemical, material, and biology problems. Furthermore, AIMD has provided microscopic insights into many chemical processes in condensed phases, leading to innovative paradigms in rationalizing experimental data, and predictions of new phenomena.

2.3.2 Canonical ensemble

The canonical ensemble is a statistical ensemble which is highly appropriate for treating the physical states in thermal equilibrium with an energy reservoir, e.g. the "heat bath", at a fixed temperature.[30] Therefore, with the exchangeable energy between the system and "heat bath", the total energy of the system will oscillate within a small range.

With the specified number of particles (N), the defined temperature (T), and the constant volume (V) (constrained by the periodic boundary conditions), the NVT canonical ensemble is widely used in many "real-life" experimental systems. In this ensemble, the critical challenge is quantifying the temperature (T). From the view of the statistical mechanics, the T can be related to the kinetic energy according to the equipartition theorem,

the kinetic energy is equally distributed on the various degrees of freedom of the system, and by solving the Maxwell-Boltzmann (MB) distribution:[31,32]

$$P(|\vec{p}|) = \left(\frac{\beta}{2\pi m}\right)^{\frac{2}{3}} exp\left(\frac{-\beta|\vec{p}|^2}{2m}\right), \qquad \beta = \frac{1}{k_B T} \tag{2.18}$$

where m is the particle mass, k_B is the Boltzmann constant and $\vec{p}$ is the momentum.

$$\vec{p} = m\vec{v} \tag{2.19}$$

Thus, the instantaneous temperature is given by:

$$T = \frac{|\vec{p}|^2}{3mNk_B} \tag{2.20}$$

T will not be a constant but it will fluctuate around a particular value.

In our AIMD study, we mainly focused on applying the NVT canonical ensemble. There are many other statistical ensembles, like the isobaric-isothermal ensemble NpT (constant number of particles, pressure, and temperature), the microcanonical ensemble NVE (constant number of particles, volume, and total energy), and the grand canonical ensemble μVT (constant chemical potential, volume, and temperature). Details of these ensembles will not be provided in this thesis and interested readers are referred to various reviews provided online.

2.3.3 Dispersion correction

It is known that DFT cannot describe the long-range dispersion interactions correctly.[33,34] For reaching better chemical accuracy, the van der Waals (vdW) dispersion-correction was introduced, which involves empirically fitted parameters for all atom-pairs.

Specifically, the vdW interactions account for the attractive part between the atoms and molecules that are not directly bonded to each other,[35] especially in the surface chemistry, the bio- or nano-architectures, etc. So far, the most popular dispersion correction form employed in DFT is named as DFT-D (atom pairwise sum over $-C_6/R^6$) method proposed by Grimme et al. Among all versions of the DFT-D methods (each post-version is promoted by upgrading the derivation of the coefficients in the empirical fitting[36–39]), the DFT-D2 and -D3 are the most widely used in large-scale molecular simulations. The fundamental idea for the DFT-Dn is adding dispersion correction ($E_{Disp-corr}$) to the Kohn-Sham portion (E_{KS}) of the total energy (E_{DFT-D}) as:[35]

$$E_{DFT-D} = E_{KS} + E_{Disp-corr} \tag{2.21}$$

$$E_{Disp-corr} = -S_6 \sum_{I=1}^{N-1} \sum_{J=I+1}^{N} \frac{C_6^{IJ}}{R_{IJ}^{\ 6}} f_{damp}(R_{IJ}) \tag{2.22}$$

where N is the total atom number. R_{IJ} and C_6^{IJ} are the interatomic distance and dispersion coefficients for different atom pairs IJ, respectively. S_6 is the empirical scaling factor depending on the functional, e.g. $S_6 = 0.75$ for PBE, $S_6 = 1.05$ for B3LYP, $S_6 = 1.2$ for BLYP. The damping function f_{damp} is used to account for the repulsive interaction between the nuclei with a minimal bonding distance, R_{IJ}.

At the early development stage of the DFT-D (e.g. DFT-D1[36] and DFT-D2[39]), the dispersion coefficients C_6^{IJ} are predetermined parameters, resulting from atomic ionization potentials and static polarizabilities. Since the atomic environment is not involved, substantial errors may be brought to final results. Therefore, the post-developed DFT-D3

overcomes this issue by introducing the effective volume concept and taking neighboring atoms into account. In its more explicate expression, the R^{-8} based damping function and dispersion coefficients are included:[40]

$$E_{Disp-corr}^{DFT-D3} = -\sum_{I=1}^{N-1}\sum_{J=I+1}^{N}\sum_{n=6,8}\left[S_n\left(\frac{C_{n,IJ}}{R_{IJ}^n}\right)f_{n,damp}(R_{IJ})\right] \tag{2.23}$$

Currently, there are two main forms of the damping functions for DFT-D3, one is the Zero-damping[42] and another is the Becke-Johnson (BJ) damping.[42–44]

Zero damping:

$$f_{n,damp}^{D3-Zero}(R_{IJ}) = \left[1 + 6\left(\frac{R_{IJ}}{S_{R,n}R_{0,IJ}}\right)^{-\alpha_n}\right]^{-1} \tag{2.24}$$

$$R_{0,IJ} = \sqrt{\frac{C_{8,IJ}}{C_{6,IJ}}} \tag{2.25}$$

where the parameters α_6, α_8, and $S_{R,8}$ are the fixed values. $S_{R,6}$, S_6, and S_8 are the adjustable parameters depending on the functional selected.

Becke-Johnson (BJ) damping:

$$f_{n,damp}^{D3-BJ}(R_{IJ}) = \frac{R_{IJ}^n}{R_{IJ}^n + \left(a_1R_{0,IJ} + a_2\right)^n} \tag{2.26}$$

Likewise, a_1, a_2 and S_8 are the adjustable parameters relying on the chosen functional. S_6 is a fixed value 1. In general, the DTF-D3(BJ) performs better than the DFT-D3(Zero) due to the improvement in the calculations of the nonbonded- distances and energies.

2.4 Computational analysis

Ever since the rapid development of computational and simulation methods in solving various chemical and physical related problems, various new analytical techniques were coming out to tackle more particular theoretical points. In the following section, I will give a brief introduction to several analytical tools used in our work.

2.4.1 Bader charge analysis

Atomic charges in the molecules or solids are not observable, thereby will not be determined by QM theory. For obtaining the partial charge of an individual atom in the system, "how to partition the continuous electronic charge density given by common QM calculations" would be the central problem. Many different schemes have been proposed, the Bader's "Quantum Theory of Atoms in Molecules" method developed by Henkelman *et al.* is the one based on the charge density.[45,46]

In Bader's "atoms in molecules" theory, the boundaries are defined to partition the electronic density charges. The 3-dimensional (3D) system space would be divided into many subsystems, each one hopefully surrounding only one nucleus or none. The boundary of each subsystem is defined as the surface through which the charge density gradient has a zero flux:[47–49]

$$\nabla\rho(r_s) \cdot n(r_s) = 0 \tag{2.27}$$

where r_s is the point on the surface $S(r_s)$, $n(r_s)$ is the unit vector perpendicular to the surface S. The Bader charge scenario offers a powerful way to analyze the properties of atoms and chemical bonding within the systems.[50]

2.4.2 Crystal Orbital Hamilton Population (COHP)

The concept of the Crystal Orbital Hamilton Population (COHP), introduced in 1993, is an inheritor of the crystal orbital overlap population (COOP) with the extended Hückel theory.[51,52] Through multiplying the density of state (DOS) by the overlap population, COOP (or COHP) technique has been argued as the efficient and reliable tool to unravel the natural chemical-bonding information (bonding, non-bonding, and anti-bonding interactions) between atom (orbital) pairs within a given solid-state material from electronic band structure calculations.[53]

In analogy to the DOS, one can specify each natural bonding contribution, positive overlap population (-pCOHP > 0) represents the bonding contribution and negative one (-pCOHP < 0) accounts for antibonding contribution.[54,55] What's more, the bonding strength can be quantitatively determined by the integration of -COHP (-ICOHP) up to the Fermi-level. A larger -ICOHP value indicates a stronger bonding interaction. COHP has been successfully applied to many solid-state systems, such as the rare-earth transition-metal halides, the polar intermetallic compounds.[56]

2.4.3 Transition state search

The transition state theory (TST), proposed by Eyring, Evans, and Polanyi in 1935,[57,58] has a very far-reaching influence in computational chemical predictions on chemical reactivity, mechanistic investigation, and catalyst designs. The transition state—a particular configuration along the reaction coordinates corresponds to the state of the first-order saddle points on the potential energy surface (PES). Therefore, a transition state

search is a sort of geometry optimization to find a stationary point on the PES (between stable molecular conformations) with exactly one negative eigenvalue in Hessian.

Variety of methods were developed for the transition state search, the single-ended methods are based on the guess of the transition state structure, while the double-ended one relies on the initial knowledge of the reactants and products.[59–63] To avoid the expensive Hessian calculations for the plane-wave methods, many methodologies are primarily monitoring the points where the energy (or force) gradients vanish. In our work, we used the double-ended method—the Nudged Elastic Band (NEB) method.[64,65]

Nudged Elastic Band

For the Nudged Elastic Band (NEB) technique, besides the given optimized geometries of the reactant and product, several intermediate images connected in between would be generated via the linear interpolation method. This image-optimization would be done by adding spring forces along the band with equal spacing between the neighboring images as well as by projecting out the component of the force due to the potential perpendicular to the band.[66] In addition, during the NEB optimization in our study, a climbing image algorithm (CI-NEB) is used to derive the highest-energy image in the pathway to the transition state.[65]

NEB method has been widely applied in many chemical-related problems. However, there are some tricks that we need to consider once using:[67]

i) Testing more states for reactants and products to eliminate the artificially introduced bias;

ii) Ensuring the appropriate amount of the intermediate images to guarantee the resolutions for locating the first-order saddle point;

To date, dedications have been focused on improving the efficiency and accuracy of the present NEB methods, such as the adaptive nudged elastic band approach (FEA-NEB[68]), and others.

2.4.4 Radial distribution function (RDF)

The Radial distribution function (RDF) ($g(r)$) describes the probability of finding a particle as a function of the distance r from a given reference particle. In the computational simulations, the RDF is proved to be particularly efficient in extracting structure information from systems. In a 3D system, considering a spherical shell (V_{shell}) of thickness dr at a distance r from a chosen atom:

$$V_{shell} = \frac{4}{3}\pi(r+dr)^3 - \frac{4}{3}\pi r^3 \approx 4\pi r^2 dr \tag{2.28}$$

The total number of the particles in the shell would be $4\pi\rho r^2 dr$, where ρ is the bulk density of particles. Then the RDF ($g_{AB}(r)$) between particle A and B can be evaluated using the formula:[69]

$$g_{AB}(r) = \frac{dn_{AB}(r)}{4\pi\rho r^2 dr} \tag{2.29}$$

where $dn_{AB}(r)$ is the function that computes the mean number of particles within a shell V_{shell} at distance r. Another important concept is the radial cumulative distribution function ($G_{AB}(r)$):

$$G_{AB}(r) = 4\pi \int_0^r r'^2 \, g_{AB}(r') dr' \tag{2.30}$$

Using the $G_{AB}(r)$, we can get the coordination number ($N_{AB}(r)$):

$$N_{AB}(r) = \rho G_{AB}(r) \tag{2.31}$$

Thus, we can obtain the number of particles within the range of each coordination sphere.

2.4.5 Mean square displacement (MSD)

In a dynamic system, the molecules will do random motion instead of remaining in the same position. One may wonder how far a particle (molecule) will travel within a fixed time period? Commonly, the question can be answered by a physical process, the diffusion rate (constant),[70–72] which can be calculated from the mean square displacement (MSD) results.

MSD is determined to measure the deviation of initial and final positions of the same particle over a certain time interval. From the statistical mechanic's point of view, the MSD is defined by the relation:[73,74]

$$MSD(t) = \langle \boldsymbol{r}^2(\Delta t) \rangle = \langle (\boldsymbol{r_i}(\Delta t + t_0) - \boldsymbol{r_i}(t_0))^2 \rangle \tag{2.32}$$

$$= \frac{1}{N} \sum_{i=1}^{N} (\boldsymbol{r_i}(\Delta t + t_0) - \boldsymbol{r_i}(t_0))^2$$

where $\boldsymbol{r_i}(\Delta t + t_0)$ and $\boldsymbol{r_i}(t_0)$ are the position of particle i at the time $(\Delta t + t_0)$ and the reference position at t_0, respectively. N is the total number of snapshots to be averaged. For normal diffusion processes, the MSD increases linearly with time.

2.4.6 Diffusion coefficients

One of the main purposes of the MSD analysis is the extraction of the self-diffusion coefficients by using the Einstein relation.[75–78]

$$D = \lim_{t\to\infty} \frac{1}{2nt} \langle \boldsymbol{r}^2(\Delta t) \rangle = \frac{1}{2n} \frac{dMSD(t)}{dt} \tag{2.33}$$

where n is the dimensionality of the system. One requirement for this method is that the time intervals should be sufficiently long for $MSD(t)$ plot to be within the linear regime.

2.5 Software & Simulation Packages & Home-made Codes

This section lists all the software and computational simulation packages utilized in all the work referred to in this dissertation.

Quantum mechanical packages

i) Vienna *Ab initio* Simulation Package[22] (VASP) 5.4.1 — performing DFT and AIMD simulations

Visualization programs

i) Visual Molecular Dynamics[79] (VMD) 1.9.3 — displaying optimized structures and analyzing molecular dynamic trajectories

ii) Molden[80] 5.8 — displaying molecular structures, analyzing electronic structures

iii) Visualization for Electronic and STructural Analysis[81] (VESTA) 3.4.0 — displaying and analyzing the structure, making the high-resolution figures, plotting the electron-density differences

iv) Avogadro[82] 1.2.0 — molecular editor, displaying structures, creating figures

Analyzing tools

i) P4VASP v0.3.29r1 — plotting Density of State (DOS), projected Density of State (pDOS), and analyzing work functions; Available online: http://www.p4vasp.at/

ii) Local-Orbital Basis Suite Towards Electronic-Structure Reconstruction[83–85] (LOBSTER) 3.1.0 — analyzing nature bonding contributions through calculating projected Crystal Orbital Hamilton Population (pCOHP) and integration of Crystal Orbital Hamilton Population (ICOHP)

iii) Rigorous Investigation of Investigation of Networks Generated using Simulations[86] (R.I.N.G.S.) 1.3.3 — Radial distribution function analysis; Available online: http://rings-code.sourceforge.net/index.php

iv) nMOLDYN[87] 3.0.1 — analyzing mean-square displacement (MSD) for molecular dynamics simulations

v) PACKMOL[88,89] 18.169 — creating initial configurations

vi) Bader Charge Analysis[90,91] 1.03 — individual atom charge analysis

vii) VTSTSCRIPTS-933[92,65] — commonly used scripts for dealing with the outputs from VASP; Available online from Henkelman group, University of Texas, Austin, TX, USA: http://theory.cm.utexas.edu

viii) VASPKIT[93] 0.72p1 — plotting the plane-averaged electron-density differences

Home-made codes

i) Extracting proton-bonded O index and positions from the AIMD trajectories (some detailed information and several main coding files can be found in the supplemental information at the end of this thesis),

ii) Calculating the diffusion coefficients from MSD results,

iii) Obtaining the dipole moment orientations and the OH bond orientations for all water molecules for each step along AIMD trajectories,

Detailed descriptions and original codes can be found online through my Github: https://github.com/LibbyXu/AIMD_DISS_CODING. Comments and suggestions are always highly welcomed.

Supporting Information

2.S1 Abbreviations

BO	Born-Oppenheimer approximation
HF	Hartree-Fock
CI	Configuration interaction

CC	Coupled-cluster
DFT	Density Functional Theory
XC	Exchange-correlation
LDA	Local-density approximation
GGA	Generalized gradient approximation
PW91	Perdew-Wang from 1991
PBE	Perdew-Burke-Ernzerhof
PP	Pseudopotential
PAW	Projector augmented wave methods
AIMD	*Ab-initio* molecular dynamics
MD	Molecular dynamics
CMD	Classical Molecular Dynamics
QM	Quantum Mechanics
MB	Maxwell-Boltzmann distribution
vdW	van der Waals
BJ	Becke-Johnson damping
(I/p)COHP	(Integral/projected) Crystal Orbital Hamilton Population
COOP	Crystal Orbital Overlap Population
DOS	Density of state
TST	Transition state theory
PES	Potential energy surface
NEB	Nudged Elastic Band

RDF	Radial distribution function
MSD	Mean square displacement

2.S2 Formulas

Num.	Formula
2.1	$\hat{H}_{total}\Psi_{total}(\vec{r},\vec{R}) = E\Psi_{total}(\vec{r},\vec{R})$
2.2	$\hat{H}_{total} = \hat{T}_{ele} + \hat{T}_{Nuc} + \hat{V}_{ele-ele} + \hat{V}_{Nuc-ele} + \hat{V}_{Nuc-Nuc}$
2.3	$\Psi_{total}(\vec{r},\vec{R}) = \Psi_{ele}(\vec{r},\vec{R})\Psi_{Nuc}(\vec{R})$
2.4	$\hat{H}_{ele}\Psi_{ele}(\vec{r},\vec{R}) = E_{ele}\Psi_{ele}(\vec{r},\vec{R})$
2.5	$\hat{H}_{ele} = \hat{T}_{ele} + \hat{V}_{ele-ele} + \hat{V}_{ext}$
2.6	$\rho(\vec{r}) = N\int\cdots\int\lvert\Psi_{ele}(\vec{r},\vec{r}_1,\vec{r}_2,\cdots,\vec{r}_N)\rvert^2\, d\vec{r}d\vec{r}_1\cdots d\vec{r}_N$
2.7	$E_0 = E[\rho_0(\vec{r})]$
2.8	$E[\rho_t(\vec{r})] \geq E[\rho_0(\vec{r})]$
2.9	$\left(-\frac{\hbar^2}{2m}\nabla^2 + v_{eff}(\vec{r})\right)\Phi_i(\vec{r}) = \epsilon_i\Phi_i(\vec{r})$
2.10	$v_{eff}(\vec{r}) = v_{ext}(\vec{r}) + \int\frac{\rho_0(\vec{r}')}{\lvert\vec{r}-\vec{r}'\rvert}d\vec{r}' + \frac{\delta E_{XC}[\rho_0(\vec{r})]}{\delta\rho_0(\vec{r})}$
2.11	$\rho_0(\vec{r}) = \sum_i^N \Phi_i^*(\vec{r})\Phi_i(\vec{r})$
2.12	$E(\rho_0(\vec{r})) = T_0(\rho_0(\vec{r})) + J(\rho_0(\vec{r})) + \int v_{ext}(\vec{r})\rho_0(\vec{r})d\vec{r} + E_{XC}(\rho_0(\vec{r}))$
2.13	$E_{XC}(\rho_0(\vec{r})) = E_X(\rho_0(\vec{r})) + E_C(\rho_0(\vec{r}))$
2.14	$\psi_i(\vec{r}) = exp(i\vec{k}\cdot\vec{r})u_i(\vec{r})$
2.15	$u_i(\vec{r}) = \sum_G c_{i,\vec{G}}\, exp(i\vec{G}\cdot\vec{r})$
2.16	$\psi_i(\vec{r}) = \sum_G c_{i,\vec{k}+\vec{G}}\, exp\{i(\vec{k}+\vec{G})\cdot\vec{r}\}$

2.17 $$M_I \ddot{\vec{R}}_I = -\nabla_I [\varepsilon_0(\vec{R}) + V_{N_{nuc}}(\vec{R})]$$

2.18 $$P(|\vec{p}|) = \left(\frac{\beta}{2\pi m}\right)^{\frac{2}{3}} exp\left(\frac{-\beta|\vec{p}|^2}{2m}\right), \qquad \beta = \frac{1}{k_B T}$$

2.19 $$\vec{p} = m\vec{v}$$

2.20 $$T = \frac{|\vec{p}|^2}{3mNk_B}$$

2.21 $$E_{DFT-D} = E_{KS} + E_{Disp-corr}$$

2.22 $$E_{Disp-corr} = -S_6 \sum_{I=1}^{N-1} \sum_{J=I+1}^{N} \frac{C_6^{IJ}}{R_{IJ}^{\ 6}} f_{damp}(R_{IJ})$$

2.23 $$E_{Disp-corr}^{DFT-D3} = -\sum_{I=1}^{N-1} \sum_{J=I+1}^{N} \sum_{n=6,8} \left[S_n \left(\frac{C_{n,IJ}}{R_{IJ}^n} \right) f_{n,damp}(R_{IJ}) \right]$$

2.24 $$f_{n,damp}^{D3-Zero}(R_{IJ}) = \left[1 + 6 \left(\frac{R_{IJ}}{S_{R,n} R_{0,IJ}} \right)^{-\alpha_n} \right]^{-1}$$

2.25 $$R_{0,IJ} = \sqrt{\frac{C_{8,IJ}}{C_{6,IJ}}}$$

2.26 $$f_{n,damp}^{D3-BJ}(R_{IJ}) = \frac{R_{IJ}^n}{R_{IJ}^n + \left(a_1 R_{0,IJ} + a_2\right)^n}$$

2.27 $$\nabla\rho(r_s) \cdot n(r_s) = 0$$

2.28 $$\mathrm{V}_{shell} = \frac{4}{3}\pi(r + dr)^3 - \frac{4}{3}\pi r^3 \approx 4\pi r^2 dr$$

2.29 $$g_{AB}(r) = \frac{dn_{AB}(r)}{4\pi\rho r^2 dr}$$

2.30 $$G_{AB}(r) = 4\pi \int_0^r r'^2 \, g_{AB}(r') dr'$$

2.31 $$N_{AB}(r) = \rho G_{AB}(r)$$

2.32 $$MSD(t) = \langle \boldsymbol{r}^2(\Delta t) \rangle = \langle (\boldsymbol{r_i}(\Delta t + t_0) - \boldsymbol{r_i}(t_0))^2 \rangle = \frac{1}{N} \sum_{i=1}^{N} (\boldsymbol{r_i}(\Delta t + t_0) - \boldsymbol{r_i}(t_0))^2$$

2.33 $$D = \lim_{t \to \infty} \frac{1}{2nt} \langle \boldsymbol{r}^2(\Delta t) \rangle = \frac{1}{2n} \frac{dMSD(t)}{dt}$$

References

(1) Born, M.; Oppenheimer, R. Zur Quantentheorie Der Molekeln. *Annalen der Physik* **1927**, *389* (20), 457–484. https://doi.org/10.1002/andp.19273892002.

(2) Ghosh, S.; Verma, P.; Cramer, C. J.; Gagliardi, L.; Truhlar, D. G. Combining Wave Function Methods with Density Functional Theory for Excited States. *Chemical reviews* **2018**, *118* (15), 7249–7292. https://doi.org/10.1021/acs.chemrev.8b00193

(3) Finkel, E. *Quantum Chemistry, (Levine, Ira N.)*; ACS Publications, 1993.

(4) Hasnip, P. J.; Refson, K.; Probert, M. I. J.; Yates, J. R.; Clark, S. J.; Pickard, C. J. Density Functional Theory in the Solid State. *Philos Trans A Math Phys Eng Sci* **2014**, *372* (2011). https://doi.org/10.1098/rsta.2013.0270.

(5) Gupta, V. P. *Principles and Applications of Quantum Chemistry*; Academic Press, 2015.

(6) Thomas, L. H. The Calculation of Atomic Fields. In *Mathematical Proceedings of the Cambridge Philosophical Society*; Cambridge University Press, 1927; Vol. 23, pp 542–548.

(7) Fermi, E. Eine Statistische Methode Zur Bestimmung Einiger Eigenschaften Des Atoms Und Ihre Anwendung Auf Die Theorie Des Periodischen Systems Der Elemente. *Zeitschrift für Physik* **1928**, *48* (1–2), 73–79. https://doi.org/10.1007/BF01351576

(8) Car, R. Introduction to Density-Functional Theory and *Ab-Initio* Molecular Dynamics. *Quantitative Structure-Activity Relationships* **2002**, *21* (2), 97–104. https://doi.org/10.1002/1521-3838(200207)21:2<97::AID-QSAR97>3.0.CO;2-6.

(9) Hohenberg, P.; Kohn, W. Inhomogeneous Electron Gas. *Phys. Rev.* **1964**, *136* (3B), B864–B871. https://doi.org/10.1103/PhysRev.136.B864.

(10) Slater, J. C. The Theory of Complex Spectra. *Phys. Rev.* **1929**, *34* (10), 1293–1322. https://doi.org/10.1103/PhysRev.34.1293.

(11) Mattsson, A. E.; Schultz, P. A.; Desjarlais, M. P.; Mattsson, T. R.; Leung, K. Designing Meaningful Density Functional Theory Calculations in Materials Science—a Primer. *Modelling Simul. Mater. Sci. Eng.* **2004**, *13* (1), R1–R31. https://doi.org/10.1088/0965-0393/13/1/R01.

(12) Kohn, W.; Sham, L. J. Self-Consistent Equations Including Exchange and Correlation Effects. *Phys. Rev.* **1965**, *140* (4A), A1133–A1138. https://doi.org/10.1103/PhysRev.140.A1133.

(13) Jensen, F. *Introduction to Computational Chemistry*; John wiley & sons, 2017.

(14) Perdew, J. P.; Burke, K.; Ernzerhof, M. Generalized Gradient Approximation Made Simple. *Phys. Rev. Lett.* **1996**, *77* (18), 3865–3868. https://doi.org/10.1103/PhysRevLett.77.3865.

(15) Ceperley, D. M.; Alder, B. J. Ground State of the Electron Gas by a Stochastic Method. *Physical review letters* **1980**, *45* (7), 566. http://dx.doi.org/10.1103/PhysRevLett.45.566.

(16) Gross, E. K.; Dreizler, R. M. *Density Functional Theory*; Springer Science & Business Media, 2013; Vol. 337.

(17) Foulkes, W. M. C.; Mitas, L.; Needs, R. J.; Rajagopal, G. Quantum Monte Carlo Simulations of Solids. *Reviews of Modern Physics* **2001**, *73* (1), 33. http://dx.doi.org/10.1103/RevModPhys.73.33.

(18) Burke, K.; Perdew, J. P.; Wang, Y. Derivation of a Generalized Gradient Approximation: The PW91 Density Functional. In *Electronic Density Functional Theory: Recent Progress and New Directions*; Dobson, J. F., Vignale, G., Das, M. P., Eds.; Springer US: Boston, MA, 1998; pp 81–111. https://doi.org/10.1007/978-1-4899-0316-7_7.

(19) Tavares, S. R.; Vaiss, V. S.; Antunes, F. P. N.; Fonseca, C. G.; Nangoi, I. M.; Moraes, P. I. R.; Soares, C. V.; Haddad, J. F. S.; Lima, L. L.; Silva, B. N. N.; Leitão, A. A. DFT Calculations for Structural Prediction and Applications of Intercalated Lamellar Compounds. *Dalton Trans.* **2018**, *47* (9), 2852–2866. https://doi.org/10.1039/C7DT03730A.

(20) Blöchl, P. E. Projector Augmented-Wave Method. *Physical review B* **1994**, *50* (24), 17953. https://dx.doi.org/10.1103/PhysRevB.50.17953.

(21) Kresse, G.; Joubert, D. From Ultrasoft Pseudopotentials to the Projector Augmented-Wave Method. *Physical review b* **1999**, *59* (3), 1758. http://dx.doi.org/10.1103/PhysRevB.59.1758.

(22) Kresse, G.; Furthmüller, J. Efficient Iterative Schemes for *Ab Initio* Total-Energy Calculations Using a Plane-Wave Basis Set. *Physical review B* **1996**, *54* (16), 11169. http://dx.doi.org/10.1103/PhysRevB.54.11169.

(23) Ashcroft, N. W.; Mermin, N. D. Solid State Physics (Saunders College, Philadelphia, 1976). *Appendix N* **2010**, *166*.

(24) Martin, R. M.; Martin, R. M. *Electronic Structure: Basic Theory and Practical Methods*; Cambridge university press, 2004.

(25) Monkhorst, H. J.; Pack, J. D. Special Points for Brillouin-Zone Integrations. *Physical review B* **1976**, *13* (12), 5188. http://dx.doi.org/10.1103/PhysRevB.13.5188.

(26) Dykstra, C. E. Electrostatic Interaction Potentials in Molecular Force Fields. *Chem. Rev.* **1993**, *93* (7), 2339–2353. https://doi.org/10.1021/cr00023a001.

(27) Hassanali, A. A.; Cuny, J.; Verdolino, V.; Parrinello, M. Aqueous Solutions: State of the Art in *Ab Initio* Molecular Dynamics. *Philosophical Transactions of the Royal Society A: Mathematical, Physical and Engineering Sciences* **2014**, *372* (2011), 20120482. https://doi.org/10.1098/rsta.2012.0482.

(28) Marx, D.; Hutter, J. *Ab Initio* Molecular Dynamics: Theory and Implementation. *Modern methods and algorithms of quantum chemistry* **2000**, *1* (301–449), 141.

(29) Iftimie, R.; Minary, P.; Tuckerman, M. E. *Ab Initio* Molecular Dynamics: Concepts, Recent Developments, and Future Trends. *Proceedings of the National Academy of Sciences* **2005**, *102* (19), 6654–6659. https://doi.org/10.1073/pnas.0500193102.

(30) Gibbs, J. W. *Elementary Principles in Statistical Mechanics: Developed with Especial Reference to the Rational Foundation of Thermodynamics*; C. Scribner's sons, 1902.

(31) Swendsen, R. *An Introduction to Statistical Mechanics and Thermodynamics*; Oxford University Press, USA, 2020.

(32) Frenkel, D.; Smit, B. *Understanding Molecular Simulation: From Algorithms to Applications*; Elsevier, 2001; Vol. 1.

(33) Kristyán, S.; Pulay, P. Can (Semi) Local Density Functional Theory Account for the London Dispersion Forces? *Chemical physics letters* **1994**, *229* (3), 175–180. https://doi.org/10.1016/0009-2614(94)01027-7.

(34) Pérez-Jordá, J.; Becke, A. D. A Density-Functional Study of van Der Waals Forces: Rare Gas Diatomics. *Chemical physics letters* **1995**, *233* (1–2), 134–137. https://doi.org/10.1016/0009-2614(94)01402-H.

(35) Antony, J.; Grimme, S. Density Functional Theory Including Dispersion Corrections for Intermolecular Interactions in a Large Benchmark Set of Biologically Relevant

Molecules. *Physical Chemistry Chemical Physics* **2006**, *8* (45), 5287–5293. https://doi.org/10.1039/B612585A.

(36) Grimme, S. Accurate Description of van Der Waals Complexes by Density Functional Theory Including Empirical Corrections. *Journal of computational chemistry* **2004**, *25* (12), 1463–1473. https://doi.org/10.1002/jcc.20078.

(37) Elstner, M.; Hobza, P.; Frauenheim, T.; Suhai, S.; Kaxiras, E. Hydrogen Bonding and Stacking Interactions of Nucleic Acid Base Pairs: A Density-Functional-Theory Based Treatment. *The Journal of Chemical Physics* **2001**, *114* (12), 5149–5155. https://doi.org/10.1063/1.1329889.

(38) Goursot, A.; Mineva, T.; Kevorkyants, R.; Talbi, D. Interaction between N-Alkane Chains: Applicability of the Empirically Corrected Density Functional Theory for van Der Waals Complexes. *Journal of chemical theory and computation* **2007**, *3* (3), 755–763. https://doi.org/10.1021/ct600373f.

(39) Grimme, S. Semiempirical GGA-type Density Functional Constructed with a Long-range Dispersion Correction. *Journal of computational chemistry* **2006**, *27* (15), 1787–1799. https://doi.org/10.1002/jcc.20495.

(40) Grimme, S.; Antony, J.; Ehrlich, S.; Krieg, H. A Consistent and Accurate *Ab Initio* Parametrization of Density Functional Dispersion Correction (DFT-D) for the 94 Elements H-Pu. *The Journal of chemical physics* **2010**, *132* (15), 154104. https://doi.org/10.1063/1.3382344.

(41) Chai, J.-D.; Head-Gordon, M. Long-Range Corrected Hybrid Density Functionals with Damped Atom–Atom Dispersion Corrections. *Physical Chemistry Chemical Physics* **2008**, *10* (44), 6615–6620. https://doi.org/10.1039/B810189B.

(42) Becke, A. D.; Johnson, E. R. A Density-Functional Model of the Dispersion Interaction. *The Journal of chemical physics* **2005**, *123* (15), 154101. https://doi.org/10.1063/1.2065267.

(43) Grimme, S.; Ehrlich, S.; Goerigk, L. Effect of the Damping Function in Dispersion Corrected Density Functional Theory. *Journal of computational chemistry* **2011**, *32* (7), 1456–1465. https://doi.org/10.1002/jcc.21759.

(44) Johnson, E. R.; Becke, A. D. A Post-Hartree–Fock Model of Intermolecular Interactions. *The Journal of chemical physics* **2005**, *123* (2), 024101. https://doi.org/10.1063/1.1949201.

(45) Tang, W.; Sanville, E.; Henkelman, G. A Grid-Based Bader Analysis Algorithm without Lattice Bias. *Journal of Physics: Condensed Matter* **2009**, *21* (8), 084204. https://iopscience.iop.org/article/10.1088/0953-8984/21/8/084204a.

(46) Sanville, E.; Kenny, S. D.; Smith, R.; Henkelman, G. Improved Grid-based Algorithm for Bader Charge Allocation. *Journal of computational chemistry* **2007**, *28* (5), 899–908. https://doi.org/10.1002/jcc.20575.

(47) Bader, R. F. W. *Atoms in Molecules: A Quantum Theory*; Clarendon Press, USA, 1990.

(48) Henkelman, G.; Arnaldsson, A.; Jónsson, H. A Fast and Robust Algorithm for Bader Decomposition of Charge Density. *Computational Materials Science* **2006**, *36* (3), 354–360. https://doi.org/10.1016/j.commatsci.2005.04.010.

(49) Bader, R. F.; Hernández-Trujillo, J.; Cortés-Guzmán, F. Chemical Bonding: From Lewis to Atoms in Molecules. *Journal of computational chemistry* **2007**, *28* (1), 4–14. https://doi.org/10.1002/jcc.20528.

(50) Bader, R. F. W.; MacDougall, P. J.; Lau, C. D. H. Bonded and Nonbonded Charge Concentrations and Their Relation to Molecular Geometry and Reactivity. *Journal of the american Chemical Society* **1984**, *106* (6), 1594–1605. https://doi.org/10.1021/ja00318a009.

(51) Maintz, S.; Deringer, V. L.; Tchougréeff, A. L.; Dronskowski, R. Analytic Projection from Plane-wave and PAW Wavefunctions and Application to Chemical-bonding Analysis in Solids. *Journal of computational chemistry* **2013**, *34* (29), 2557–2567. https://doi.org/10.1002/jcc.23424.

(52) Deringer, V. L.; Tchougréeff, A. L.; Dronskowski, R. Crystal Orbital Hamilton Population (COHP) Analysis As Projected from Plane-Wave Basis Sets. *J. Phys. Chem. A* **2011**, *115* (21), 5461–5466. https://doi.org/10.1021/jp202489s.

(53) Hoffmann, R. Solids and Surfaces: A Chemist's View of Bonding in Extended Structures. VCH Publ. *Inc., New York* **1988**.

(54) Chakraborty, J. Interplay of Covalency, Spin-Orbit Coupling, and Geometric Frustration in the $d^{3.5}$ System $Ba_3LiIr_2O_9$. *Physical Review B* **2018**, *97* (23), 235147. http://dx.doi.org/10.1103/PhysRevB.97.235147.

(55) Hao, Y.; Wang, Y.-T.; Xu, L.-C.; Yang, Z.; Liu, R.; Li, X. 1T-MoS_2 Monolayer Doped with Isolated Ni Atoms as Highly Active Hydrogen Evolution Catalysts: A Density Functional Study. *Applied Surface Science* **2019**, *469*, 292–297. https://dx.doi.org/10.1016/j.apsusc.2018.11.040.

(56) Steinberg, S.; Dronskowski, R. The Crystal Orbital Hamilton Population (COHP) Method as a Tool to Visualize and Analyze Chemical Bonding in Intermetallic Compounds. *Crystals* **2018**, *8* (5), 225. https://doi.org/10.3390/cryst8050225.

(57) Laidler, K. J.; King, M. C. Development of Transition-State Theory. *The Journal of physical chemistry* **1983**, *87* (15), 2657–2664. https://doi.org/10.1021/j100238a002.

(58) Eyring, H. The Activated Complex in Chemical Reactions. *The Journal of Chemical Physics* **1935**, *3* (2), 107–115. https://doi.org/10.1063/1.1749604.

(59) Carr, J. M.; Trygubenko, S. A.; Wales, D. J. Finding Pathways between Distant Local Minima. *The Journal of Chemical Physics* **2005**, *122* (23), 234903. https://doi.org/10.1063/1.1931587.

(60) Koslover, E. F.; Wales, D. J. Comparison of Double-Ended Transition State Search Methods. *The Journal of Chemical Physics* **2007**, *127* (13), 134102. https://doi.org/10.1063/1.2767621.

(61) Munro, L. J.; Wales, D. J. Defect Migration in Crystalline Silicon. *Physical Review B* **1999**, *59* (6), 3969. http://dx.doi.org/10.1103/PhysRevB.59.3969.

(62) Kumeda, Y.; Wales, D. J.; Munro, L. J. Transition States and Rearrangement Mechanisms from Hybrid Eigenvector-Following and Density Functional Theory.: Application to C10H10 and Defect Migration in Crystalline Silicon. *Chemical physics letters* **2001**, *341* (1–2), 185–194. https://doi.org/10.1016/S0009-2614(01)00334-7.

(63) Trygubenko, S. A.; Wales, D. J. A Doubly Nudged Elastic Band Method for Finding Transition States. *The Journal of chemical physics* **2004**, *120* (5), 2082–2094. https://doi.org/10.1063/1.1636455.

(64) Henkelman, G.; Jónsson, H. Improved Tangent Estimate in the Nudged Elastic Band Method for Finding Minimum Energy Paths and Saddle Points. *The Journal of chemical physics* **2000**, *113* (22), 9978–9985. https://doi.org/10.1063/1.1323224.

(65) Henkelman, G.; Uberuaga, B. P.; Jónsson, H. A Climbing Image Nudged Elastic Band Method for Finding Saddle Points and Minimum Energy Paths. *The Journal of chemical physics* **2000**, *113* (22), 9901–9904. https://doi.org/10.1063/1.1329672.

(66) Mills, G.; Jónsson, H. Quantum and Thermal Effects in H_2 Dissociative Adsorption: Evaluation of Free Energy Barriers in Multidimensional Quantum Systems. *Physical review letters* **1994**, *72* (7), 1124. http://dx.doi.org/10.1103/PhysRevLett.72.1124.

(67) Fung, V. Alkane Conversion on Heterogeneous Catalysts From First Principles and Descriptors, UC Riverside, 2019. ProQuest ID: Fung_ucr_0032D_13716. Merritt ID: ark:/13030/m5r54t5m. Retrieved from https://escholarship.org/uc/item/6zx9c73p

(68) Maragakis, P.; Andreev, S. A.; Brumer, Y.; Reichman, D. R.; Kaxiras, E. Adaptive Nudged Elastic Band Approach for Transition State Calculation. *J. Chem. Phys.* **2002**, *117* (10), 4651–4658. https://doi.org/10.1063/1.1495401.

(60) Chandler, D. Introduction to Modern Statistical. *Mechanics. Oxford University Press, Oxford, UK* **1987**.

(70) Frenkel, D.; Smit, B. *Understanding Molecular Simulation: From Algorithms to Applications*; Elsevier, 2001; Vol. 1.

(71) Michalet, X. Mean Square Displacement Analysis of Single-Particle Trajectories with Localization Error: Brownian Motion in an Isotropic Medium. *Physical Review E* **2010**, *82* (4), 041914. http://dx.doi.org/10.1103/PhysRevE.82.041914.

(72) Keffer, D. The Working Man's Guide to Obtaining Self Diffusion Coefficients from Molecular Dynamics Simulations. *Department of Chemical Engineering, University of Tennessee, Knoxville, USA* **2001**.

(73) Sun, Y.; Zhan, C.; Kent, P. R.; Naguib, M.; Gogotsi, Y.; Jiang, D. Proton Redox and Transport in MXene-Confined Water. *ACS Applied Materials & Interfaces* **2019**. https://doi.org/10.1021/acsami.9b18139.

(74) Fischer, S. A.; Dunlap, B. I.; Gunlycke, D. Correlated Dynamics in Aqueous Proton Diffusion. *Chemical science* **2018**, *9* (35), 7126–7132. https://doi.org/10.1039/C8SC01253A.

(75) Hall, D.; Hoshino, M. Effects of Macromolecular Crowding on Intracellular Diffusion from a Single Particle Perspective. *Biophysical reviews* **2010**, *2* (1), 39–53. https://doi.org/10.1007/s12551-010-0029-0.

(76) Ushida, K.; Masuda, A. General Importance of Anomalous Diffusion in Biological Inhomogeneous Systems. *Handai Nanophotonics* **2007**, *3*, 175. https://dx.doi.org/10.1016/s1574-0641(07)80016-7.

(77) Mocanu, G. R. Mean Square Displacement and Instantaneous Diffusion Coefficient of Charged Particles in Stochastic Motion. *arXiv preprint arXiv:1906.10402* **2019**. https://arxiv.org/abs/1906.10402.

(78) Pestana, L. R.; Mardirossian, N.; Head-Gordon, M.; Head-Gordon, T. *Ab Initio* Molecular Dynamics Simulations of Liquid Water Using High Quality Meta-GGA Functionals. *Chemical science* **2017**, *8* (5), 3554–3565. https://doi.org/10.1039/C6SC04711D.

(79) Humphrey, W.; Dalke, A.; Schulten, K. VMD: Visual Molecular Dynamics. *Journal of molecular graphics* **1996**, *14* (1), 33–38. https://doi.org/10.1016/0263-7855(96)00018-5.

(80) Schaftenaar, G.; Noordik, J. H. Molden: A Pre-and Post-Processing Program for Molecular and Electronic Structures. *Journal of computer-aided molecular design* **2000**, *14* (2), 123–134. https://doi.org/10.1023/A:1008193805436.

(81) Momma, K.; Izumi, F. VESTA 3 for Three-Dimensional Visualization of Crystal, Volumetric and Morphology Data. *Journal of applied crystallography* **2011**, *44* (6), 1272–1276. https://dx.doi.org/10.1107/S0021889811038970.

(82) Hanwell, M. D.; Curtis, D. E.; Lonie, D. C.; Vandermeersch, T.; Zurek, E.; Hutchison, G. R. Avogadro: An Advanced Semantic Chemical Editor, Visualization, and Analysis Platform. *Journal of cheminformatics* **2012**, *4* (1), 17. https://doi.org/10.1186/1758-2946-4-17.

(83) Maintz, S.; Deringer, V. L.; Tchougréeff, A. L.; Dronskowski, R. LOBSTER: A Tool to Extract Chemical Bonding from Plane-wave Based DFT. *Journal of computational chemistry* **2016**, *37* (11), 1030–1035. https://doi.org/10.1002/jcc.24300.

(84) Maintz, S.; Esser, M.; Dronskowski, R. Efficient Rotation of Local Basis Functions Using Real Spherical Harmonics. *Acta Physica Polonica B* **2016**, *47* (4). https://www.actaphys.uj.edu.pl/R/47/4/1165/pdf.

(85) Maintz, S.; Deringer, V. L.; Tchougréeff, A. L.; Dronskowski, R. Analytic Projection from Plane-wave and PAW Wavefunctions and Application to Chemical-bonding Analysis in Solids. *Journal of computational chemistry* **2013**, *34* (29), 2557–2567. https://doi.org/10.1002/jcc.23424.

(86) Le Roux, S.; Jund, P. Ring Statistics Analysis of Topological Networks: New Approach and Application to Amorphous GeS2 and SiO2 Systems. *Computational Materials Science* **2010**, *49* (1), 70–83. https://doi.org/10.1016/j.commatsci.2010.04.023.

(87) Róg, T.; Murzyn, K.; Hinsen, K.; Kneller, G. R. NMoldyn: A Program Package for a Neutron Scattering Oriented Analysis of Molecular Dynamics Simulations. *Journal of computational chemistry* **2003**, *24* (5), 657–667. https://doi.org/10.1002/jcc.10243.

(88) Martínez, J. M.; Martínez, L. Packing Optimization for Automated Generation of Complex System's Initial Configurations for Molecular Dynamics and Docking. *Journal of computational chemistry* **2003**, *24* (7), 819–825. https://doi.org/10.1002/jcc.10216.

(89) Martínez, L.; Andrade, R.; Birgin, E. G.; Martínez, J. M. PACKMOL: A Package for Building Initial Configurations for Molecular Dynamics Simulations. *Journal of computational chemistry* **2009**, *30* (13), 2157–2164. https://doi.org/10.1002/jcc.21224.

(90) Tang, W.; Sanville, E.; Henkelman, G. A Grid-Based Bader Analysis Algorithm without Lattice Bias. *Journal of Physics: Condensed Matter* **2009**, *21* (8), 084204. https://iopscience.iop.org/article/10.1088/0953-8984/21/8/084204/meta.

(91) Yu, M.; Trinkle, D. R. Accurate and Efficient Algorithm for Bader Charge Integration. *The Journal of chemical physics* **2011**, *134* (6), 064111. https://doi.org/10.1063/1.3553716.

(92) Sheppard, D.; Terrell, R.; Henkelman, G. Optimization Methods for Finding Minimum Energy Paths. *The Journal of chemical physics* **2008**, *128* (13), 134106. https://doi.org/10.1063/1.2841941.

(93) Ve, W,; Nan, X.; Jin-Cheng, L. VASPKIT: A Pre- and Post-Processing Program for the VASP Code. http://vaspkit.sourceforge.net.

Chapter 3

Understanding hydrogen in perovskites from first principles

3.1 Abstract

The behavior of hydrogen in oxides is important to understand their functions; for example, some perovskites are fast proton conductors. Herein we study geometry, energetics, chemical bonding, and transport behaviors of hydrogen in ABO_3 perovskites from first principles. We find that hydrogen absorption to lattice oxygen, as well as hydrogen diffusion process inside bulk systems, leads to structure distortion, especially in the (100) BO_2 plane, and ~1.5% volume expansion. Density-of-states (DOS) and crystal orbital Hamilton population (COHP) analyses indicate that the electron from hydrogen

occupies the lower-lying states in the conduction band which corresponds to the B-O antibonding states and thereby weakens the B-O covalent bonding. More interestingly, oxygen vacancy formation energy (OVFE), the Integrated COHP of the B-O bond, and the electronegativity difference (ΔX_{B-A}) are all found to be useful descriptors that correlate with hydrogen absorption energy (HAE).

3.2 Introduction

Hydrogen can exist as a proton inside oxide materials[1–3]. Some of these proton-containing oxide materials are used as proton conductors for batteries, fuel cells, and electrochemical sensors[2,4–6]. For example, Iwahara *et al.* found that certain perovskites such as Y-doped $SeCeO_3$ exhibited high proton conductivity/permeability at elevated temperatures[7–9]. This discovery sparked sustained interest in proton conductivity in perovskites.

Perovskite is a prominent class of mixed metal oxides with formula ABO_3, where A-site and B-site cations are 12-fold and octahedrally 6-fold coordinated with the oxygen atoms, respectively. The majority of the metallic ions in the periodic table can be taken as a brick of perovskites and different compositions represent different physical and chemical properties. In recent years, researchers have tried to correlate proton conductivity in perovskites to their structure. Mitsui *et al.* linked the kinetic properties for proton diffusion and conductivity in several perovskites to their structural parameters, e.g., lattice constants[10]. Norby *et al.* searched for empirical correlations between thermodynamic

properties and material-specific parameters to predict the hydration enthalpy and the predominance of oxide ion (or proton) conduction in the materials[1,11]. Bork *et al.* investigated hydrogen/proton dynamics in series of undoped perovskites and created a design methodology for a doped perovskite with desired proton mobility or binding energy[12]. M. Wohlfahrt-Mehrens *et al.* reported that the mobility of the protons in the host lattice of the metal-doped $SrRuO_3$ dominated the electrochemical redox capacity processes[13].

Despite previous explorations, detailed geometric, electronic-structure changes, and inner-diffusion behavior due to hydrogen in perovskites are still unclear. To address this issue, we here study geometry, energetics, electronic structure, and transport phenomenon from the perspective of hydrogen absorption inside perovskites using density functional theory (DFT). The change to nature chemical-bonding in perovskites due to hydrogen absorption is then analyzed via the crystal orbital Hamiltonian populations (COHP) and density-of-states (DOS). Then, the energetic and electronic-structure descriptors are explored to leverage the variability of A and B ions in perovskites. Moreover, the transport path and the energy barrier due to the motion of hydrogen will be illustrated by the Nudged-elastic band (NEB) methodology. Below, we first describe the computational methods used.

3.3 Computational methods

Spin-polarized density functional theory (DFT) calculations were performed using the plane-wave pseudopotential method as implemented in the Vienna *ab initio* simulation

package (VASP)[14,15]. The electron-ion interactions were described by the projector augmented-wave (PAW)[16,17] methods while the electron exchange-correlation part was parameterized by the Perdew-Burke-Ernzerhof (PBE)[18] functional form of generalized gradient approximation (GGA). A cutoff energy of 450 eV was used for the plane-wave basis set. The 2×2×2 ABO_3 supercell of approximately 8 Å in lattice parameter and containing 40 atoms were used for hydrogen absorption; its Brillouin zone was sampled by a 5×5×5 Monkhorst-Pack k-point mesh[19]. All ionic positions in the unit cell and the lattice columns were allowed during structure optimizations. The convergence criteria are 0.025 eV/ Å in force and 2.5×10^{-4} eV in energy. Table 3.1 shows the good agreement between DFT-PBE and literatures[20–22] for the lattice constants.

Table 3.1 Calculated cubic unit-cell lattice constants compared to literature data[20–22]

System	Cubic unit-cell lattice constants		
	Literature [Å]	DFT-PBE [Å]	Deviation [%]
$BaTiO_3$	4.036	4.028	0.215
$BaCuO_3$	4.004	4.006	0.051
$BaZrO_3$	4.256	4.243	0.318
$BaMoO_3$	4.149	4.073	1.827
$BaHfO_3$	4.204	4.196	0.199
$SrTiO_3$	3.945	3.941	0.100
$SrVO_3$	3.901	3.857	1.134
$SrCrO_3$	3.893	3.845	1.237
$SrMnO_3$	3.882	3.840	1.080
$SrFeO_3$	3.913	3.845	1.740
$SrCoO_3$	3.863	3.834	0.759
$SrNiO_3$	3.886	3.845	1.056
$SrCuO_3$	3.885	3.880	0.137

The hydrogen absorption energies (E_{HAE}) and the oxygen vacancy formation energy (E_{OVFE}) based on the 2×2×2 ABO_3 supercell were determined by the following expressions:

$$E_{HAE} = E_{Bulk+H} - E_{Bulk} - \frac{1}{2}E_{H_2} \tag{3.1}$$

$$E_{OVFE} = E_{Bulk-O} + \frac{1}{2}E_{O_2} - E_{Bulk} \tag{3.2}$$

where E_{Bulk+H} and E_{Bulk-O} are the total energies of the perovskite supercell with one absorbed hydrogen atom and one oxygen vacancy, respectively; E_{Bulk} is the total energy of the perovskite; E_{H_2} and E_{O_2} represent the total energies of a gas phase H_2 and O_2 molecule, respectively. Relaxed geometries were used for all computed energies.

To reveal the bonding nature of different perovskites, the crystal orbital Hamiltonian populations (COHP) was performed using the standalone computer program Local Orbital Basis Suite towards Electronic-Structure Reconstruction (LOBSTER)[23–25].

The electronegativity difference (ΔX_{B-A}) for the perovskites (ABO_3) is determined as:

$$\Delta X_{B-A} = X_B - X_A \tag{3.3}$$

where X_A, X_B denotes the Allred-Rochow electronegativity[26,27] of cations A and B, respectively, in perovskites. It is also important to mention that A and B are mainly 3d or 4d transition metals.

To study the minimum-energy paths and transition-state (TS) energy barriers for the hydrogen migration between different O sites inside bulk perovskites, the Climbing-

image Nudged-elastic approach (CI-NEB) implemented in VASP package[28] will be employed with the same convergence criteria used in above structure optimizations.

3.4 Results and discussions

Hydrogen as an interstitial dopant inside a bulk perovskite prefers to bind with lattice oxygen to form a hydroxyl group. As in the case of surface adsorption, the H in the hydroxyl group can be viewed as a proton, while the accompanying electron reduces the B ion in ABO_3. We first examine structural change induced to perovskite structure after H absorption.

3.4.1 Change of geometric structure after H absorption

Figure. 3.1 shows the percent change of the supercell volume after hydrogen absorption. The average change is about 1%, while $BaTiO_3$ and $SrNiO_3$ are the exceptions and have > 2.5% changes. Using $SrTiO_3$ as an example, Figure 3.2 presents the change in atomic positions before and after hydrogen absorption. At the most stable site, the H atom forms a hydroxyl group with one lattice oxygen in the (100) TiO_2 plane, while interacting strongly with nearby oxygen atoms. This interaction deforms lattice by shortening the distances between hydrogen and its neighboring oxygens.

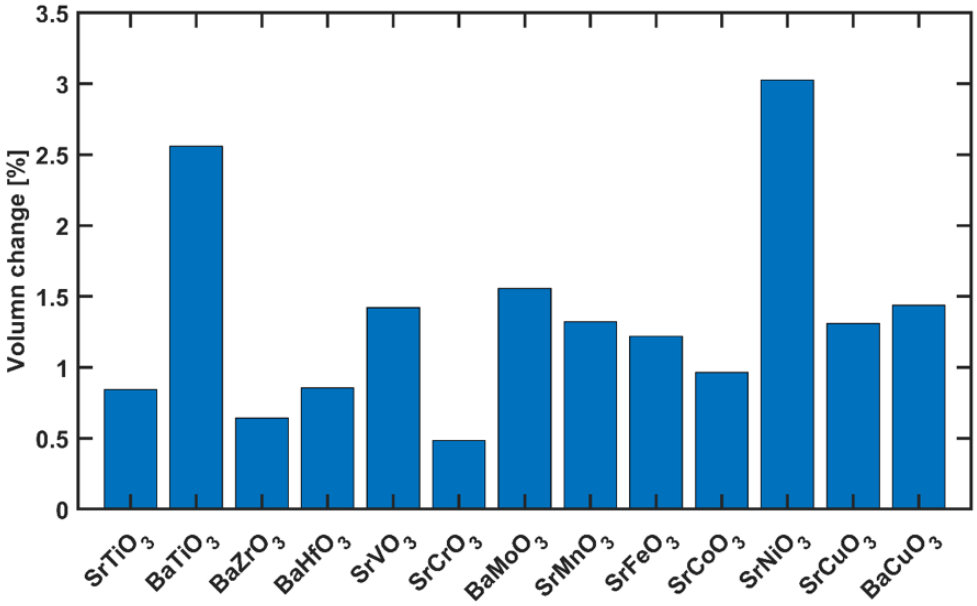

Figure 3.1. Volume change after hydrogen absorption in various perovskites.

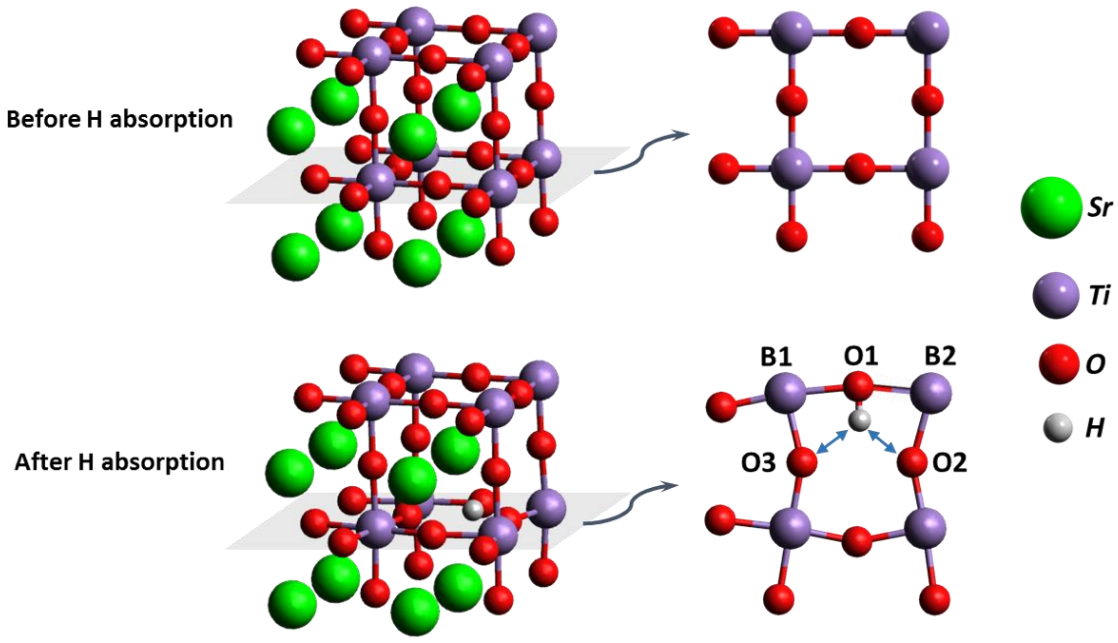

Figure 3.2 The optimized $SrTiO_3$ structures before and after hydrogen absorption. The (100) TiO_2 plane where hydrogen is located shaded in gray.

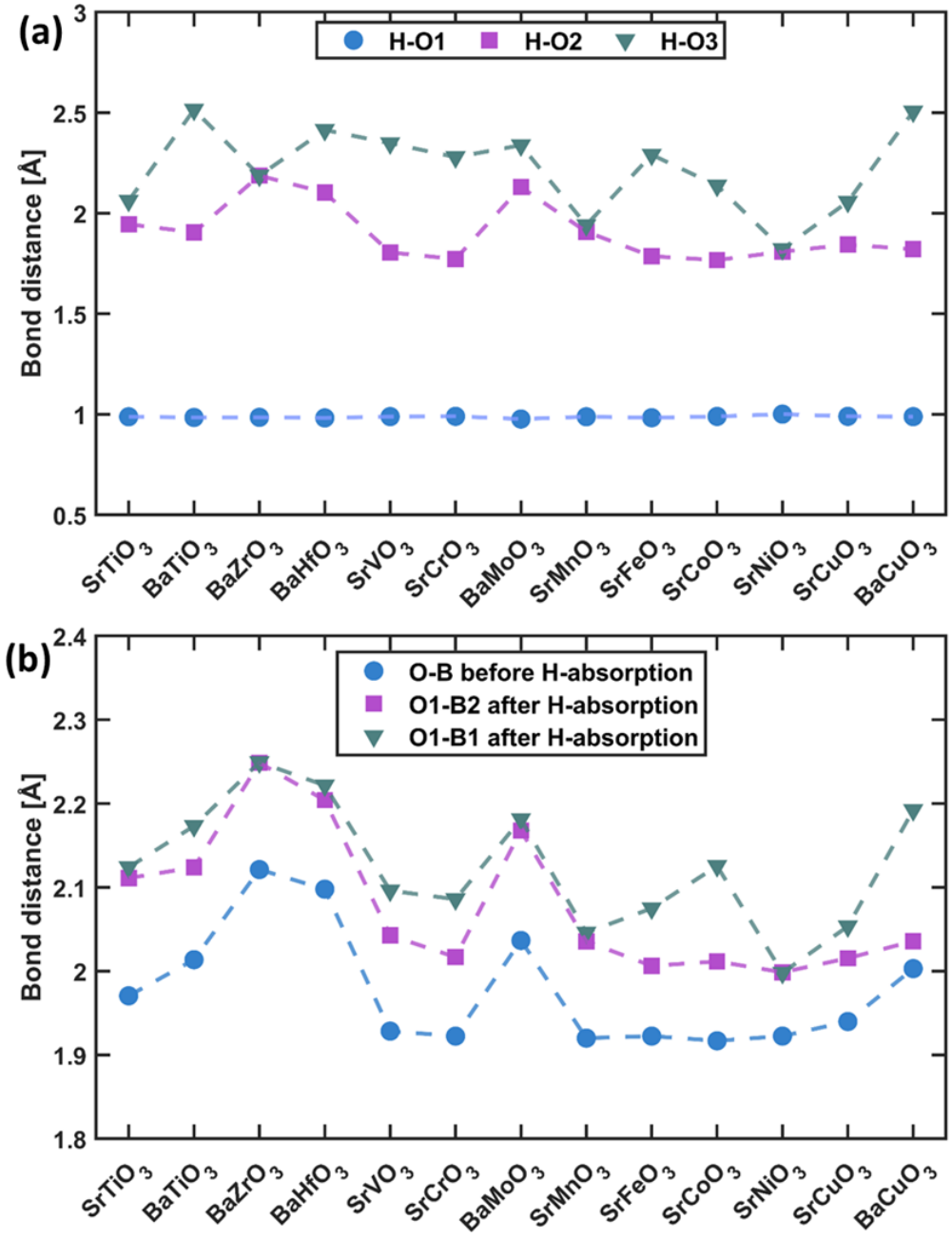

Figure 3. 3 **(a)** Variations of O-H distances inside the perovskites; **(b)** variations of B-O bond distances before and after hydrogen absorption. See Figure. 3.2 for labels of the O atoms.

Figure. 3.3(a) illustrates the variations of the O-H distances inside the perovskites under investigation. The O-H1 distance varies very little with different compositions of perovskites. For the distance of the H-O2 and H-O3, they are both within the range of 1.8~2.5 Å and contributing to the stabilization of proton inside perovskites. However, in most cases, the H-O2 distance shorter than the H-O3 distance, indicating that the O1-H bond tilts toward O2. This inclination influences the two neighboring B-O bond distances of the OH bond as shown in Figure. 3.3(b): the B-O bond distances increase after H absorption; the O1-B2 bond distances are slightly smaller than the O1-B1 bonds. Similar distance shortening phenomenon and structure distortions were also reported from other oxides systems[11,29–32].

3.4.2 Electronic structures and chemical bonding

The geometric changes after hydrogen absorption and the formation of the OH bond can also affect the electronic structure of the B-O bonds. In pristine perovskites, B and O form a polar covalent bond through hybridization of O 2p-states and B d-states[33,34]. Our group previous study[35] shows that ICOHP will increase with the d–electron count in B, consistent with the weakening of the B-O bond across the row in the periodic table (Figure 3.S1). In our study, we compared the ICOHP of B-O bond before and after H absorption via the explanations of the electronic properties and corresponding bonding contributions. Here, the typical cubic perovskite $SrTiO_3$ will be used as the case study. As shown in Figure. 3.4(a), the conduction bands are mostly composed of the Ti-3d orbitals; after H absorption, the Ti-3d orbitals shift down. The crystal orbital Hamilton population (COHP)

plots in Figure. 3.4(b) show that there is a slight occupancy of the Ti-O antibonding states near the Fermi level (negative -COHP values). In other words, the Ti-O bonds are weakened after H absorption, which is consistent with the increase of the B-O distance (Figure. 3.3(b)). In addition, Figure 3.S2 shows that the ICOHP of the B-O bond is always larger than that before H absorption for all the perovskites under investigation in this work.

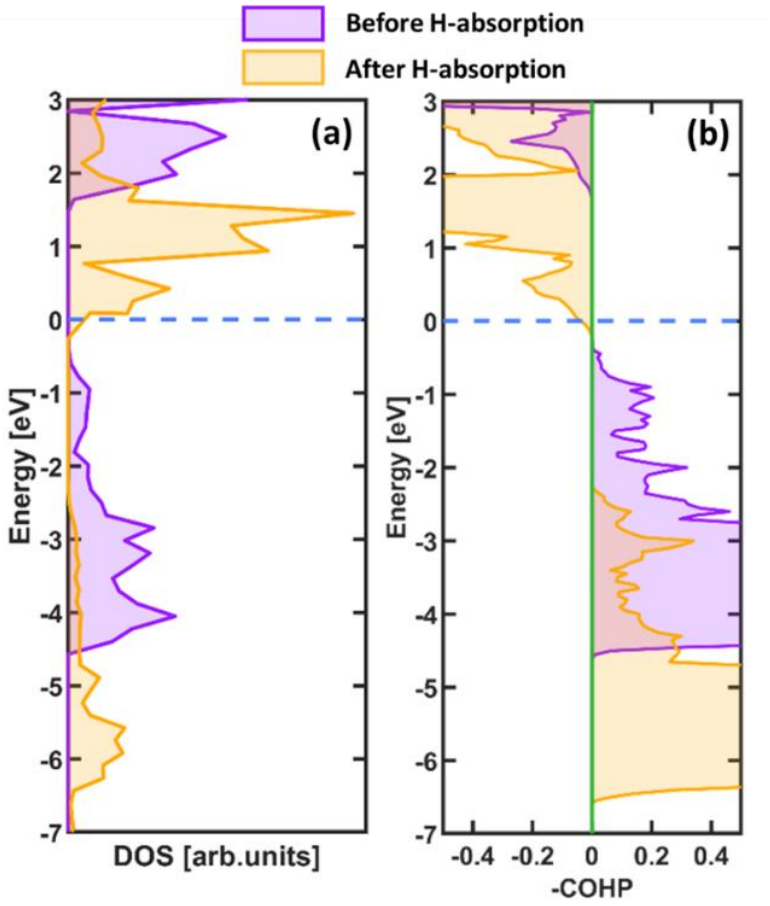

Figure 3.4 **(a)** Ti 3d-state partial density-of-states (DOS) before and after hydrogen absorption onto the oxygen-site of $SrTiO_3$. **(b)** –COHP plot of the local Ti-O bond before and after hydrogen absorption (negative and positive COHP corresponds to bonding and antibonding interactions, respectively).

3.4.3 Hydrogen absorption energy and descriptors

Hydrogen adsorption energy on surfaces has been found to be a highly useful energetic descriptor for their reactivity in catalysis[12,35–39]. Therefore, the hydrogen absorption energy (HAE) in perovskites could also be an important indicator of other properties of the perovskites. Here we first examine the correlation of HAE with the oxygen vacancy formation energy (OVFE). As shown in Figure. 3.5(a), a very good linear relationship is found. In other words, the smaller the OVFE, the more reducible the perovskite and the more reactive the lattice oxygen, so the more favorable the binding with hydrogen.

Previously it was found that the integrated crystal orbital Hamilton population (ICOHP) value can be used as a bulk descriptor to correlate with the reactivity of the surface oxygen toward hydrogen on perovskite surfaces[35]. Hence, here we use the B-O ICOHP values of perovskites to correlate with their reactivity toward H absorption. We found a good correlation between ICOHP and HAE as shown in Figure. 3.5(b). Less negative ICOHP values for the B-O bonds mean that the perovskites have less population of the B-O antibonding states, so the O atoms will be more reactive toward hydrogen, leading to more favorable interaction or more negative HAE. We also found that O1-H ICOHP (Figure 3.S3) stays roughly constant with respect to the HAE, showing that the change in HAE must be dominated by the B-O bond contributions.

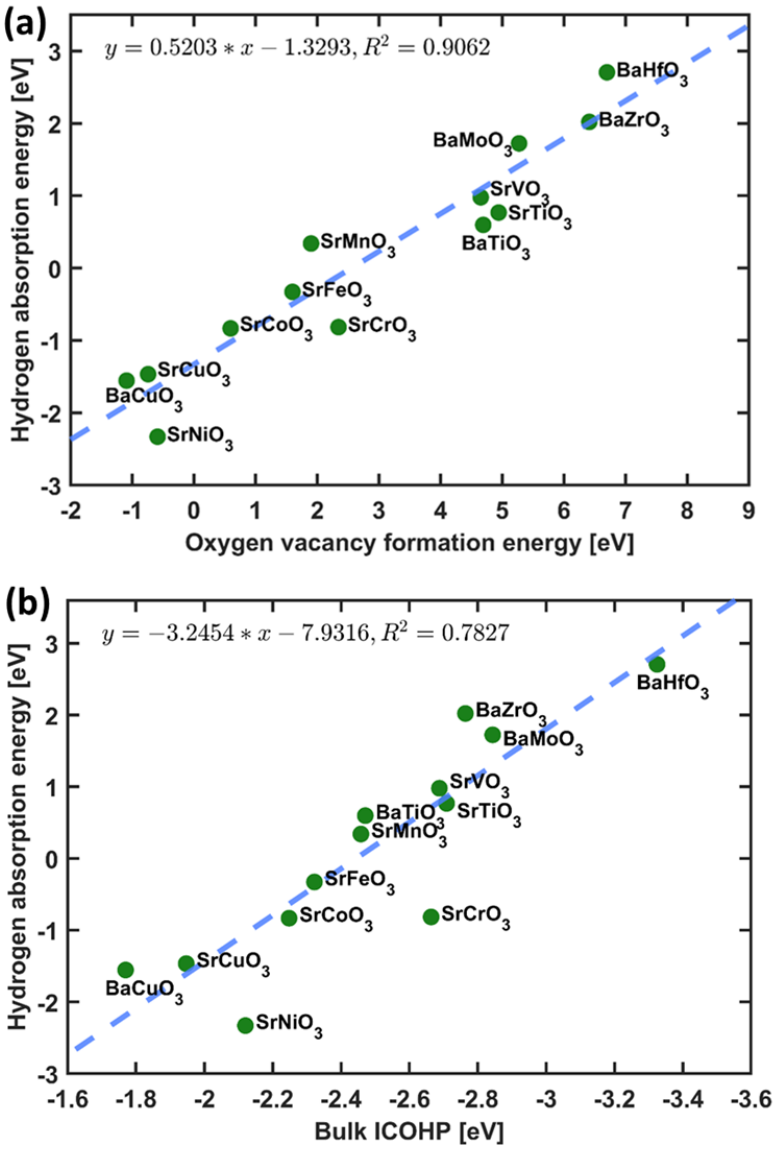

Figure 3.5 Correlation plots **(a)** between the hydrogen absorption energy (HAE) and the oxygen vacancy formation energy (OVFE) and **(b)** between the integrated crystal orbital Hamilton population (ICOHP) of the B-O bonds and HAE.

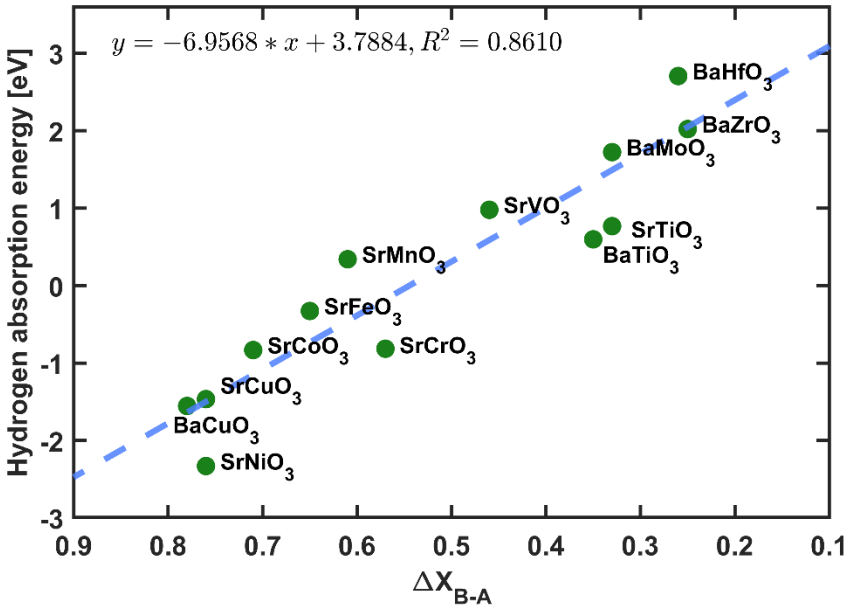

Figure 3.6 Correlation plot between the hydrogen absorption energy (HAE) and the electronegativity difference (ΔX_{B-A}) in ABO_3 perovskites.

Kreuer *et al.* proposed that the acid-base character of the cations play crucial roles in the proton mobility and the hydration processes in various perovskites[1,40,41]. The affinity for protons to the lattice O site inside the perovskites may vary with the chemical matching of A and B cations in perovskites (ABO_3). Therefore, we correlate the HAE with the electronegativity difference between B and A (ΔX_{B-A}). As shown in Figure. 3.6, the larger the electronegativity difference, the stronger (the more negative) the HAE. Since ΔX_{B-A} is mainly dictated by B, Figure. 3.6 means that the less electronegative the B cation, the stronger the bonding of B with O and then the less reactive the O toward hydrogen.

3.4.4 Hydrogen diffusion processes

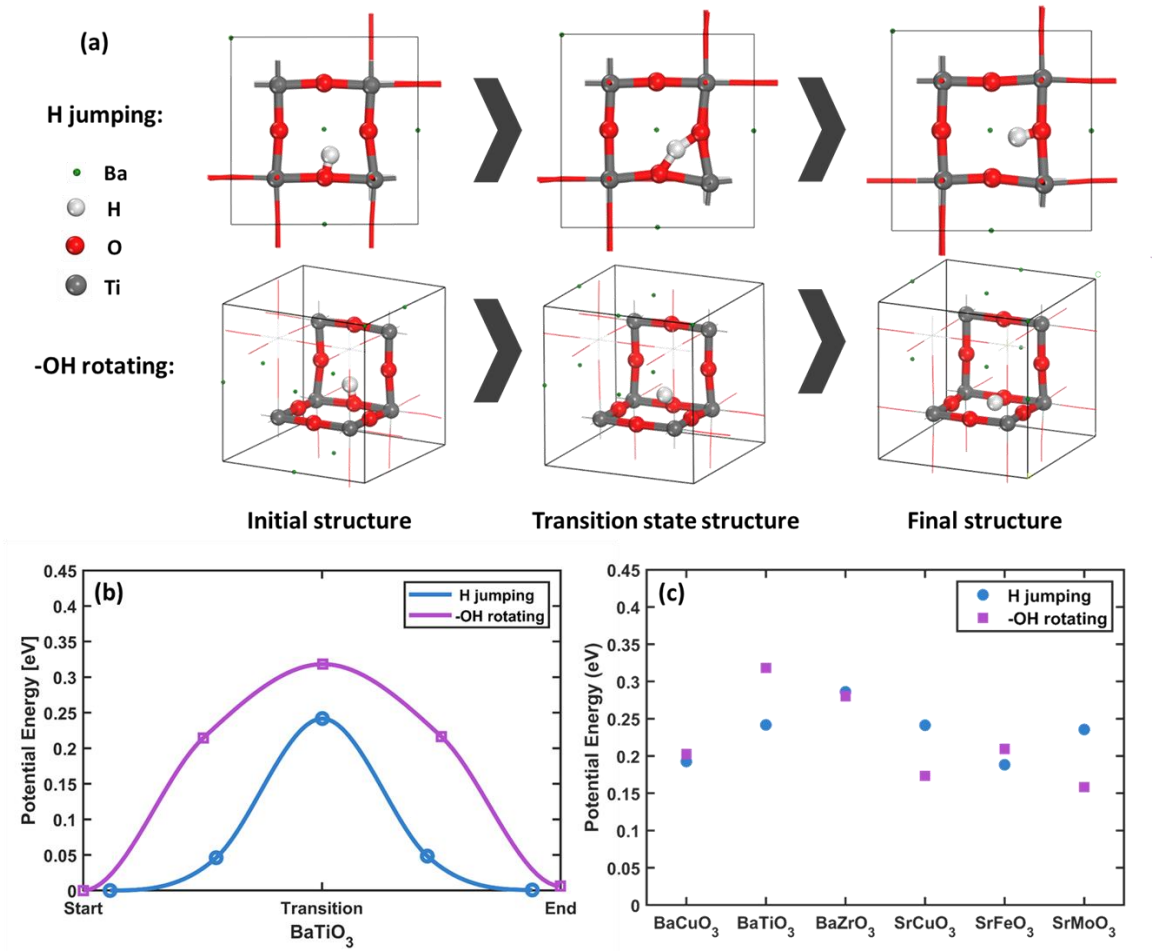

Figure 3.7 **(a)** The configurations illustrate the transition-state pathway (the initial, transition-state and final structures) for the H jumping and -OH rotating diffusion processes using $BaTiO_3$ as an example; **(b)** Illustration of the potential energy surface of the minimum-energy path for different diffusion processes in $BaTiO_3$. Makers indicate the images included in the actual CI-NEB calculations; **(c)** Potential energy barriers for two diffusion processes in 6 different perovskites out from the all.

There are two dominating hydrogen diffusion processes inside perovskites. One diffusion process is called “H jumping” —the H transfers within neighboring O sites, containing the breakage and reformation of the –OH bonds. Another process is the “H rotating” — the H reorients at the same O site. Using the $BaTiO_3$ as an instance, Figure

3.7(b) displays the potential energy surface of the minimum-energy path for different diffusion processes. The pathways are symmetrical about the transition state, and the structure distortions take place during the hydrogen transfer as shown in Figure 3.7(a). Here, we only studied the diffusion behaviors of 6 perovskites ($BaCuO_3$, $BaTiO_3$, $BaZrO_3$, $SrCuO_3$, $SrFeO_3$, and $SrMoO_3$ out from the all mentioned above), the potential energy barriers (Figure 3.7(c)) of "H jumping" and "-OH rotating" for the same perovskites are very small and close to each other. This result indicates an easy and faster hydrogen migration inside perovskites.

3.5 Conclusion

We have studied geometry, chemical bonding, energetics, and descriptors of hydrogen absorption in ABO_3 perovskites using density functional theory. We found that hydrogen formed a hydroxyl group with lattice oxygen, causing structural distortion mainly in the (100)-BO_2 plane and a volume increase of 0.5 to 3%. Density-of-states and crystal orbital Hamilton population (COHP) analyses indicated that the electron from hydrogen occupied the lower-lying states in the conduction band which corresponded to the B-O antibonding states, thereby weakening and lengthening the nearby B-O bonds. Oxygen vacancy formation energy (OVFE), the Integrated COHP of the B-O bond, and the electronegativity difference (ΔX_{B-A}) were found to be useful descriptors that correlate with hydrogen absorption energy (HAE). The low potential energy barriers of the "H jumping" and "-OH rotating" diffusion processes resulted in possible hydrogen migration inside

perovskites. This work provides fundamental insights into H in perovskites that may be useful for future studies of hydrogen intercalation and transport through perovskites.

Supporting information

3.S1 ICOHP of B-O bond with d-electron counts in B in $SrBO_3$

Figure 3.S1(a) illustrates that the ICOHP of B-O bond increases with d–electron counts in B in $SrBO_3$ perovskites, indicating the weakening of B-O bond across the row in the periodic table. Meanwhile, it is implied that the B-O covalent bonding contributes more than the ionic bonding. The downward shift of the antibonding states of B-O bond -COHP (-COHP and COHP correspond to bonding and antibonding state, respectively) due to additional d-election (Figure 3.S1(b)) further proves the increase of the ICOHP.

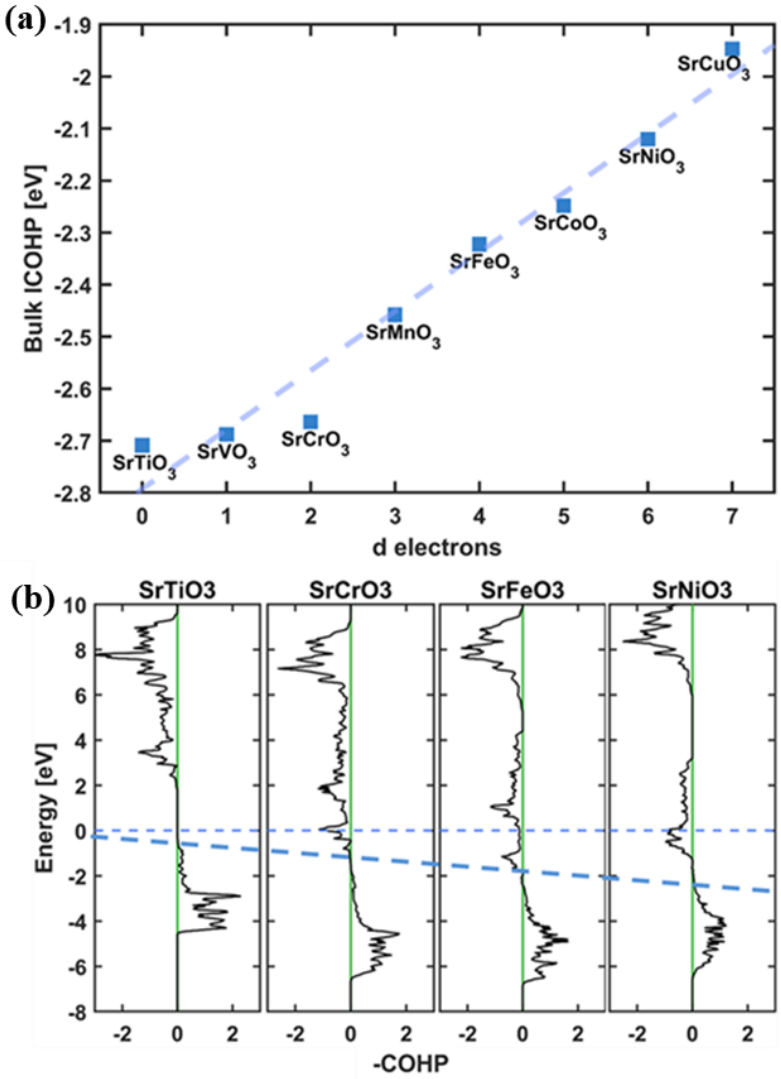

Figure 3.S1 **(a)** Averaged integrated crystal orbital Hamilton populations (ICOHP) of B-O bond in the pristine perovskites $SrBO_3$ with B being the 3d transition metals. **(b)** Negative crystal-orbital Hamilton population (-COHP) versus energy (relative to E_{Fermi}). The dashed dark blue line demonstrates the downshift of the separation point between the antibonding (negative -COHP) and bonding (positive -COHP) states.

3.S2 ICOHP of B-O bond after H absorption

Figure 3.S2 shows that the ICOHP of the B-O bond after H absorption is always larger than that before H absorption. This demonstrates the weakening of the B-O bond

after H absorption and the result is in line with the increased B-O bond distance (Figure 3.3(b)).

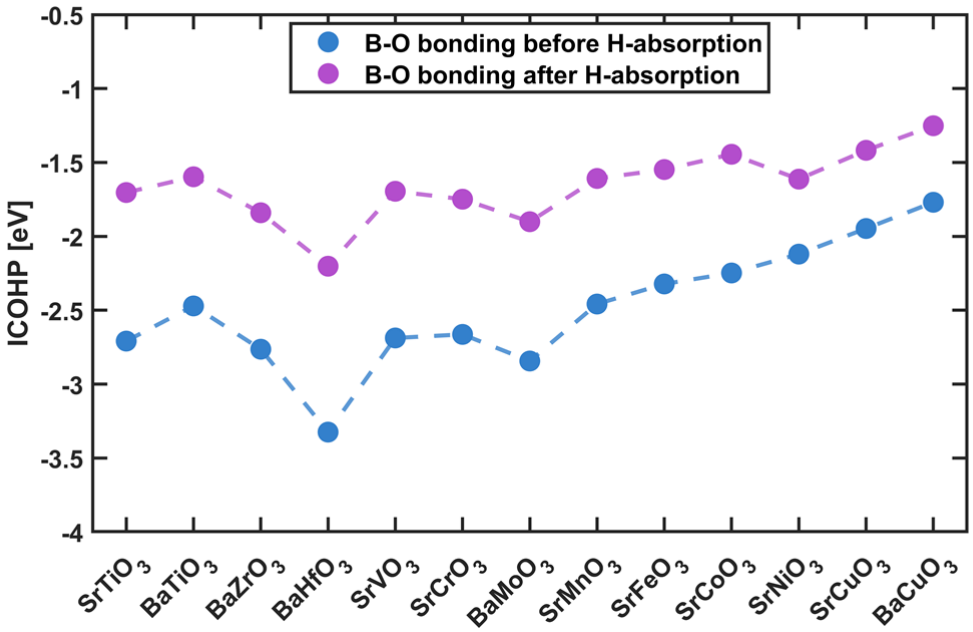

Figure 3.S2 Scatterplot of the ICOHP of the B-O bond before and after H absorption. Note that, the ICOHP value is averaged from the O1-B1 and O1-B2 bond after H absorption. See Figure 3.2 for labels of the O and B atoms.

3.S3 ICOHP of O1-H bond versus hydrogen absorption energy (HAE)

Figure 3.S3 suggests that the ICOHP of O1-H stays roughly constant with respect to the hydrogen absorption energy (HAE), illustrating that the change in HAE on different perovskites primarily derived from the reduction of the B-O bond.

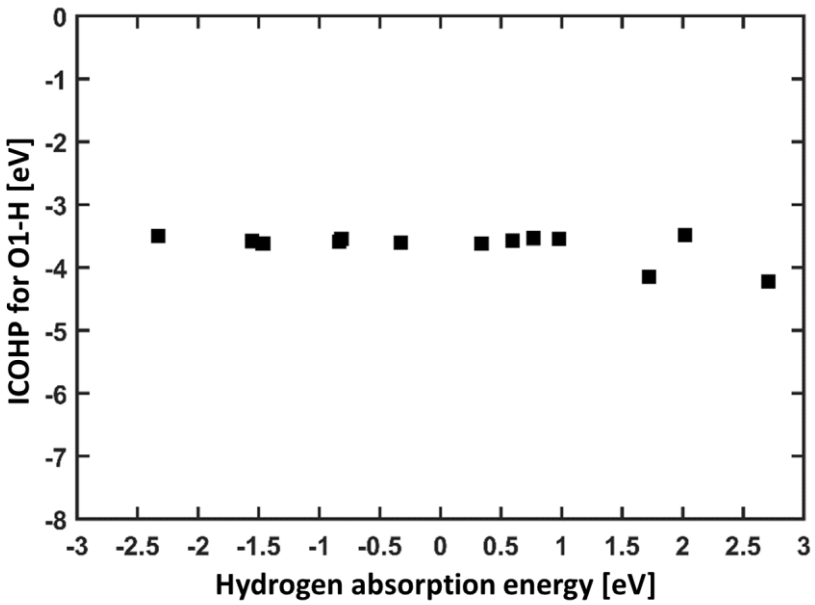

Figure 3.S3 Scatterplot of O1-H ICOHP versus hydrogen absorption energy (HAE). See Figure 3.2 for labels of the O atom.

3.S4 Abbreviations

(I/p)COHP	(Integral/projected) Crystal orbital hamilton population
OVFE	Oxygen vacancy formation energy
HAE	Hydrogen absorption energy
DFT	Density functional theory
DOS	Density-of-states
TS	Transition-state
CI-NEB	Climbing-image Nudged-elastic band

3.S5 Formulas

Num.	Formula
3.1	$E_{HAE} = E_{Bulk+H} - E_{Bulk} - \frac{1}{2}E_{H_2}$
3.2	$E_{OVFE} = E_{Bulk-O} + \frac{1}{2}E_{O_2} - E_{Bulk}$
3.3	$\Delta X_{B-A} = X_B - X_A$

References

(1) Norby, T.; Widerøe, M.; Glöckner, R.; Larring, Y. Hydrogen in Oxides. *Dalton Trans.* **2004**, No. 19, 3012–3018. https://doi.org/10.1039/B403011G.

(2) Kreuer, K.-D. Proton Conductivity: Materials and Applications. *Chem. Mater.* **1996**, *8* (3), 610–641. https://doi.org/10.1021/cm950192a.

(3) Thomas, D. G.; Lander, J. J. Hydrogen as a Donor in Zinc Oxide. *J. Chem. Phys.* **1956**, *25* (6), 1136–1142. https://doi.org/10.1063/1.1743165.

(4) Iwahara, H. Proton Conducting Ceramics and Their Applications. *Solid State Ionics* **1996**, *86–88*, 9–15. https://doi.org/10.1016/0167-2738(96)00087-2.

(5) Kochetova, N.; Animitsa, I.; Medvedev, D.; Demin, A.; Tsiakaras, P. Recent Activity in the Development of Proton-Conducting Oxides for High-Temperature Applications. *RSC Adv.* **2016**, *6* (77), 73222–73268. https://doi.org/10.1039/C6RA13347A.

(6) Kim, J.; Sengodan, S.; Kim, S.; Kwon, O.; Bu, Y.; Kim, G. Proton Conducting Oxides: A Review of Materials and Applications for Renewable Energy Conversion and Storage. *Renewable and Sustainable Energy Reviews* **2019**, *109*, 606–618. https://doi.org/10.1016/j.rser.2019.04.042.

(7) Takahashi, T.; Iwahara, H. ChemInform Abstract: Solid-state Ionics: Protonic Conduction in Perovskite Type Oxide Solid Solutions. *Chemischer Informationsdienst* **1981**, *12* (14). https://doi.org/10.1002/chin.198114014.

(8) Iwahara, H.; Uchida, H.; Ono, K.; Ogaki, K. Proton Conduction in Sintered Oxides Based on $BaCeO_3$. *J. Electrochem. Soc.* **1988**, *135* (2), 529. https://doi.org/10.1149/1.2095649.

(9) Iwahara, H.; Esaka, T.; Uchida, H.; Maeda, N. Proton Conduction in Sintered Oxides and Its Application to Steam Electrolysis for Hydrogen Production. *Solid State Ionics* **1981**, *3–4*, 359–363. https://doi.org/10.1016/0167-2738(81)90113-2.

(10) Mitsui, A.; Miyayama, M.; Yanagida, H. Evaluation of the Activation Energy for Proton Conduction in Perovskite-Type Oxides. *Solid State Ionics* **1987**, *22* (2), 213–217. https://doi.org/10.1016/0167-2738(87)90035-X.

(11) Bjørheim, T. S.; Kuwabara, A.; Ahmed, I.; Haugsrud, R.; Stølen, S.; Norby, T. A Combined Conductivity and DFT Study of Protons in $PbZrO_3$ and Alkaline Earth Zirconate Perovskites. *Solid State Ionics* **2010**, *181* (3), 130–137. https://doi.org/10.1016/j.ssi.2009.04.013.

(12) Bork, N.; Bonanos, N.; Rossmeisl, J.; Vegge, T. Simple Descriptors for Proton-Conducting Perovskites from Density Functional Theory. *Phys. Rev. B* **2010**, *82* (1), 014103. https://doi.org/10.1103/PhysRevB.82.014103.

(13) Wohlfahrt-Mehrens, M.; Schenk, J.; Wilde, P. M.; Abdelmula, E.; Axmann, P.; Garche, J. New Materials for Supercapacitors. *Journal of power sources* **2002**, *105* (2), 182–188.

(14) Kresse, G.; Furthmüller, J. Efficiency of *Ab-Initio* Total Energy Calculations for Metals and Semiconductors Using a Plane-Wave Basis Set. *Computational Materials Science* **1996**, *6* (1), 15–50. https://doi.org/10.1016/0927-0256(96)00008-0.

(15) Kresse, G.; Furthmüller, J. Efficient Iterative Schemes for *Ab Initio* Total-Energy Calculations Using a Plane-Wave Basis Set. *Phys. Rev. B* **1996**, *54* (16), 11169–11186. https://doi.org/10.1103/PhysRevB.54.11169.

(16) Blöchl, P. E. Projector Augmented-Wave Method. *Phys. Rev. B* **1994**, *50* (24), 17953–17979. https://doi.org/10.1103/PhysRevB.50.17953.

(17) Kresse, G.; Joubert, D. From Ultrasoft Pseudopotentials to the Projector Augmented-Wave Method. *Phys. Rev. B* **1999**, *59* (3), 1758–1775. https://doi.org/10.1103/PhysRevB.59.1758.

(18) Perdew, J. P.; Burke, K.; Ernzerhof, M. Generalized Gradient Approximation Made Simple. *Phys. Rev. Lett.* **1996**, *77* (18), 3865–3868. https://doi.org/10.1103/PhysRevLett.77.3865.

(19) Monkhorst, H. J.; Pack, J. D. Special Points for Brillouin-Zone Integrations. *Phys. Rev. B* **1976**, *13* (12), 5188–5192. https://doi.org/10.1103/PhysRevB.13.5188.

(20) Jain, A.; Ong, S. P.; Hautier, G.; Chen, W.; Richards, W. D.; Dacek, S.; Cholia, S.; Gunter, D.; Skinner, D.; Ceder, G.; Persson, K. A. Commentary: The Materials

Project: A Materials Genome Approach to Accelerating Materials Innovation. *APL Materials* **2013**, *1* (1), 011002. https://doi.org/10.1063/1.4812323.

(21) Jiang, L. Q.; Guo, J. K.; Liu, H. B.; Zhu, M.; Zhou, X.; Wu, P.; Li, C. H. Prediction of Lattice Constant in Cubic Perovskites. *Journal of Physics and Chemistry of Solids* **2006**, *67* (7), 1531–1536. https://doi.org/10.1016/j.jpcs.2006.02.004.

(22) Moreira, R. L.; Dias, A. Comment on "Prediction of Lattice Constant in Cubic Perovskites." *Journal of Physics and Chemistry of Solids* **2007**, *68* (8), 1617–1622. https://doi.org/10.1016/j.jpcs.2007.03.050.

(23) Deringer, V. L.; Tchougréeff, A. L.; Dronskowski, R. Crystal Orbital Hamilton Population (COHP) Analysis As Projected from Plane-Wave Basis Sets. *J. Phys. Chem. A* **2011**, *115* (21), 5461–5466. https://doi.org/10.1021/jp202489s.

(24) Dronskowski, R.; Bloechl, P. E. Crystal Orbital Hamilton Populations (COHP): Energy-Resolved Visualization of Chemical Bonding in Solids Based on Density-Functional Calculations. *J. Phys. Chem.* **1993**, *97* (33), 8617–8624. https://doi.org/10.1021/j100135a014.

(25) Maintz, S.; Deringer, V. L.; Tchougréeff, A. L.; Dronskowski, R. LOBSTER: A Tool to Extract Chemical Bonding from Plane-Wave Based DFT. *Journal of Computational Chemistry* **2016**, *37* (11), 1030–1035. https://doi.org/10.1002/jcc.24300.

(26) Allred, A. L.; Rochow, E. G. A Scale of Electronegativity Based on Electrostatic Force. *Journal of Inorganic and Nuclear Chemistry* **1958**, *5* (4), 264–268. https://doi.org/10.1016/0022-1902(58)80003-2.

(27) Housecroft, C. E.; Sharpe, A. G. *Inorganic Chemistry*; Pearson Prentice Hall, 2005.

(28) Henkelman, G.; Uberuaga, B. P.; Jónsson, H. A Climbing Image Nudged Elastic Band Method for Finding Saddle Points and Minimum Energy Paths. *The Journal of chemical physics* **2000**, *113* (22), 9901–9904.

(29) Björketun, M. E.; Sundell, P. G.; Wahnström, G. Effect of Acceptor Dopants on the Proton Mobility in $BaZrO_3$: A Density Functional Investigation. *Phys. Rev. B* **2007**, *76* (5), 054307. https://doi.org/10.1103/PhysRevB.76.054307.

(30) van Duin, A. C. T.; Merinov, B. V.; Han, S. S.; Dorso, C. O.; Goddard, W. A. ReaxFF Reactive Force Field for the Y-Doped $BaZrO_3$ Proton Conductor with Applications to Diffusion Rates for Multigranular Systems. *J. Phys. Chem. A* **2008**, *112* (45), 11414–11422. https://doi.org/10.1021/jp801082q.

(31) Fronzi, M.; Tateyama, Y.; Marzari, N.; Nolan, M.; Traversa, E. First-Principles Molecular Dynamics Simulations of Proton Diffusion in Cubic $BaZrO_3$ perovskite under Strain Conditions. *Mater Renew Sustain Energy* **2016**, *5* (4), 14. https://doi.org/10.1007/s40243-016-0078-9.

(32) Islam, M. S.; Davies, R. A.; Gale, J. D. Proton Migration and Defect Interactions in the $CaZrO_3$ Orthorhombic Perovskite: A Quantum Mechanical Study. *Chem. Mater.* **2001**, *13* (6), 2049–2055. https://doi.org/10.1021/cm010005a.

(33) Hoffmann, R. *Solids and Surfaces: A Chemist's View of Bonding in Extended Structures*; VCH Publishers, 1988.

(34) van Santen, R. A.; Tranca, I.; Hensen, E. J. M. Theory of Surface Chemistry and Reactivity of Reducible Oxides. *Catalysis Today* **2015**, *244*, 63–84. https://doi.org/10.1016/j.cattod.2014.07.009.

(35) Fung, V.; Wu, Z.; Jiang, D. New Bonding Model of Radical Adsorbate on Lattice Oxygen of Perovskites. *J. Phys. Chem. Lett.* **2018**, *9* (21), 6321–6325. https://doi.org/10.1021/acs.jpclett.8b02749.

(36) Fung, V.; Polo-Garzon, F.; Wu, Z.; Jiang, D. Exploring Perovskites for Methane Activation from First Principles. *Catal. Sci. Technol.* **2018**, *8* (3), 702–709. https://doi.org/10.1039/C7CY01791J.

(37) Fung, V.; Tao, F. F.; Jiang, D. General Structure–Reactivity Relationship for Oxygen on Transition-Metal Oxides. *J. Phys. Chem. Lett.* **2017**, *8* (10), 2206–2211. https://doi.org/10.1021/acs.jpclett.7b00861.

(38) Fung, V.; Tao, F. (Feng); Jiang, D. Trends of Alkane Activation on Doped Cobalt (II, III) Oxide from First Principles. *ChemCatChem* **2018**, *10* (1), 244–249. https://doi.org/10.1002/cctc.201700960.

(39) Latimer, A. A.; Kulkarni, A. R.; Aljama, H.; Montoya, J. H.; Yoo, J. S.; Tsai, C.; Abild-Pedersen, F.; Studt, F.; Nørskov, J. K. Understanding Trends in C–H Bond Activation in Heterogeneous Catalysis. *Nature Materials* **2017**, *16* (2), 225–229. https://doi.org/10.1038/nmat4760.

(40) Münch, W.; Kreuer, K. D.; Adams, S.; Seifert, G.; Maier, J. The Relation between Crystal Structure and the Formation and Mobility of Protonic Charge Carriers in Perovskite-Type Oxides: A Case Study of Y-Doped $BaCeO_3$ and $SrCeO_3$. *Phase Transitions* **1999**, *68* (3), 567–586. https://doi.org/10.1080/01411599908224535.

(41) Ishihara, T. *Perovskite Oxide for Solid Oxide Fuel Cells*; Springer Science & Business Media, 2009.

Chapter 4

First Principles Insights into the Heterostructures of MXene and TiO_2

4.1 Abstract

Heterostructures of MXenes (2D carbides and nitrides) and transition-metal oxides (TMOs) have shown great promises in electrical energy storage. However, many fundamental properties at the interfaces of MXenes and TMOs are still unclear. Here we use first-principles density functional theory (DFT) to investigate the interfacial structure, energetics, and electronic properties of the heterostructures of TiC-based MXenes and anatase TiO_2. For the heterostructures containing MXene with -O terminations, the density

of states (DOS) shows that the system switches from a semiconductor to metal after increasing the thickness of MXene (from Ti_2CO_2 to $Ti_3C_2O_2$). For MXene with –OH terminations, the strong H-bonding interactions at interface contribute to strong adhesive energy.

4.2 Introduction

In recent years, extensive efforts have been devoted to enhancing the performance of energy storage devices. However, it is still a challenge to achieve both high energy density and power density, simultaneously.[1–4] Novel electrode materials hold the key to a breakthrough in performances.

Due to the excellent electrical conductivity and high volumetric capacitance, MXenes (2D carbides and nitrides) were explored in applications for electrical energy storage and electrocatalysis.[5–14] Especially, many researchers have demonstrated great potentials of using MXenes for capacitive energy storage.[15–20] To further enhance the capacitor performance, MXene nanosheets such as $Ti_3C_2T_x$ (T denotes terminal groups such as -O, -OH, and -F) were hybridized with transition metal oxides (TMOs),[21,22] and the resultant binder-free flexible films exhibited excellent Li-ion storage capability. For example, Rakhi et al. reported that nanocrystalline ε-MnO_2 coated MXene nanosheets (ε-MnO_2/$Ti_2CT_x$and ε-MnO_2/$Ti_3C_2T_x$) showed superior specific capacitance when compared with pure MXene-based symmetric supercapacitors.[23] In another report, Ahmed et al. successfully fabricated TiO_2 nanocrystals on the surface of Ti_2CT_x MXene sheets for Li-ion battery applications.[24]

Despite many experimental demonstrations of using MXene/TMO composite/hybrid materials as the electrodes for energy storage, fundamental understanding of the interfacial structure, energetics, and electronic properties is still missing. $Ti_3C_2T_x$ is the most studied MXene and metallic, but its cousin Ti_2CT_x offers higher specific capacitance (due to smaller formula weight) despite its semiconducting nature.[25,26] Thus, it will be interesting to examine the contrast between Ti_2CT_x and $Ti_3C_2T_x$ in forming interfaces with TMOs. In addition, heterostructures of the 2D metal/semiconductor are held together mainly through the van der Waals (vDW) interactions, resulting in weak Fermi-level pining that enables the effective tuning of the Schottky barrier.[27–29]

To address the issues raised above, herein, we investigate the interfacial properties of Ti_2CT_x/TiO_2 and $Ti_3C_2T_x/TiO_2$ heterostructures using the first-principles density-functional theory (DFT), as an initial step toward understanding the MXene/TMO interfaces and heterostructures. We chose $Ti_3C_2T_x$ because it is the most studied MXene so far,[17,30] Ti_2CT_x for comparison with $Ti_3C_2T_x$, and TiO_2 as it is the most studied TMO.[31] Here we focus on the anatase phase since it is more widely used in many applications and has a remarkably higher specific surface area.[32,33] Regarding surface chemistry, we consider three different surface functional groups on the Ti_2CT_x and $Ti_3C_2T_x$ MXenes (T= 100% -O, 100% -OH, a mixture of 10% -F and 90% -O). Below we first elaborate our computational approach.

4.3 Computational methods

Density functional theory (DFT) calculations were performed using the plane-wave pseudopotential method as implemented in the Vienna *ab initio* simulation package (VASP).[34,35] The electron-ion interactions were described by the projector augmented-wave (PAW) methods[36,37] while the electron exchange-correlation part was parameterized by the Perdew-Burke-Ernzerhof[38] (PBE) functional form of generalized gradient approximation (GGA). The kinetic energy cutoff of 500 eV was used for the plane-wave basis set. Periodic boundary conditions have been utilized in all calculations with the Grimme DFT-D3 dispersion correction (Becke-Jonson damping[39]) to account for the van der Waals (vDW) interactions.[40,41]

The optimized lattice constants of tetragonal anatase TiO_2 unit cell are **a** = **b** = 3.827 Å and **c** = 9.665 Å, while the calculated in-plane lattice constants for MXene are 3.043, 3.092, 3.057, 3.105 Å for Ti_2CO_2, $Ti_2C(OH)_2$, $Ti_3C_2O_2$ and $Ti_3C_2(OH)_2$, respectively. Because of either LiF+HCl or HF was used in preparing MXene,[42–44] its surface is usually ended up with a fraction of -F functional groups, so we also considered this scenario by substituting 10% of the –O surface-terminations with -F, namely, having $Ti_2CF_{0.2}O_{1.8}$ and $Ti_3C_2F_{0.2}O_{1.8}$ as building blocks as well.

The heterostructure comprises a lateral supercell of the anatase TiO_2 (101) surface (the most stable one) matched to a similar lateral supercell of the MXene basal plane: Table 4.1 shows the cases whose lattice mismatches are smaller than 2.5%. These two-dimensional slabs, containing an MXene monolayer and three TiO_2 anatase (101) surface layers, were modeled by using supercell approximation with a vacuum space about 15 Å

along the z-axis. Only MXene and the top TiO_2 layers were allowed to relax during structure optimizations. Convergence criteria were set to be 0.02 eV/Å for force and 10^{-5} eV energy and the Brillouin zone was sampled by (3×3×1) Monkhorst-Pack grid.[45]

The adhesive energy (E_{inter}) of the interface between MXene and TiO_2 layers is defined as:

$$E_{inter} = (E_{MXene} + E_{TiO_2} - E_{total})/A \quad (4.1)$$

where E_{MXene}, E_{TiO_2}, and E_{total} represent the energies of the MXene layer, the TiO_2 layer, and the heterostructure, respectively; A is the area of the interface.

Table 4.1 Lattice mismatches for several heterostructure systems.

System	a Lattice [Å]	b Lattice [Å]	γ Degrees [°]	Mismatch
Ti_2CO_2/TiO_2	15.651	11.227	43.029	1.8%
$Ti_2CF_{0.2}O_{1.8}/TiO_2$	15.651	11.227	43.029	1.8%
$Ti_2C(OH)_2/TiO_2$	15.777	11.314	43.029	2.0%
$Ti_3C_2O_2/TiO_2$	15.686	11.252	43.029	1.7%
$Ti_3C_2F_{0.2}O_{1.8}/TiO_2$	15.686	11.252	43.029	1.7%
$Ti_3C_2(OH)_2/TiO_2$	15.811	11.338	43.029	2.4%

4.4 Results and discussion

Before elaborating on the interfacial energetic and electronic properties of the different heterostructures, we first compare the work functions and electronic density of states of the building blocks.

4.4.1 Building blocks for the heterostructures

Table 4.2 shows the calculated work functions for all building blocks. It is found that the work functions of MXenes are all lower than that of the anatase TiO_2 (101) surface [a-TiO_2 (101)]. As expected, -OH termination leads to the lowest work function,[46] while including a fraction of -F groups on the surface lowers the work function of the -O termination. Moreover, there is a small change in the work function from Ti_2CT_x to $Ti_3C_2T_x$.

Table 4.2 Calculated work function (in eV) of the building blocks.

System	Work Function	System	Work Function
Ti_2CO_2	5.70	$Ti_3C_2O_2$	5.94
$Ti_2CF_{0.2}O_{1.8}$	5.67	$Ti_3C_2F_{0.2}O_{1.8}$	5.04
$Ti_2C(OH)_2$	1.63	$Ti_3C_2(OH)_2$	1.57
a-TiO_2(101)	6.43		

Figure 4.1 compares the total DOS of the building blocks. Ti_2CO_2 has a small band gap, while $Ti_3C_2O_2$ is metallic (Figure 1a). In addition, by substituting 10% of the -O terminations with the –F terminated groups in Ti_2CO_2, the resulting $Ti_2CF_{0.2}O_{1.8}$ also becomes metallic (Figure 1b). In comparison, both $Ti_2C(OH)_2$ and $Ti_3C_2(OH)_2$ (Figure 1c), TiO_2 is a semiconductor (Figure 1d). The electronic properties of the building blocks provide a basis for our discussion of the heterostructures as in the following.

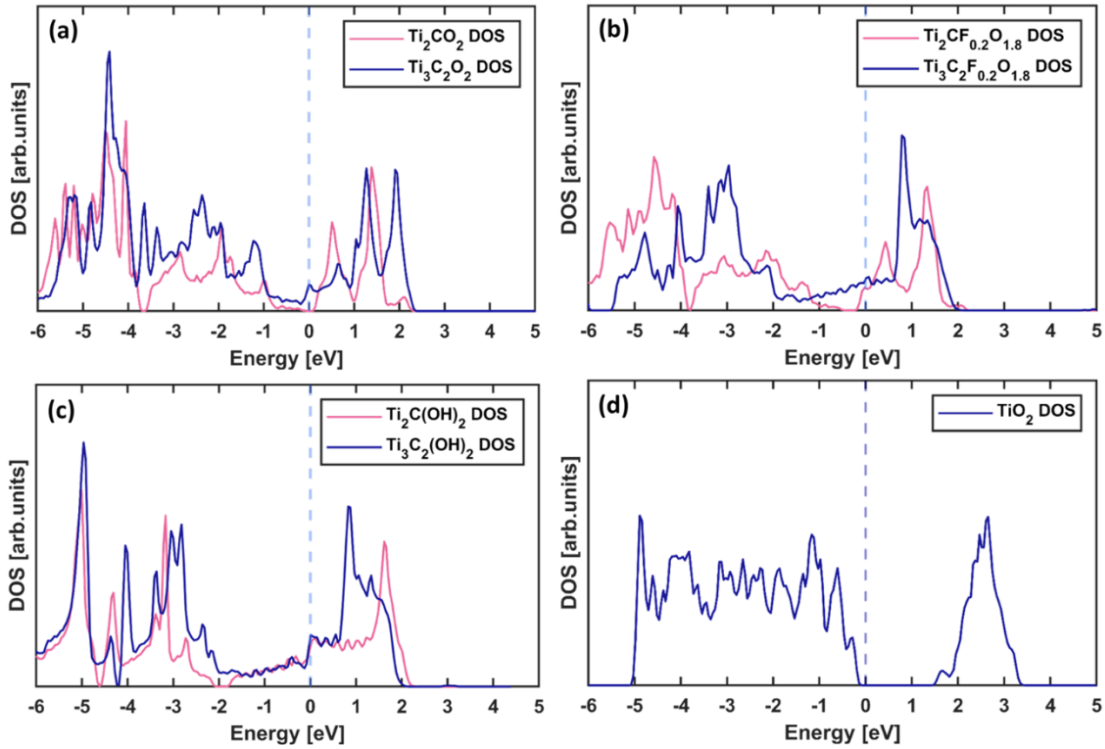

Figure 4.1 Total density of state (DOS) **(a)** Ti_2CO_2 and $Ti_3C_2O_2$; **(b)** $Ti_2CF_{0.2}O_{1.8}$ and $Ti_3C_2F_{0.2}O_{1.8}$; **(c)** $Ti_2C(OH)_2$ and $Ti_3C_2(OH)_2$; **(d)** anatase-TiO_2.

4.4.2 Structure and energetics of the heterostructures

Figure 4.2 shows the optimal configurations for all heterostructures under investigation and their plane-averaged interlayer distances between the surface-O layer from a-TiO_2(101) and the O-layer from MXene (namely, the distance between the two closest O-layers at the interface). In general, the thickness of the MXene does not impact the plane-averaged interlayer distance too much. By modifying the surface functional groups, the interlayer distance decreases slightly around 0.03Å from MXene (100% -O)/TiO_2 to MXene (10% -F and 90% -O)/TiO_2. The interlayer distance for MXene (100% -OH)/TiO_2 is almost unchanged regardless of the multiple H-bonding within interfaces.

The H-bonding induces higher interfacial adhesion energy (E_{inter}) >5 eV/nm^2, which is over 5 times larger than that of MXene(100% -O)/TiO_2 (Table 4.3). In addition, due to rigid stacking layers, -OH groups can H-bond with more than one surface-O from a-TiO_2(101), thereby contributing more to the stronger interfacial interactions. With -F functional groups substituting -O in MXene, E_{inter} decreased about 0.1 eV/nm^2 from MXene (100% -O)/TiO_2 to MXene(10% -F and 90% -O)/TiO_2, indicating a weaker interfacial interaction. Moreover, changing MXene thickness from Ti_2CO_2 to $Ti_3C_2O_2$ will affect E_{inter} by about 0.2 eV/nm^2.

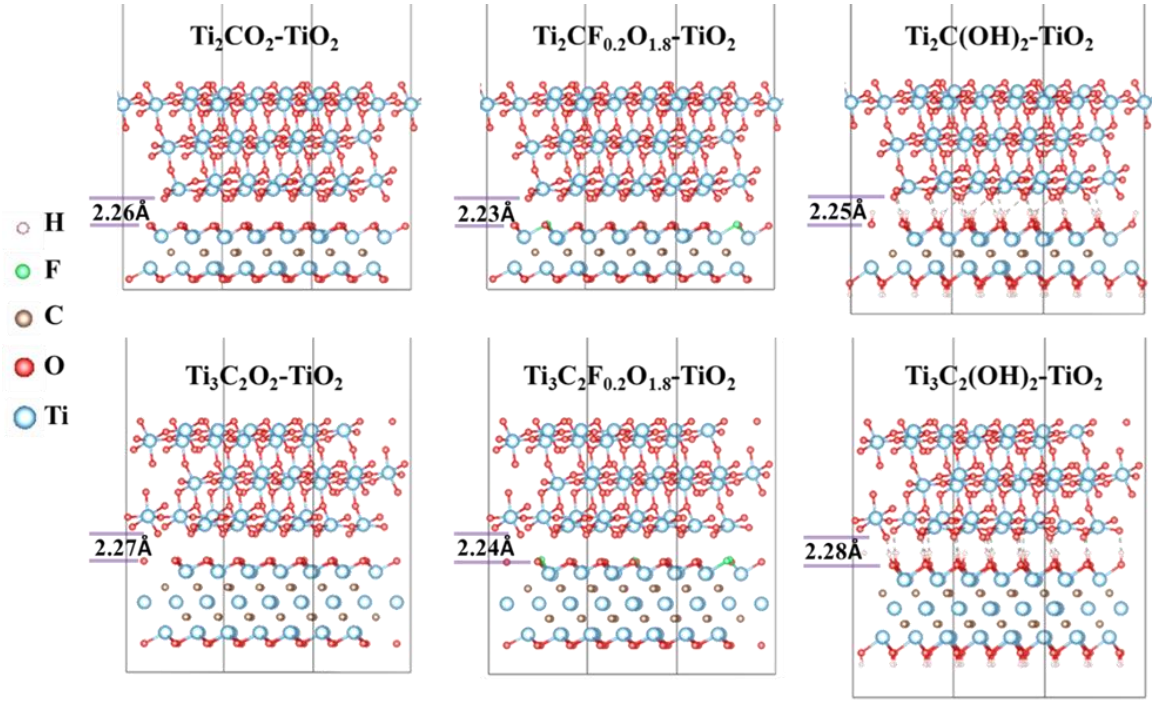

Figure 4.2 Optimal geometries of different heterostructures. The plane-averaged interlayer distance (shown as the number between two solid purple lines) is determined as the distance between the surface-O layer from a-TiO_2(101) and the O-layer from MXene monolayer.

Table 4.3 Interfacial adhesion energy (E_{inter}) for different MXene/TiO_2 systems.

Structure	E_{inter} [eV/nm^2]
Ti_2CO_2/TiO_2	1.00
$Ti_2CF_{0.2}O_{1.8}/TiO_2$	0.93
$Ti_2C(OH)_2/TiO_2$	5.31
$Ti_3C_2O_2/TiO_2$	0.82
$Ti_3C_2F_{0.2}O_{1.8}/TiO_2$	0.71
$Ti_3C_2(OH)_2/TiO_2$	5.11

4.4.3 Electronic properties of the heterostructures

Figure 4.3 depicts the electron-density differences for all heterostructures, the arrows and values dictate the electron transfer direction and amount across the interfaces, respectively. Around 0.015 e/nm^2 were transferred from MXene (100% -O) to TiO_2, a lightly higher value 0.020 e/nm^2 were obtained from MXene (10% -O and 90% -F) to TiO_2. Over 0.85 e/nm^2 goes to the TiO_2 from MXene (100% -OH). Hence, via varying the surface functional groups of MXene, the relevant interfacial electrostatic polarization differs, leading to a huge difference in the interfacial electronic properties. These results are in line with our group's previous findings: the larger the work function difference between interfacial building blocks, the more electrons will be transferred from the building block with the lower work function value to the one with a higher value.[47] For better understanding the electron distributions within interfaces, the plane-averaged electron density differences were plotted in Figure 4.4. Most of the transferred electrons accumulated at the surface-O and -Ti layers from the a-TiO_2, and the electron distributions are mainly localized in the regions nearby two interfacial areas of heterostructures.

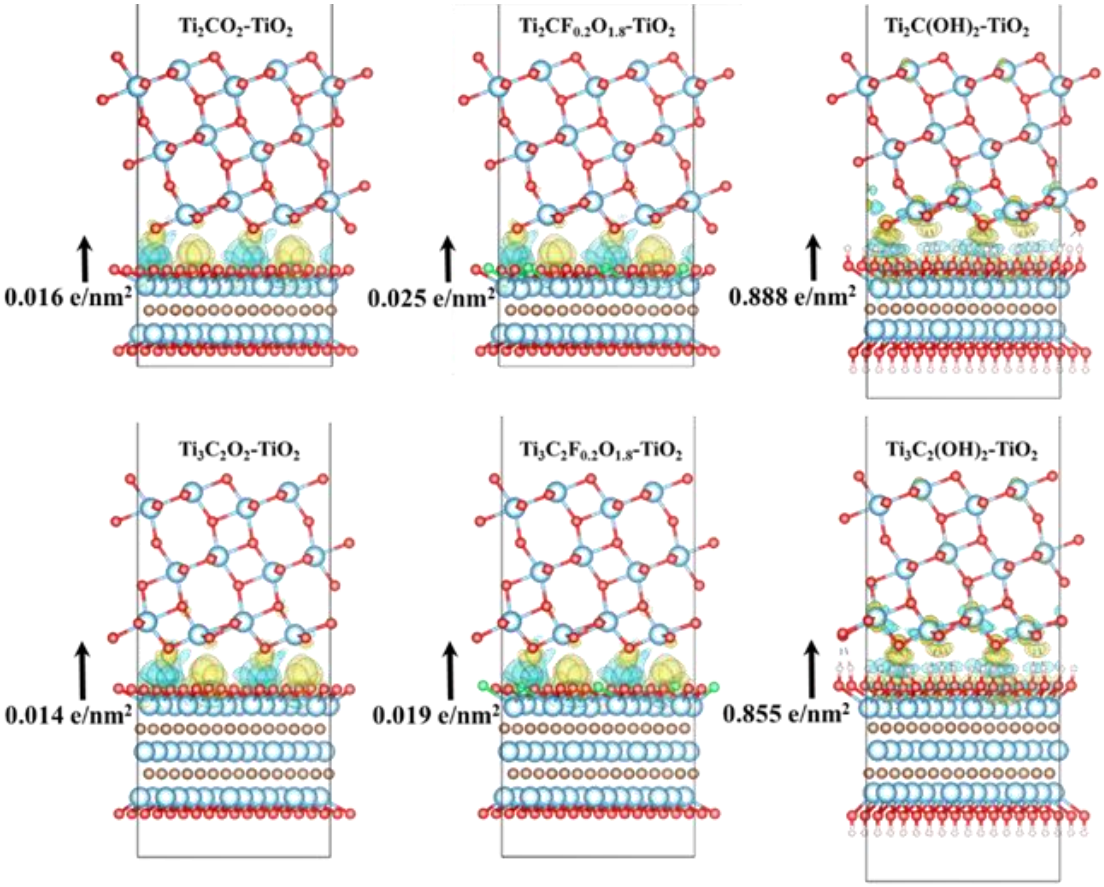

Figure 4.3 The electron-density difference for different heterostructures. The arrow and number illustrate the electron transfer direction and amount, respectively. The excess (yellow) and depleted (cyan) electrons are shown in the plots. The iso-surface value is 0.003 e/Å^3 for MXene(100% -OH)/TiO_2 and 0.0006 e/Å^3 for all other heterostructures.

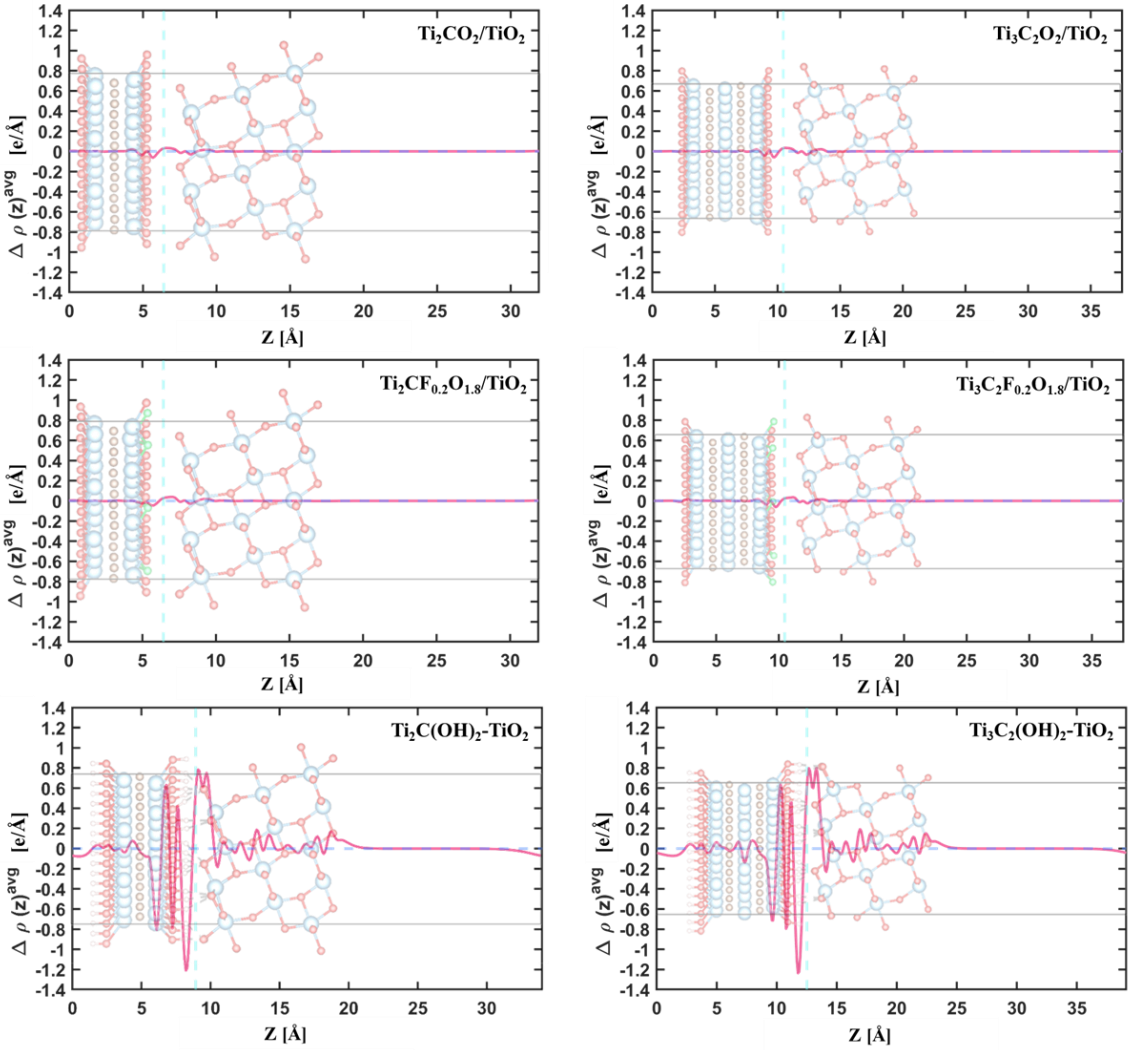

Figure 4.4 The plane-averaged electron-density difference for different heterostructures. The dashed light-blue line represents the middle position between the interlayer spaces (the two closest O-layer within the interfaces).

To elaborate the conductivity for different heterostructures, we plot the density of states (DOS) and PDOS for different building blocks as shown in Figure 4.5. The Fermi-level is set to zero in energy. The Ti_2CO_2/TiO_2 heterostructure is semiconducting, while $Ti_3C_2O_2/TiO_2$ is metallic. For all other heterostructures, the high DOS values at Fermi-level were contributed by the MXene monolayer. When the surface functionalization of the

MXene changes from 100% –O to a mixture of 10% –F and 90% -O, the DOS plots shift downward as more electrons are localized on the F atoms. Furthermore, $Ti_2CF_{0.2}O_{1.8}/TiO_2$ heterostructure becomes a conductor.

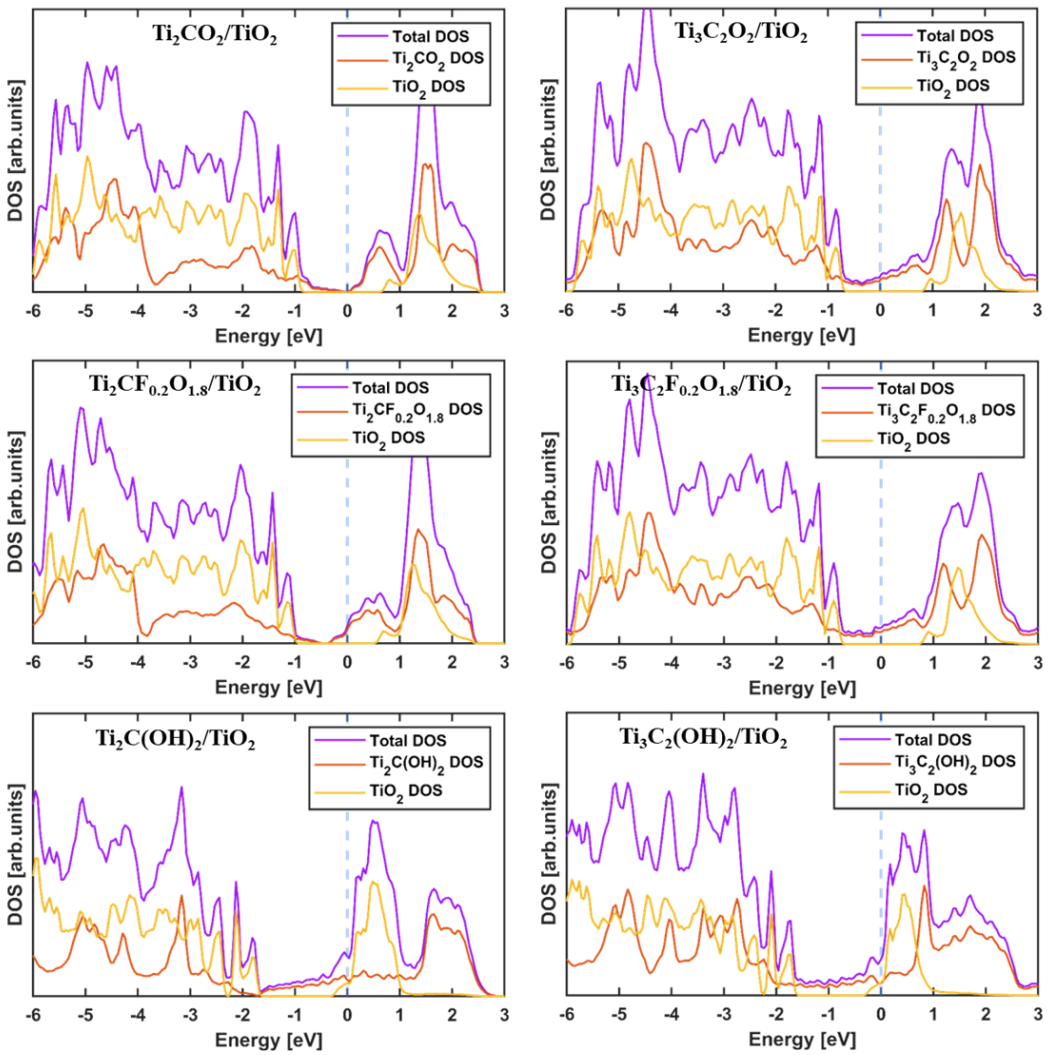

Figure 4.5 The density of state (DOS) and projected-DOS (pDOS) for different heterostructures. The Fermi-level is set to zero in energy.

4.5 Conclusion

We have carried out a comprehensive first-principles study of the structural, energetic, and electronic properties within the interfaces of different MXene/a-TiO_2(101) heterostructures. Different thicknesses of MXene (Ti_2CT_2 and $Ti_3C_2T_2$) and surface functional groups (100% -O, 100% -OH, or a mixture of 10% -F and 90% -O terminations) are examined in our studies. We found that the most considerable work function difference of the individual building blocks occurs in MXene (100% -OH)/TiO_2 heterostructures, leading to the largest electrons transfer from MXene (100% -OH) to TiO_2 layer. For Ti_2CO_2-based heterostructures, through modifying the surface functional groups ($Ti_2CF_{0.2}O_{1.8}$), the heterostructure will change from a semiconductor to a conductor. In addition, the presence of the multiple interfacial H-bonding in MXene (100% -OH)/TiO_2 make the interfacial adhesion energy (E_{inter}) >5 eV/nm^2. To sum up, our simulation results provide fundamental understandings of various interfacial properties for different MXene/TiO_2 heterostructures.

4.6 MXene(-O, -OH)/(N)TiO_2 heterostructures

Besides modifying surface functional groups of MXene,[48] the chemical manipulation method, element doping, is another way to modify the interfacial properties.[49] Following, we use the DFT approach to explore some interfacial properties in MXene/(N)TiO_2 heterostructures. This study serves as an attempt, only the MXenes (Ti_2CT_2 and $Ti_3C_2T_2$) with pure surface terminational groups (T=100% -O, or 100% -OH)

are involved. Since we mainly focused on interfaces, we start by using the N element to dope only one surface-O from a-TiO_2(101).

The optimal heterostructures and the electron-density difference were depicted in Figure 4.6. It suggests that the electrons are more localized surrounding the doped N atom. The DOS plots (Figure 4.7) present that after doping, the Ti_2CO_2/(1N)TiO_2 becomes a conductor. Meanwhile, the calculated work function values are 6.43 eV for the TiO_2 and 6.75 for the (1N)TiO_2 in our case. The analysis of the amount of interfacial electron transfer and the interfacial adhesion energy is warranted in our future work.

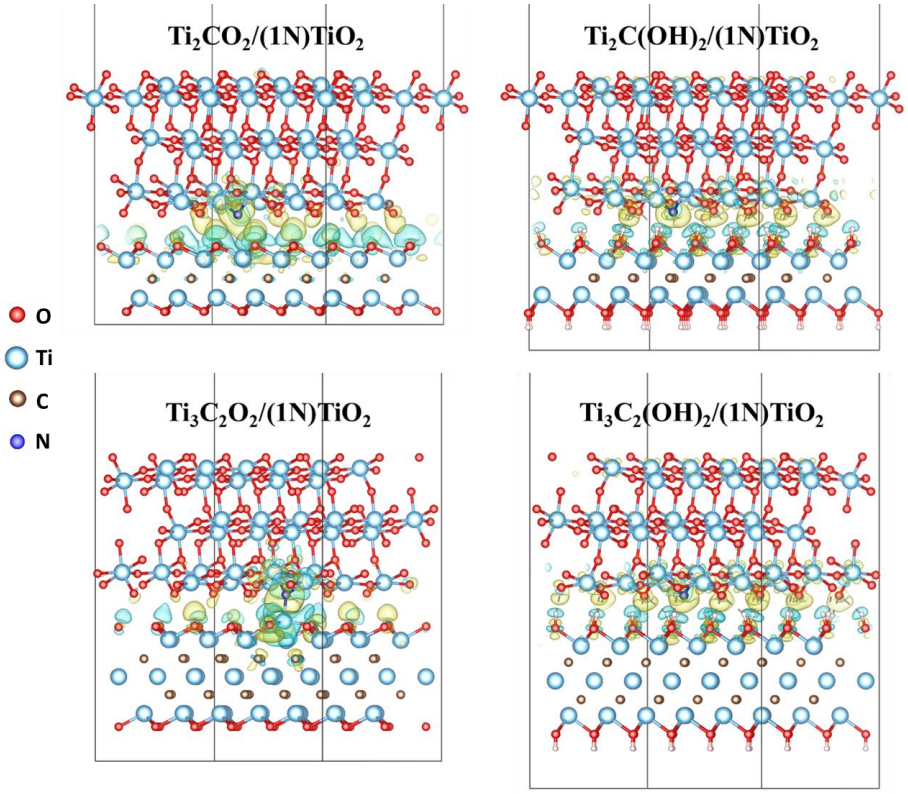

Figure 4.6 The electron-density difference for different optimal heterostructures. The excess (yellow) and depleted (cyan) electrons are shown in the plots. The iso-surface value is 0.003 e/Å^3 for MXene(100% -OH)/(1N)TiO_2, 0.0006 e/Å^3 for Ti_2CO_2/(1N)TiO_2, and 0.001 e/Å^3 for $Ti_3C_2O_2$/(1N)TiO_2.

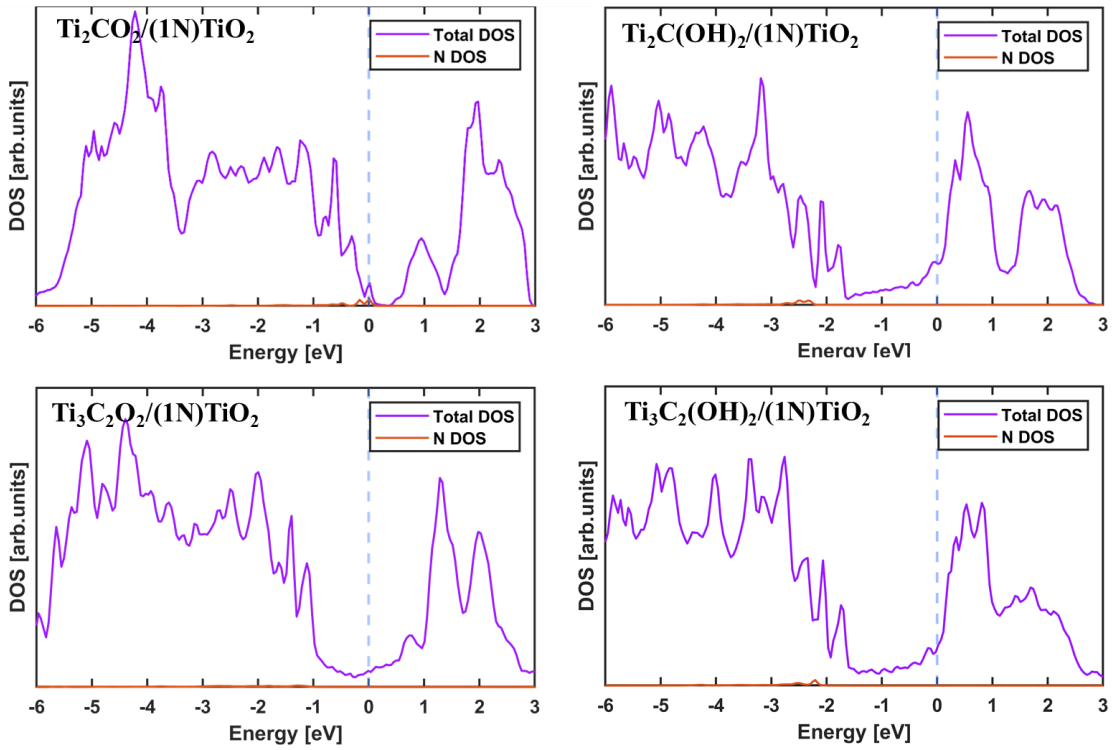

Figure 4.7 The total density of state (DOS) and projected-DOS of the N element for different heterostructures. The Fermi-level is set to zero in energy.

Moreover, in $Ti_3C_2O_2$/(1N)TiO_2 heterostructure, we noticed the formation of the bond between the doped N and the closest Ti from $Ti_3C_2O_2$ (Figure 4.6). We further explore the cases with additional doped N in TiO_2 for MXene(100% -O)/(N)-TiO_2 heterostructures. Interestingly, we also observe the formation of these N-Ti bonds (Figure 4.8). The corresponding bonding analysis and interfacial properties will be our future research directions.

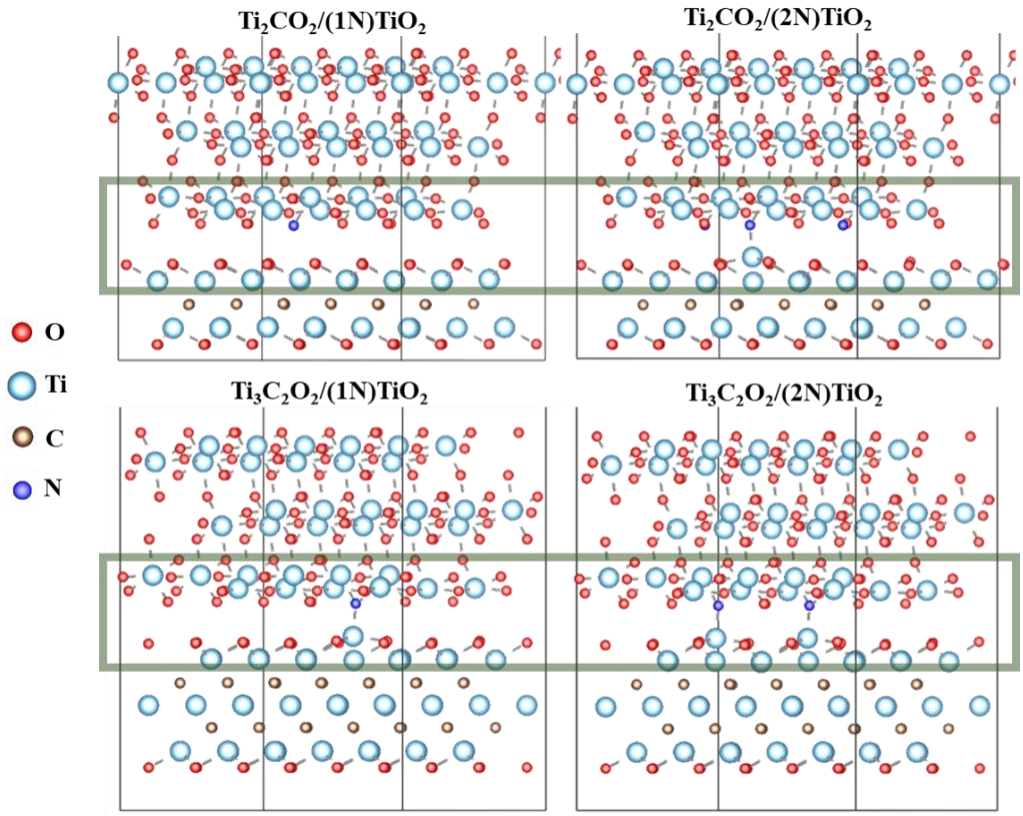

Figure 4.8 Optimal geometries of different MXene/(N)TiO_2 heterostructures. There is only 1N doping TiO_2 in the left column of the plot, while 2N doping in the right column of the plot.

Supporting information

4.S1 Abbreviations

TMO	Transition metal oxide
DFT	Density functional theory
(p)DOS	(projected) Density-of-states
vDW	van der Waals

4.S2 Formulas

Num.	Formula
4.1	$E_{inter} = (E_{MXene} + E_{TiO_2} - E_{total})/A$

References

(1) Pomerantseva, E.; Gogotsi, Y. Two-Dimensional Heterostructures for Energy Storage. *Nature Energy* **2017**, *2* (7), 1–6. https://doi.org/10.1038/nenergy.2017.89.

(2) Choi, C.; Ashby, D. S.; Butts, D. M.; DeBlock, R. H.; Wei, Q.; Lau, J.; Dunn, B. Achieving High Energy Density and High Power Density with Pseudocapacitive Materials. *Nature Reviews Materials* **2020**, *5* (1), 5–19. https://doi.org/10.1038/s41578-019-0142-z.

(3) Li, J.; Du, Z.; Ruther, R. E.; An, S. J.; David, L. A.; Hays, K.; Wood, M.; Phillip, N. D.; Sheng, Y.; Mao, C. Toward Low-Cost, High-Energy Density, and High-Power Density Lithium-Ion Batteries. *Jom* **2017**, *69* (9), 1484–1496. https://doi.org/10.1007/s11837-017-2404-9.

(4) Sajjad, M.; Chen, X.; Yu, C.; Guan, L.; Zhang, S.; Ren, Y.; Zhou, X.; Liu, Z. High Energy Density Asymmetric Supercapacitor Based on $NiCo_2S_4$/CNTs Hybrid and Carbon Nanotube Paper Electrodes. *J. Mol. Eng. Mater.* **2019**, *07* (01n02), 1950004. https://doi.org/10.1142/S2251237319500047.

(5) Naguib, M.; Mochalin, V. N.; Barsoum, M. W.; Gogotsi, Y. 25th Anniversary Article: MXenes: A New Family of Two-dimensional Materials. *Advanced materials* **2014**, *26* (7), 992–1005. https://doi.org/10.1002/adma.201304138.

(6) Come, J.; Naguib, M.; Rozier, P.; Barsoum, M. W.; Gogotsi, Y.; Taberna, P.-L.; Morcrette, M.; Simon, P. A Non-Aqueous Asymmetric Cell with a Ti_2C-Based Two-Dimensional Negative Electrode. *Journal of the Electrochemical Society* **2012**, *159* (8), A1368–A1373. https://dx.doi.org/10.1149/2.003208jes.

(7) Guo, Z.; Zhou, J.; Sun, Z. New Two-Dimensional Transition Metal Borides for Li Ion Batteries and Electrocatalysis. *Journal of Materials Chemistry A* **2017**, *5* (45), 23530–23535. https://doi.org/10.1039/C7TA08665B.

(8) Chaudhari, N. K.; Jin, H.; Kim, B.; San Baek, D.; Joo, S. H.; Lee, K. MXene: An Emerging Two-Dimensional Material for Future Energy Conversion and Storage

Applications. *Journal of Materials Chemistry A* **2017**, *5* (47), 24564–24579. https://doi.org/10.1039/C7TA09094C.

(9) Tang, H.; Hu, Q.; Zheng, M.; Chi, Y.; Qin, X.; Pang, H.; Xu, Q. MXene–2D Layered Electrode Materials for Energy Storage. *Progress in Natural Science: Materials International* **2018**, *28* (2), 133–147. https://doi.org/10.1016/j.pnsc.2018.03.003.

(10) Li, H.; Hou, Y.; Wang, F.; Lohe, M. R.; Zhuang, X.; Niu, L.; Feng, X. Flexible All-solid-state Supercapacitors with High Volumetric Capacitances Boosted by Solution Processable MXene and Electrochemically Exfoliated Graphene. *Advanced Energy Materials* **2017**, *7* (4), 1601847. https://doi.org/10.1002/aenm.201601847.

(11) Yan, J.; Ren, C. E.; Maleski, K.; Hatter, C. B.; Anasori, B.; Urbankowski, P.; Sarycheva, A.; Gogotsi, Y. Flexible MXene/Graphene Films for Ultrafast Supercapacitors with Outstanding Volumetric Capacitance. *Advanced Functional Materials* **2017**, *27* (30), 1701264. https://doi.org/10.1002/adfm.201701264.

(12) Liang, X.; Garsuch, A.; Nazar, L. F. Sulfur Cathodes Based on Conductive MXene Nanosheets for High-performance Lithium–Sulfur Batteries. *Angewandte Chemie International Edition* **2015**, *54* (13), 3907–3911. https://doi.org/10.1002/anie.201410174.

(13) Tang, Q.; Zhou, Z.; Shen, P. Are MXenes Promising Anode Materials for Li Ion Batteries? Computational Studies on Electronic Properties and Li Storage Capability of Ti_3C_2 and $Ti_3C_2X_2$ (X= F, OH) Monolayer. *Journal of the American Chemical Society* **2012**, *134* (40), 16909–16916. https://doi.org/10.1021/ja308463r.

(14) Khazaei, M.; Ranjbar, A.; Arai, M.; Sasaki, T.; Yunoki, S. Electronic Properties and Applications of MXenes: A Theoretical Review. *J. Mater. Chem. C* **2017**, *5* (10), 2488–2503. https://doi.org/10.1039/C7TC00140A.

(15) Kurra, N.; Ahmed, B.; Gogotsi, Y.; Alshareef, H. N. MXene-on-Paper Coplanar Microsupercapacitors. *Advanced Energy Materials* **2016**, *6* (24), 1601372. https://doi.org/10.1002/aenm.201601372.

(16) Pomerantseva, E.; Bonaccorso, F.; Feng, X.; Cui, Y.; Gogotsi, Y. Energy Storage: The Future Enabled by Nanomaterials. *Science* **2019**, *366* (6468). https://dx.doi.org/10.1126/science.aan8285.

(17) Anasori, B.; Lukatskaya, M. R.; Gogotsi, Y. 2D Metal Carbides and Nitrides (MXenes) for Energy Storage. *Nature Reviews Materials* **2017**, *2* (2), 1–17. https://doi.org/10.1038/natrevmats.2016.98.

(18) Zhao, M.-Q.; Ren, C. E.; Ling, Z.; Lukatskaya, M. R.; Zhang, C.; Van Aken, K. L.; Barsoum, M. W.; Gogotsi, Y. Flexible MXene/Carbon Nanotube Composite Paper with High Volumetric Capacitance. *Advanced materials* **2015**, *27* (2), 339–345. https://doi.org/10.1002/adma.201404140.

(19) Ling, Z.; Ren, C. E.; Zhao, M.-Q.; Yang, J.; Giammarco, J. M.; Qiu, J.; Barsoum, M. W.; Gogotsi, Y. Flexible and Conductive MXene Films and Nanocomposites with High Capacitance. *Proceedings of the National Academy of Sciences* **2014**, *111* (47), 16676–16681. https://doi.org/10.1073/pnas.1414215111.

(20) Naguib, M.; Kurtoglu, M.; Presser, V.; Lu, J.; Niu, J.; Heon, M.; Hultman, L.; Gogotsi, Y.; Barsoum, M. W. Two-dimensional Nanocrystals Produced by Exfoliation of Ti_3AlC_2. *Advanced materials* **2011**, *23* (37), 4248–4253. https://doi.org/10.1002/adma.201102306.

(21) Liu, Y.-T.; Zhang, P.; Sun, N.; Anasori, B.; Zhu, Q.-Z.; Liu, H.; Gogotsi, Y.; Xu, B. Self-Assembly of Transition Metal Oxide Nanostructures on MXene Nanosheets for Fast and Stable Lithium Storage. *Advanced Materials* **2018**, *30* (23), 1707334. https://doi.org/10.1002/adma.201707334.

(22) Zhang, C.; Beidaghi, M.; Naguib, M.; Lukatskaya, M. R.; Zhao, M.-Q.; Dyatkin, B.; Cook, K. M.; Kim, S. J.; Eng, B.; Xiao, X. Synthesis and Charge Storage Properties of Hierarchical Niobium Pentoxide/Carbon/Niobium Carbide (MXene) Hybrid Materials. *Chemistry of Materials* **2016**, *28* (11), 3937–3943. https://doi.org/10.1021/acs.chemmater.6b01244.

(23) Rakhi, R. B.; Ahmed, B.; Anjum, D.; Alshareef, H. N. Direct Chemical Synthesis of MnO_2 Nanowhiskers on Transition-Metal Carbide Surfaces for Supercapacitor Applications. *ACS Appl. Mater. Interfaces* **2016**, *8* (29), 18806–18814. https://doi.org/10.1021/acsami.6b04481.

(24) Ahmed, B.; Anjum, D. H.; Hedhili, M. N.; Gogotsi, Y.; Alshareef, H. N. H_2O_2 Assisted Room Temperature Oxidation of Ti_2C MXene for Li-Ion Battery Anodes. *Nanoscale* **2016**, *8* (14), 7580–7587. https://doi.org/10.1039/C6NR00002A.

(25) Mashtalir, O.; Naguib, M.; Mochalin, V. N.; Dall'Agnese, Y.; Heon, M.; Barsoum, M. W.; Gogotsi, Y. Intercalation and Delamination of Layered Carbides and Carbonitrides. *Nature communications* **2013**, *4* (1), 1–7. https://doi.org/10.1038/ncomms2664.

(26) Xie, Y.; Kent, P. R. C. Hybrid Density Functional Study of Structural and Electronic Properties of Functionalized $Ti_{N+1}X_n$ (X= C, N) Monolayers. *Physical Review B* **2013**, *87* (23), 235441. http://dx.doi.org/10.1103/PhysRevB.87.235441.

(27) Liu, Y.; Xiao, H.; Goddard III, W. A. Schottky-Barrier-Free Contacts with Two-Dimensional Semiconductors by Surface-Engineered MXenes. *Journal of the American Chemical Society* **2016**, *138* (49), 15853–15856. https://doi.org/10.1021/jacs.6b10834.

(28) Liu, Y.; Stradins, P.; Wei, S.-H. Van Der Waals Metal-Semiconductor Junction: Weak Fermi Level Pinning Enables Effective Tuning of Schottky Barrier. *Science advances* **2016**, *2* (4), e1600069. https://dx.doi.org/10.1126/sciadv.1600069.

(29) Tahini, H. A.; Tan, X.; Smith, S. C. The Origin of Low Workfunctions in OH Terminated MXenes. *Nanoscale* **2017**, *9* (21), 7016–7020. https://doi.org/10.1039/C7NR01601H.

(30) Alhabeb, M.; Maleski, K.; Anasori, B.; Lelyukh, P.; Clark, L.; Sin, S.; Gogotsi, Y. Guidelines for Synthesis and Processing of Two-Dimensional Titanium Carbide ($Ti_3C_2T_x$ MXene). *Chem. Mater.* **2017**, *29* (18), 7633–7644. https://doi.org/10.1021/acs.chemmater.7b02847.

(31) Haider, A. J.; Jameel, Z. N.; Al-Hussaini, I. H. M. Review on: Titanium Dioxide Applications. *Energy Procedia* **2019**, *157*, 17–29. https://doi.org/10.1016/j.egypro.2018.11.159.

(32) Jung, H.-G.; Yoon, C. S.; Prakash, J.; Sun, Y.-K. Mesoporous Anatase TiO_2 with High Surface Area and Controllable Pore Size by F^--Ion Doping: Applications for High-Power Li-Ion Battery Anode. *J. Phys. Chem. C* **2009**, *113* (50), 21258–21263. https://doi.org/10.1021/jp908719k.

(33) Yasir, V. A.; MohanDas, P. N.; Yusuff, K. K. M. Preparation of High Surface Area TiO_2 (Anatase) by Thermal Hydrolysis of Titanyl Sulphate Solution. *International Journal of Inorganic Materials* **2001**, *3* (7), 593–596. https://doi.org/10.1016/S1466-6049(01)00171-4.

(34) Kresse, G.; Furthmüller, J. Efficiency of *Ab-Initio* Total Energy Calculations for Metals and Semiconductors Using a Plane-Wave Basis Set. *Computational Materials Science* **1996**, *6* (1), 15–50. https://doi.org/10.1016/0927-0256(96)00008-0.

(35) Kresse, G.; Furthmüller, J. Efficient Iterative Schemes for *Ab Initio* Total-Energy Calculations Using a Plane-Wave Basis Set. *Phys. Rev. B* **1996**, *54* (16), 11169–11186. https://doi.org/10.1103/PhysRevB.54.11169.

(36) Blöchl, P. E. Projector Augmented-Wave Method. *Phys. Rev. B* **1994**, *50* (24), 17953–17979. https://doi.org/10.1103/PhysRevB.50.17953.

(37) Kresse, G.; Joubert, D. From Ultrasoft Pseudopotentials to the Projector Augmented-Wave Method. *Phys. Rev. B* **1999**, *59* (3), 1758–1775. https://doi.org/10.1103/PhysRevB.59.1758.

(38) Perdew, J. P.; Burke, K.; Ernzerhof, M. Generalized Gradient Approximation Made Simple. *Phys. Rev. Lett.* **1996**, *77* (18), 3865–3868. https://doi.org/10.1103/PhysRevLett.77.3865.

(39) Grimme, S.; Ehrlich, S.; Goerigk, L. Effect of the Damping Function in Dispersion Corrected Density Functional Theory. *Journal of computational chemistry* **2011**, *32* (7), 1456–1465. https://doi.org/10.1002/jcc.21759.

(40) Becke, A. D.; Johnson, E. R. A Density-Functional Model of the Dispersion Interaction. *The Journal of chemical physics* **2005**, *123* (15), 154101. https://doi.org/10.1063/1.2065267.

(41) Grimme, S.; Antony, J.; Ehrlich, S.; Krieg, H. A Consistent and Accurate *Ab Initio* Parametrization of Density Functional Dispersion Correction (DFT-D) for the 94 Elements H-Pu. *The Journal of chemical physics* **2010**, *132* (15), 154104. https://doi.org/10.1063/1.3382344.

(42) Hope, M. A.; Forse, A. C.; Griffith, K. J.; Lukatskaya, M. R.; Ghidiu, M.; Gogotsi, Y.; Grey, C. P. NMR Reveals the Surface Functionalisation of Ti_3C_2 MXene. *Physical Chemistry Chemical Physics* **2016**, *18* (7), 5099–5102. https://doi.org/10.1039/C6CP00330C.

(43) Zhan, X.; Si, C.; Zhou, J.; Sun, Z. MXene and MXene-Based Composites: Synthesis, Properties and Environment-Related Applications. *Nanoscale Horizons* **2020**. https://doi.org/10.1039/C9NH00571D.

(44) Ghidiu, M.; Lukatskaya, M. R.; Zhao, M.-Q.; Gogotsi, Y.; Barsoum, M. W. Conductive Two-Dimensional Titanium Carbide "clay" with High Volumetric Capacitance. *Nature* **2014**, *516* (7529), 78–81. https://doi.org/10.1038/nature13970.

(45) Monkhorst, H. J.; Pack, J. D. Special Points for Brillouin-Zone Integrations. *Phys. Rev. B* **1976**, *13* (12), 5188–5192. https://doi.org/10.1103/PhysRevB.13.5188.

(46) Khazaei, M.; Arai, M.; Sasaki, T.; Ranjbar, A.; Liang, Y.; Yunoki, S. OH-Terminated Two-Dimensional Transition Metal Carbides and Nitrides as Ultralow Work Function Materials. *Physical Review B* **2015**, *92* (7), 075411. https://dx.doi.org/10.1103/PhysRevB.92.075411.

(47) Li, R.; Sun, W.; Zhan, C.; Kent, P. R. C.; Jiang, D. Interfacial and Electronic Properties of Heterostructures of MXene and Graphene. *Phys. Rev. B* **2019**, *99* (8), 085429. https://doi.org/10.1103/PhysRevB.99.085429.

(48) Yu, H.; Wang, Y.; Jing, Y.; Ma, J.; Du, C.-F.; Yan, Q. Surface Modified MXene-Based Nanocomposites for Electrochemical Energy Conversion and Storage. *Small* **2019**, *15* (25), 1901503. https://doi.org/10.1002/smll.201901503.

(49) Zhou, S.; Yang, X.; Pei, W.; Liu, N.; Zhao, J. Heterostructures of MXenes and N-Doped Graphene as Highly Active Bifunctional Electrocatalysts. *Nanoscale* **2018**, *10* (23), 10876–10883. https://doi.org/10.1039/C8NR01090K.

Chapter 5

Proton Dynamics and Interfacial Properties in Single Water Layer Confined by Graphene-MXene and MXene-MXene

5.1 Abstract

The reversible redox process delivers significant contributions to the energy density of pseudo-capacitors. Pseudo-capacitors store energy through surface or near surface redox reaction. The intercalated proton involved redox reactions play crucial role in the pseudocapacitance of MXene. To further enhance its performance, the hybridization with carbon-based materials make the composites possess outstanding capacitance and high retention. However, the fundamental understanding of energy storage mechanisms within

heterostructures is still lacking. Herein, we employ *ab initio* molecular dynamics (AIMD) simulations to study the proton-transfer and redox behavior in MXene involved dissimilar interface (graphene-$Ti_3C_2O_2$) confined water and compare to its behavior in MXene confined water (similar interface $Ti_3C_2O_2$-$Ti_3C_2O_2$). By increasing intercalated-proton concentration, the surface-redox reactions are initiated and becoming more active. The interfacial electron transfer induced electric field enhanced the proton redox reaction rate in graphene-$Ti_3C_2O_2$ confined water compare to $Ti_3C_2O_2$-$Ti_3C_2O_2$ system. These interfacial properties also affect proton transport behavior by forming denser hydrogen-bonded networks with well-organized water molecules, leading to an incipient increase of proton mobility at low proton concentration. Further increasing proton concentration lead to decreased proton diffusivity. This decreased diffusivity can be attributed to the restrictions from frequent surface redox to proton in-water transfer. In $Ti_3C_2O_2$-$Ti_3C_2O_2$, the repulsion between protons dominates the proton diffusion. Thus, a decreasing trend of the proton diffusion coefficient can be obtained with more intercalated-proton. As an initial attempt, our model explores and compares the effect from the interfacial properties and configurations to the intercalated-proton dynamics within the confined single water layer from the perspective of different types of interfaces.

5.2 Introduction

MXenes, a family of two-dimensional (2D) transition metal carbides and nitrides, firstly discovered in 2011,[1,2] has emerged as a fantastic material widely investigated in various fields, including energy storage,[3–7] membranes,[8,9] electronics,[10–12] sensors,[13–18] and

catalysts,[19–22] etc. Due to the high electrical conductivity and high volumetric capacitance, MXenes have be considered as a promising electrode material for energy storage.[23] Previous experimental studies revealed that proton-involved reversible surface redox reaction is the key process to induce the pseudocapacitive behavior of MXene electrodes in H_2SO_4 electrolyte.[24–26] The followed theoretical study showed that the thickness of the MXene-confined water layer impact the surface redox chemistry and proton in-water transfer.[27]

However, the self-restacking issue of pure MXene nanosheets hampered its capacitor performance. This issue can be resolved via hybridizing with carbon-based materials (e.g. graphene nano-flacks, carbon nanotubes), metal oxides, or polymers.[28–34] Meanwhile, those MXene-based composites showed superior specific capacitances with an ultra-long lifespan. For example, Fu et al. reported that graphene/Ti_2CT_x@polyaniline (PAN) composite exhibits higher specific capacitance and excellent cycling stability in H_2SO_4 electrolyte.[35] Gogotsi et al. prepared MXene/reduced graphene oxide (rGO) electrodes which can generate more electrochemical active sites for surface-redox and deliver a high volumetric capacitance.[6]

Theoretical studies on the interfaces of different heterostructure are also hot topics at present.[36,37] Li et al. examined the interfacial electric properties of various stacking types of graphene/MXene heterostructures and found that the charge transfer between different building blocks induced the interfacial electric fields.[38] However, fundamental understandings of the energy storage mechanisms (e.g. the ions/molecule transport) within these dissimilar interfaces are still elusive. To serve as an initial attempt, in this work, we

explored and compared the effects of the interfacial properties and configurations on proton dynamics within single water layer interface confined by graphene-MXene, and MXene-MXene. The proton was chosen because of its small size favorable for surface redox reactions.[39] Another reason is that acidic electrolytes are commonly used in aqueous-based electrochemical supercapacitors due to their superb ionic conductivity. The MXene referred to in this work are all $Ti_3C_2O_2$ since the -O terminations will be reduced to -OH in acid electrolyte through hydrogen binding. Below we first elaborate our computational methods.

5.3 Computational methods

Density functional theory (DFT) implemented by the Vienna *ab initio* Simulation Package (VASP[40,41]) was used for both structure optimization and *ab initio* molecular dynamics (AIMD) simulations. The electron-ion interactions were described by the projector augmented-wave (PAW[42,43]) methods while the electron exchange-correlation part was parameterized by the Perdew-Burke-Ernzerhof (PBE[44]) functional form of generalized gradient approximation (GGA). The kinetic energy cutoff 500 eV was used for the plane-wave basis set. Periodic boundary conditions have been utilized in all calculations with Grimme DFT-D3 (Becke-Jonson damping[45]) dispersion correction to account for the van der Waals (vDW) interactions.[46,47] Convergence criteria were set to 0.02 eV/Å in force and 10^{-5} eV in energy. The Brillouin zone was sampled by (3×3×1) Monkhorst-Pack grid[48] for geometry optimizations, while only gamma point for AIMD simulations.

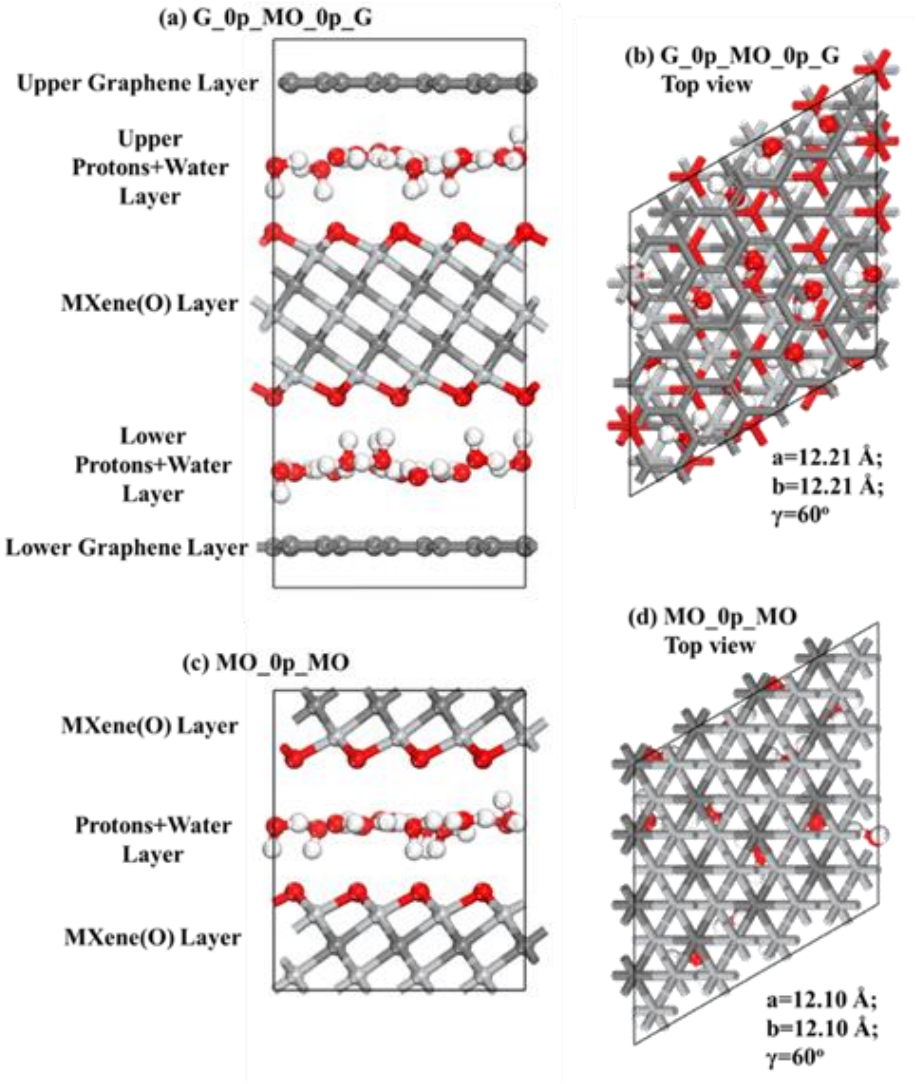

Figure 5.1 The optimized structures and the labeled building blocks for **(a)** G_0p_MO_0p_G and **(c)** MO_0p_MO ("0p" means no protons are intercalated at that interface); **(b)** and **(d)** provide the top-view and lattice parameters of **(a)** and **(c)**, respectively.

To model the structures, we used a monoclinic supercell for both graphene-MXene (A 4×4 supercell of $Ti_3C_2O_2$ is matched to a 5×5 supercell of graphene with the lattice mismatch ~1.3%) and MXene-MXene (4×4 supercell of $Ti_3C_2O_2$) systems. For

convenience, we use MO_MO and G_MO_G to represent various MXene-MXene and graphene-MXene systems in this work. In addition, the number of interfaces is 1 for MO_MO and 2 for G_MO_G. Within each interface, only a single water layer containing 12 water molecules and 0 to 3 protons were intercalated, and the whole simulation cell is charge neutral. We use "#p" to denote the number of protons being intercalated, e.g. G_1p_MO_1p_G stands for 1 proton per interface. The optimized structure of G_0p_MO_0p_G and MO_0p_MO are displays in Figure 5.1. The name of each building block as well as the a, b lattice constants and γ are also listed in Figure 5.1. For systems with same building block but different intercalated proton concentration, only c-lattice constant was optimized while other lattice parameters were kept unchanged. The optimal c-lattice constants are summarized in Table 5.S1.

The optimized structures were utilized as the initial structures for subsequent AIMD simulations. The AIMD were run in canonical ensemble (NVT) with the Nosé-thermostat at 300 K for 20 ps with 1 fs/time-step.[49–51] The last 15 ps, where the system temperature was stabilized, were used for the following analysis.

The proton diffusion coefficient can be calculated from the Einstein relation (equation 2.33) $D = \frac{1}{n}\frac{\partial(MSD)}{\partial t}$ $(n = 6\ for\ 3D\ system)$, where MSD stands for the mean square displacement of the proton-bonded O_0 atom. Detailed definitions are provided in supporting information.

5.4 Results and discussion

Given different interfaces, one may wonder how the proton behaves differently in confined single water layer. To address this problem, we evaluate proton transport subsequently.

5.4.1 Proton transport and surface redox reaction

In our simulation timescale, besides proton in-water transfer, the reversible surface redox process can also be observed. During this process, the proton in hydronium ion (H_3O^+) transfers to the surface-O of MXene forms the hydroxyl group (-OH). After a certain time interval, the -OH group will release the proton to nearby water molecule to form H_3O^+ again. Figure 5.2 depicted the number of proton in-water transfer events and surface redox reactions happened at each timestep along the whole trajectories. The proton in-water transfer happened much more frequently than surface-redox. Furthermore, more frequent surface redox reactions occur in G_MO_Gs with additional intercalated-proton, while a few redox events take place in MO_3p_MO. Thus, both interfacial proton concentration and interface compositions may impact proton surface-redox behavior. Due to proton's transitivity, the surface-redox can happen on different surface-O sites of MXene, which was primarily mediated by proton in-water transfer events (Figure 5.S2).

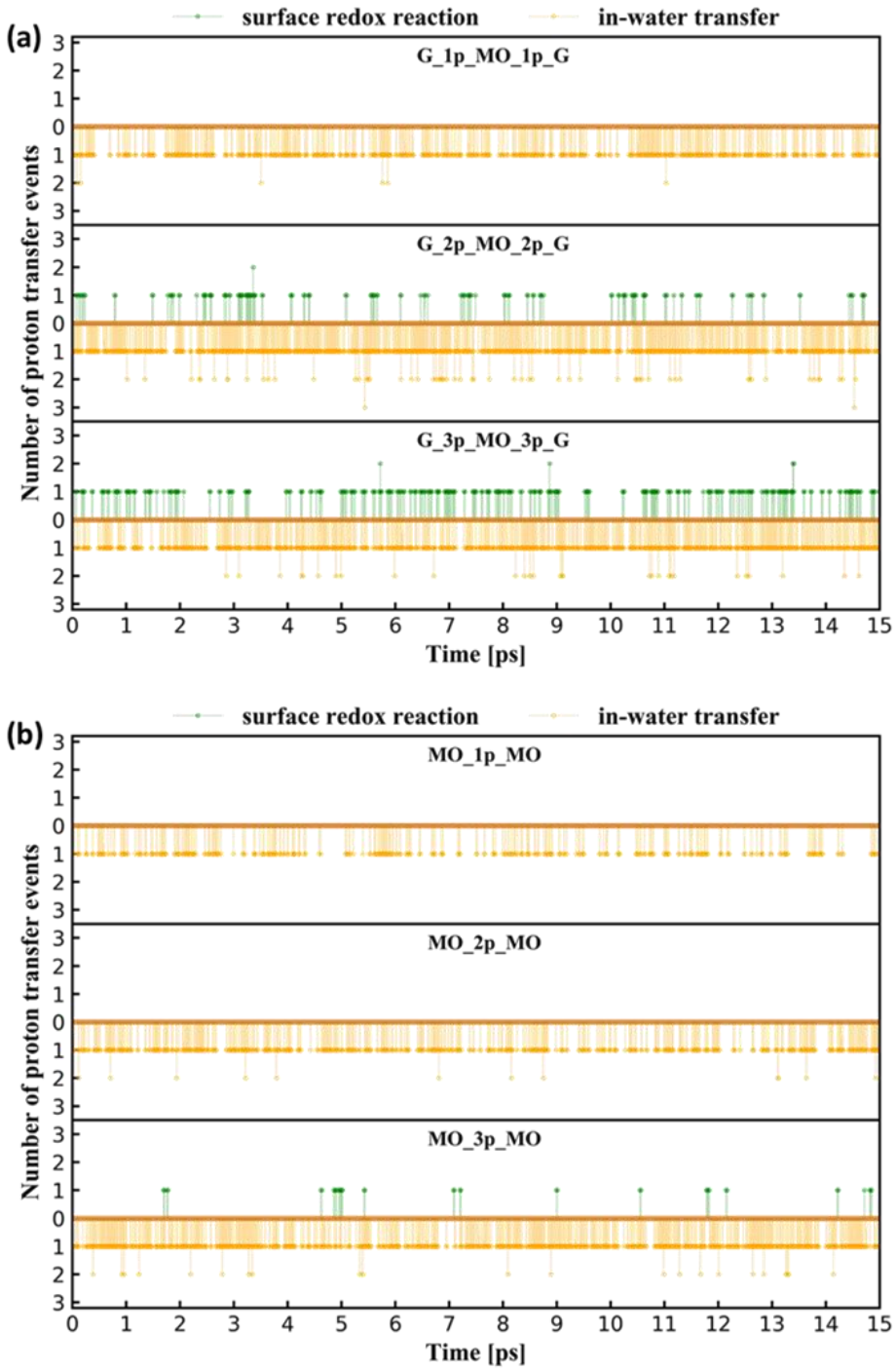

Figure 5.2 Number of proton surface-redox (green) versus in-water proton transfer (orange) events with time for **(a)** G_MO_Gs and **(b)** MO_MOs. Note that we count all protons inside each system.

The estimated surface redox rate constant is summarized in Table 5.1. Comparing the 3-proton per interface case, the rate constant for G_3p_MO_3p_G, 634 m/s, is about 9 times larger than that of MO_3p_MO, 68.6 m/s. This huge difference should be derived from proton transport mechanisms and the interfacial properties/configurations. Below, we begin to analyze the proton diffusivities.

Table 5.1 The calculated surface redox rate constants for different systems.

Systems	Graphene-MXene			MXene-MXene		
Proton number per interface	1	2	3	1	2	3
Surface redox rate constant [m/s]	-	430.0	634.25	-	-	68.6

5.4.2 Proton diffusivity within interfaces

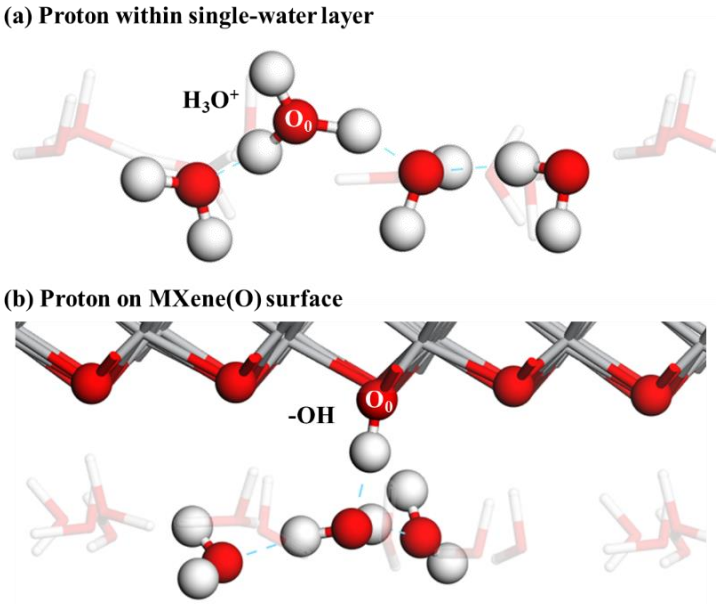

Figure 5.3 The identity of the proton-bonded O_0 inside **(a)** H_3O^+ within single water-layer, or **(b)** -OH group on the MXene surface.

The proton-bonded O_0—the O in the hydronium ion (H_3O^+) within water layer or the O from the hydroxyl group (-OH) on MXene surface (Figure 5.3**)**, was treated as the identity to describe the proton transferbehavior. The proton mobility can be quantified by the diffusion coefficients (Figure 5.4) through Einstein relation from the mean square displacement (MSD) results (Figure 5.S3(a)). When increasing intercalated-proton concentration, a decreasing trend of the diffusion coefficient is obtained for MO_MOs, while an increasing then decreasing trend is found for G_MO_Gs. In the next two subsections, we will give a detailed analysis on why proton mobility change with concentration for each system.

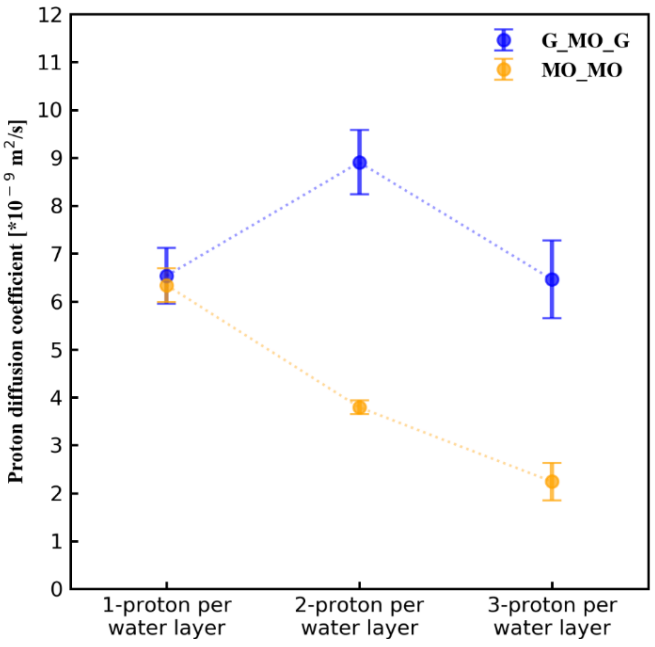

Figure 5.4 Proton diffusion coefficients for different systems calculated from the Einstein relation of mean square displacement (MSD) (Figure 5.S3(a)).

5.4.2.1 MXene-MXene interface

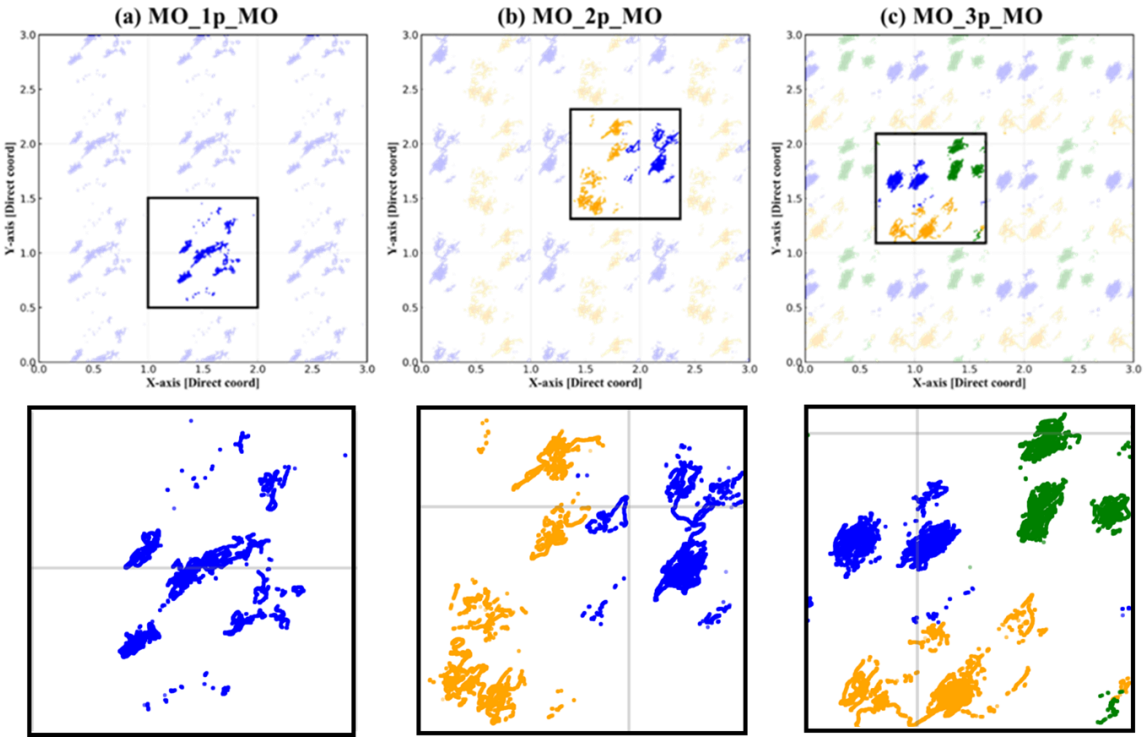

Figure 5.5 The continues O_0 paths (using the direct coordinate) for **(a)** MO_1p_MO, **(b)** MO_2p_MO, and **(c)** MO_3p_MO. We plotted a 3×3 unit-area (with 9 repeating units) for better representing the O_0 trajectory in the black squared unit space. Each color denotes a different proton-bonded O_0. The lower plots are the enlargement of the black square box from upper plots.

Through analyzing the percent of occupation time (Table 5.S2), either inside H_3O^+, or bind with MXene surface-O (-OH group), we found regardless of the proton concentration, >99% of the time proton stay within the water layer though few surface redox reactions happen in MO_3p_MO. Additionally, a larger decomposed diffusion coefficients within XY-plane (Figure 5.S3(b)) denotes that the proton in-water transfer mostly contributes to the proton diffusion in MO_MOs. Via plotting the XY-plane projected continuous O_0 paths (Figure 5.5), we found there are apparent gaps between

different O_0 trajectories. Those separations are originated from the proton repulsions within the single water-layer. Thus increasing proton concentration results in more localized proton movement, hence decreased proton diffusivity in MO_MOs.

5.4.2.2 Graphene-MXene interface

Table 5.2 Percent of occupation time when protons are in H_3O^+ in water layer or -OH group on MXene surface for G_MO_Gs.

Systems	% of occupation time	
	H_3O^+ in Water layer	-OH on MXene surface
G_1p_MO_1p_G	100	-
G_2p_MO_2p_G	96.20	3.80
G_3p_MO_3p_G	53.42	46.57

Likewise, we tabulated the percent of occupation time when the proton is in the H_3O^+ or -OH group for G_MO_Gs into Table 5.2. For high proton concentration system (G_3p_MO_3p_MO), 46.6% of the time, the proton were binding with MXene surface-O which largely restrict proton mobility, hence low proton diffusion coefficient. The restricted proton movement is further proved by the formation of more cluster-like O_0 paths as depicted in Figure 5.6(c). However, for both G_1p_MO_1p_MO and G_2p_MO_2p_MO, the proton in-water diffusion plays a pivotal role as protons stay inside H_3O^+ >95% of time. (This can be further confirmed by larger XY-plane proton diffusion coefficients suggested from Figure 5.S3(b)). Since under this circumstance, the in-water diffusion dominates the proton movement as showed in previous MO_MOs, a rinsing question would be why the proton diffusion coefficient trend different in G_MO_Gs. This

abnormal trend might ascribed to the dissimilar interface enhanced water mobility or the induced denser hydrogen-bonded networks.

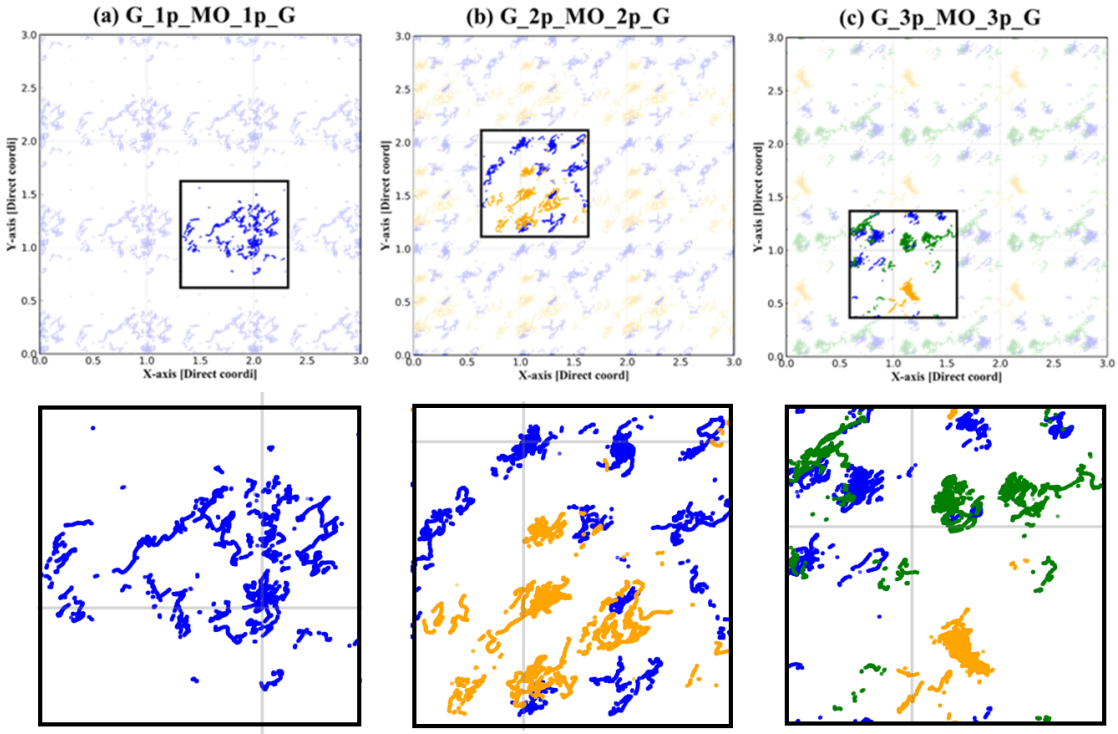

Figure 5.6 The continues O_0 paths (using the direct coordinate) for **(a)** G_1p_MO_1p_G, **(b)** G_2p_MO_2p_G, and **(c)** G_3p_MO_3p_G. We plotted a 3×3 unit-area (with 9 repeating units) for better representing the O_0 trajectory in black squared unit space. Each color denotes a different proton-bonded O_0. Due to the relative symmetric structures of G_MO_Gs, only the O_0 paths within the "Lower Protons+Water Layer" were plotted. See Figure 5.1 for the label of the building block. The lower plots are the enlargement of the black square box from upper plots.

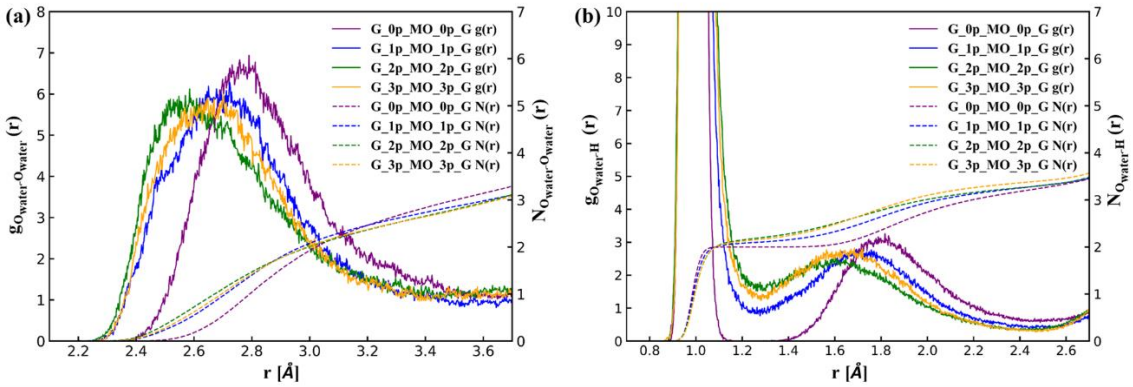

Figure 5.7 Radial distribution function (RDF) g(r) and coordination number N(r) of **(a)** O_{water}-O_{water}, **(b)** O_{water}-H(including protons) for G_MO_Gs.

To rule out the effect of fast water mobility, we estimated the diffusion coefficients of water molecules (O_{water}) (Figure 5.S4). We found that water became motionless after additional intercalated-proton. From the perspective of the hydrogen-bonded networks, the radial distribution function (RDF) g(r) and coordination number N(r) of the O_{water}-O_{water} and O_{water}-H (including protons) are plotted in Figure 5.7. When changing from G_1p_MO_1p_MO to G_2p_MO_2p_MO, both O_{water}-O_{water} peak and H-bonding peak (the peak locate at 1.6~1.8 Å) shifted left, which suggests reduced hydrogen bond length, indicating the denser hydrogen-bonded networks within interfaces. Moreover, we also investigated the water dipole orientation θ and OH bond orientation β to check water configurations as shown in Figure 5.8. The normalized distribution plot shows that with respect to growing proton concentration: i) the narrower and higher peak will appear within region $40^o<\theta<75^o$; ii) the more obvious separated peaks will emerge at regions $10^o<\beta<30^o$ and $80^o<\beta<110^o$. These results demonstrate the formation of more directional water structures with one OH bond pointing toward the MXene surface and the other pointing

parallelly to XY-plane. With denser hydrogen-bonded networks and more oriented water molecules, the proton in-water transfer will become easier and faster, thus an increased proton diffusion coefficient is obtained for G_2p_MO_2p_MO.

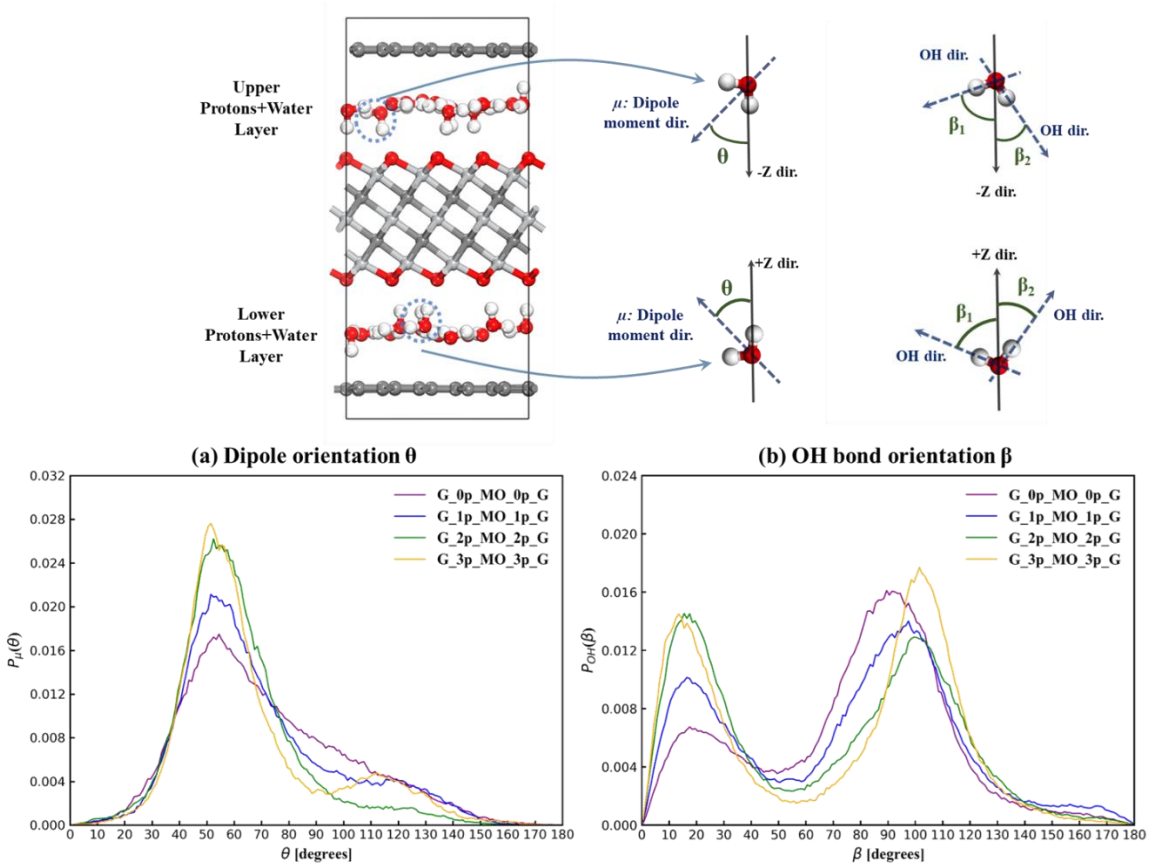

Figure 5.8 The normalized distribution of **(a)** the dipole orientation θ and **(b)** OH bond orientation β for water molecules (exclude the hydronium ion) for G_MO_Gs. A schematic of water orientations for θ and β is illustrated in the top plots. The ±Z-dir directed perpendicularly from graphene to MXene.

5.4.3 Interfacial properties and configurations

In this section, we will explore the effects of the interfacial properties and configurations on the proton dynamic movements. We firstly probe the interfacial electric properties next.

5.4.3.1 Interfacial electric field

Regardless of the intercalated water layer, the electrons still transfer between different building blocks. (Detailed bader charge analysis (Figure 5.S5) is included in supporting information.) In G_MO_Gs, an interfacial electronic field directed from graphene to MXene layer will always be there due to the positively charged graphene and negatively charged MXene (Figure 5.9). In contrast to G_MO_Gs, no interfacial electric field appears in MO_MOs. For both systems, most of the electrons are transferred from interfaces ("Upper/Lower Protons+Water Layer") to MXene, making MXene more negatively charged with increasing intercalated-proton concentration. Those interfacial electronic properties will help to align and attract OH bonds from water molecules, making a more directional water layer.

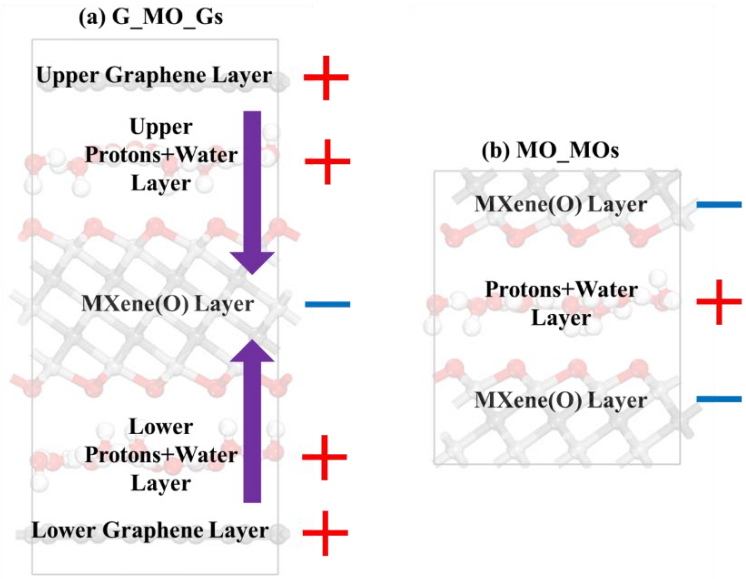

Figure 5.9 Diagram of the charge sign (+/-) for different building blocks and the interfacial electronic field directions (the purple array) for **(a)** G_MO_Gs, and **(b)** MO_MOs. See supporting information for detailed bader charge analysis.

5.4.3.2 Interfacial configurations

For G_MO_Gs, with increased intercalated-proton number, the greater interfacial electric field induces stronger interlayer interactions, leading to the reduced O_{water}-O_{MXene} (O_{MXene} denotes surface-O from MXene) distance (Figure 5.S6). This closer water-MXene interlayer distance assists to raise chances for protons in water to encounter MXene surface, thereby a higher surface redox rate is gained for G_3p_MO_3p_G 634.5 m/s than G_2p_MO_2p_G 430 m/s (Table 5.1).

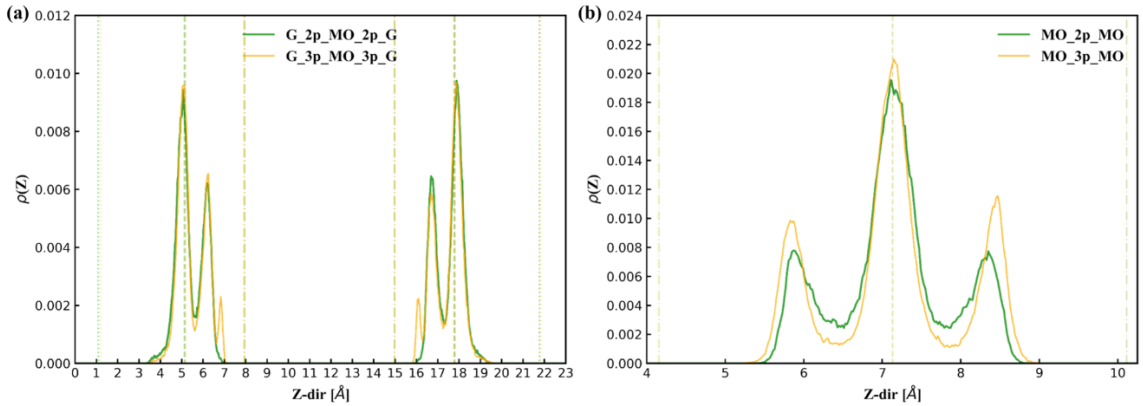

Figure 5.10 A histogram of the positions of H (including the protons) atoms along Z-direction from trajectories for **(a)** G_2p_MO_2p_G and G_3p_MO_3p_G, **(b)** MO_2p_MO and MO_3p_MO. ρ(Z) corresponds to the normalized distribution function along Z-direction. Dashed line, O_{MXene} layer; Dotted line, graphene layer; Dash-dotted line, O_{water} layer. These line positions are averaged from the corresponding atom positions along trajectories.

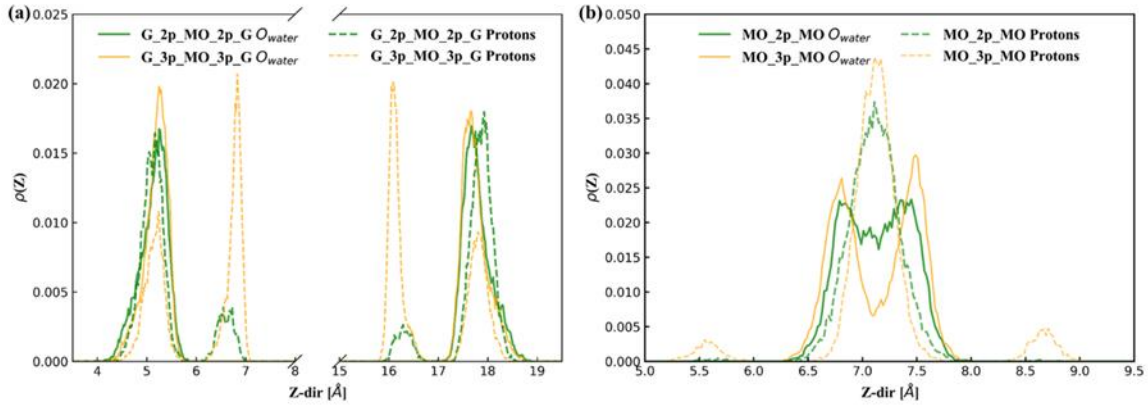

Figure 5.11 A histogram of the O_{water} and proton positions along Z-direction from trajectories for **(a)** G_2p_MO_2p_G and G_3p_MO_3p_G, **(b)** MO_2p_MO and MO_3p_MO. ρ(Z) corresponds to the normalized distribution function along Z-direction.

According to Table 5.1, the surface redox rate is always larger in G_MO_Gs than in MO_MOs at the higher proton-intercalated concentration (2-3 protons per interface). This is owing to their different interfacial configurations and properties. According to the unit-cell construction, the interface is exposed to just one side of the MXene surface in

G_MO_Gs, while both-sides in MO_MOs. Moreover, the graphene layer is hydrophobic while the -O terminated MXene is hydrophilic. Thus, the distribution of H (including protons) positions along Z-direction from trajectories (Figure 5.10) shows a greater H density within water-MXene interlayer in G_MO_Gs and a symmetric H distribution about the O_{water} layer in MO_MOs. We further plot the distribution of O_{water} and proton positions as shown in Figure 5.11. More interestingly, unlike G_(2-3)p_MO_(2-3)p_G that only one O_{water} peak appears at each interface, there are two separated O_{water} peaks in MO_(2-3)p_MO. With more intercalated-protons, the separated O_{water} peaks in MO_MO become more conspicuous, indicating that the water molecules move towards either side of the MXene surfaces to form inner-separation water regions. (The distribution plots of the water dipole orientation θ and OH bond orientation β further proves these separations (Figure 5.S7**)**.) Meanwhile, the higher and narrower proton position peak between the two separated O_{water} peaks illustrates that the protons prefer to act like the bridge between water molecules from the inner-separation water regions in MO_MOs. (Figure 5.S8 provides several snapshots showing the structures of the proton-involved H_3O^+/-OH group with the nearest water molecule.) The preference of the proton behavior decreases its possibility to run into MXene surfaces, thereby less-frequent surface-redox reactions and a smaller surface redox rate will be the case for MO_MOs. Besides, our group previous study on MXene showed that the capability for storing protons in $Ti_3C_2O_2$ is about 0.5 H^+/formula-unit.[52] In terms of our study, the largest proton storage is around 0.38H^+/formula-unit and 0.19H^+/formula-unit for G_3p_MO_3p_MO and MO_3p_MO, respectively. The relative

smaller proton storage value for MO_3p_MO may also be the cause of fewer surface redox activities than G_3p_MO_3p_MO.

5.5 Conclusions

Through employing *ab-initio* molecular dynamics (AIMD) methodology, the proton transport mechanisms and interfacial properties were thoroughly explored. The intercalated-proton concentration did impact the proton transport and surface redox processes. With more intercalated-protons, proton repulsions mainly influence the proton in-water transfer in MO_MOs, resulting in a decreased proton mobility. For G_MO_Gs, the incipient increase of the proton diffusion coefficient is primarily attributed to the denser hydrogen-bonded networks with more directional water structures. The frequent proton surface-redox and longer-time that proton binding with the MXene surface-O restricts the proton in-water transfer, leading to the further decreased proton diffusion coefficient in G_3p_MO_3p_G. Moreover, the interfacial configurations and electric properties may also be the factor to control the proton dynamic behaviors. In general, our study provides detailed comparisons of the proton transport mechanisms within single water layer confined by different types of interfaces.

Supporting information

5.S1 Calculation details about MSD

The time-dependent mean square displacement (MSD) of the proton-bonded O_0 was estimated from equation 2.32. The diffusion coefficient (D) is estimated by the Einstein relation (equation 2.33) — the slope of the MSD divided by n. In our study, the slop is obtained by fitting the virtual linear region from the MSD curves (averaged over all snapshots within 1.0 ps – 4.5 ps).

5.S2 Optimal c-lattice constants and water densities

Table 5.S1 The optimal c-lattice constants and water densities for different systems.

Systems	Optimal c-lattice constant [Å]	Water density [g/cm^3]
G_0p_MO_0p_G	23.0	0.862
G_1p_MO_1p_G	23.0	0.862
G_2p_MO_2p_G	23.0	0.862
G_3p_MO_3p_G	23.0	0.862
MO_0p_MO	12.5	1.029
MO_1p_MO	12.5	1.029
MO_2p_MO	13.0	0.871
MO_3p_MO	13.0	0.871

Table 5.S1 shows the optimal c-lattice constant and water density for each system. Through scanning the c-lattice (with an increment value 0.5 Å) as a function of the total unit-cell energy, the optimal c-lattice constant is determined at the point where the lowest total unit-cell energy is obtained (Figure S1). From this table, all G_MO_Gs have the same c-lattice parameter and water density, while for MO_MOs, the increase of the optimal c-lattice constant from 1 to 2 protons per interface leads to the decrease of the corresponding

water density. It is worth to mention that the increase of the c-lattice constant in MO_MOs will not affect any results investigated in this work.

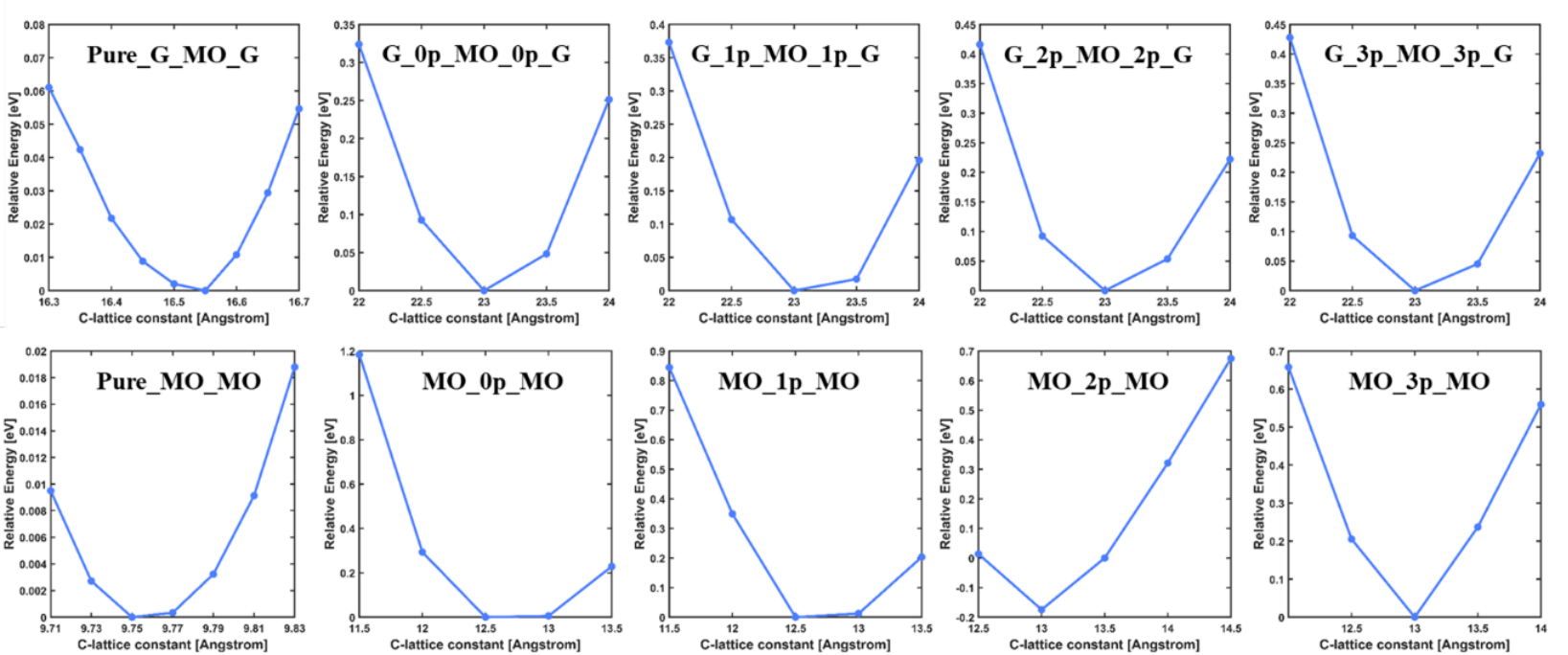

Figure 5.S1 Relative total unit-cell energy as a function of the c-lattice parameter of different systems with/without confined single water layer and proton. The Pure_G_MO_G and Pure_MO_MO refer to the systems with no intercalated water layer and protons.

5.S3 Index changes for the proton-bonded O_0

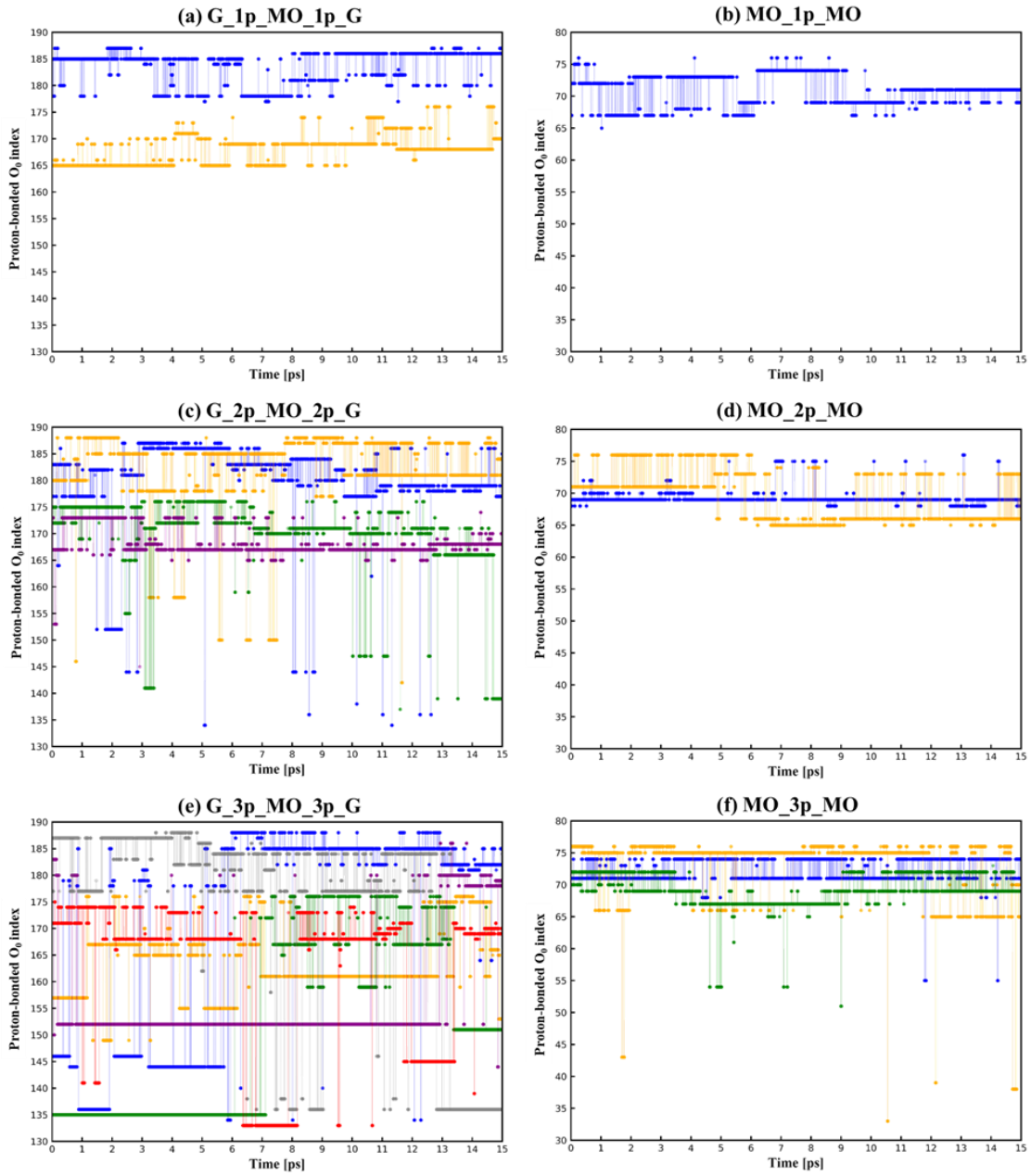

Figure 5.S2 The time-dependent index changes of proton-bonded O_0 along trajectories **(a), (c), (e)** for different G_MO_G; **(b), (d), (e)** for different MO_MOs. The index range of the surface-O from MXene is 133-164 for G_MO_Gs and 33-64 for MO_MOs, while the index range for the O in the water layer is 165-188 for G_MO_Gs and 65-76 for MO_MO. Different color denotes different proton-bonded O_0.

Figure 5.S2 illustrates the time-dependent index change of the proton-bonded O_0 along AIMD trajectories for different systems. Whenever there is a proton transfer from water to MXene surface, the proton-bonded O_0 index will be located within the index range 133-164 for G_MO_Gs and 33-64 for MO_MOs. The multiple index changes within this range along the same continues O_0 path, indicating that protons were transferred to different surface-O sites.

5.S4 Total/decomposed proton diffusion coefficients

The total MSD as a function of time for the proton-bonded O_0 is shown in Figure 5.S3(a). To evaluate the contributions to the total diffusion coefficients, the decomposed XY-plane ($n = 4$ for a 2D system) and Z-direction ($n = 2$ for a 1D system) (Figure 5.S3(b)) diffusion coefficient are obtained by projecting the proton-bonded O positions to the relative direction in MSD. Since a single water-layer is applied at each interface, the XY-plane proton diffusion is mainly due to proton in-water transfer, while the Z-direction diffusion corresponds to proton jumping between water and MXene surface (namely surface redox reactions). As a result, the XY-plane diffusion contributed primarily to the proton diffusion in all MO_MOs. In G_MO_Gs, the incipient increase of the diffusion coefficient should be attributed to the faster proton in-water transfer, and the latter decreased value is due to the more frequent proton surface-redox behavior.

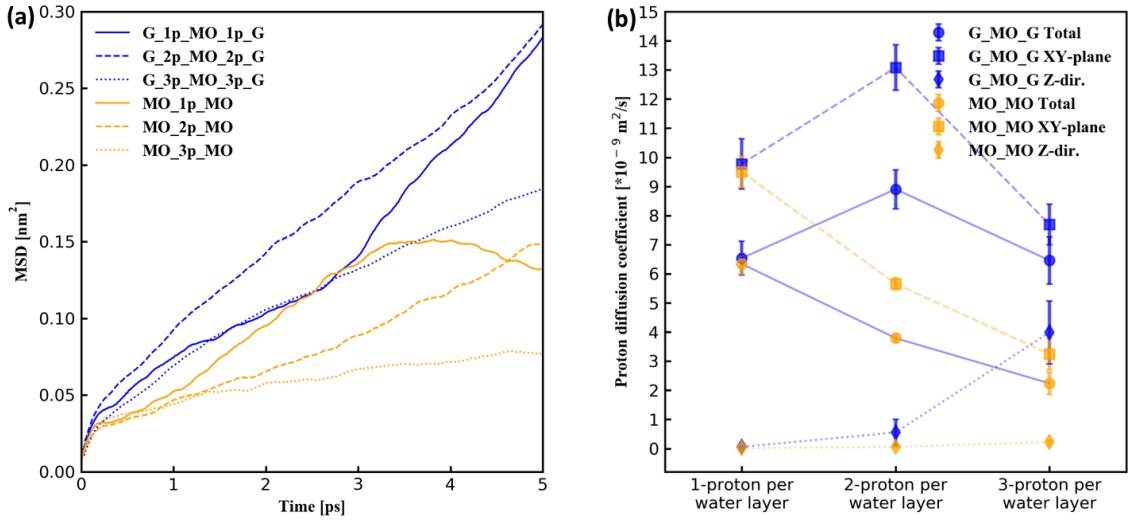

Figure 5.S3 Proton diffusion within the interface: **(a)** Total mean-squared displacement (MSD) as a function of time for O_0; **(b)** Total and decomposed (XY-plane and Z-dir.) proton diffusion coefficients for different systems.

5.S5 Percent of occupation time for different proton-involved structures

Table 5.S2 suggests that protons prefer to stay as H_3O^+ in water layer >99% of the time for all MO_MOs. This result provides additional evidence that proton in-water transfer plays a key role during the whole proton diffusion in MO_MOs.

Table 5.S2 Percent of occupation time when protons are in H_3O^+ in water layer or -OH group on MXene surface for MO_MOs.

Systems	% of occupation time	
	H_3O^+ in Water layer	-OH on MXene surface
MO_1p_MO	100	-
MO_2p_MO	100	-
MO_3p_MO	99.29	0.71

5.S6 Total/decomposed O_{water} diffusion coefficients

The diffusion coefficients are found to be in a decreasing trend for O in the water layer (O_{water}) with increased intercalated-proton concentration, indicating that water molecules become more motionless (Figure 5.S4). Here, we included the H_3O^+ species in our calculations because they influence the water dynamic behavior dramatically within single water layer.

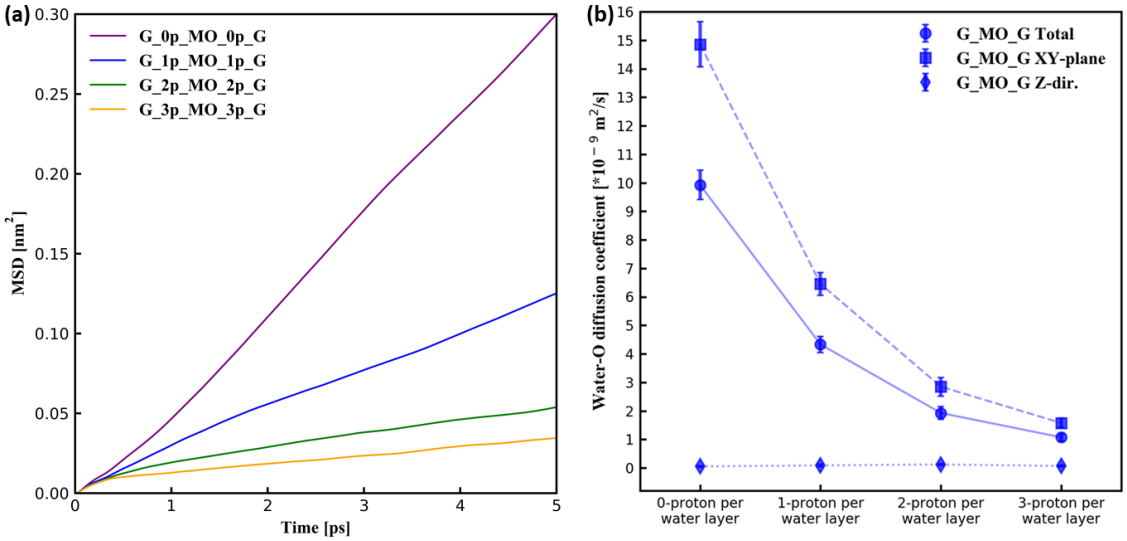

Figure 5.S4 The O_{water} diffusion within the interface: **(a)** Total mean-squared displacement (MSD) as a function of time for O_{water}; **(b)** Total and decomposed (XY-plane and Z-dir.) O_{water} diffusion coefficients.

5.S7 Bader charge analysis for different building blocks

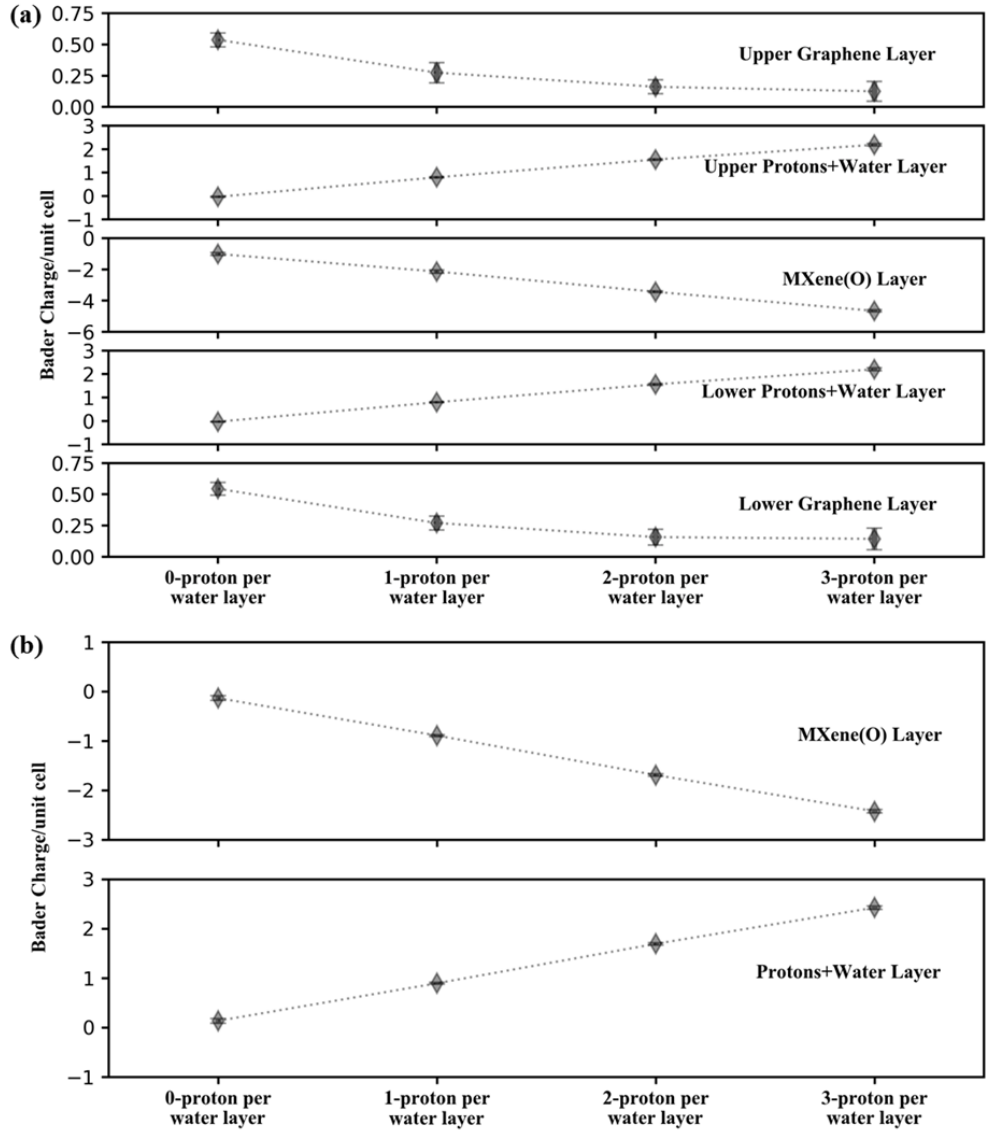

Figure 5.S5 The averaged bader charge per unit cell (from 10 randomly selected snapshots) of each building block for **(a)** G_MO_Gs and **(b)** MO_MOs. Note that the y-axis range is different for different building blocks. See **Figure 5.1** for the names of different building blocks.

We calculated the Bader charge for different building blocks of 10 randomly selected snapshots for all systems under investigation. The averaged Bader charge values

with small standard deviations were presented in Figure 5.S5. Accompanied by the increased intercalated-proton concentration, for G_MO_Gs, a fraction of electrons goes from interfaces ("Upper/Lower Protons+Water Layer") to graphene, and another fraction goes to MXene. In return, we obtain a more negatively charged MXene and more positively charged interface. The slight reduced positive charge in graphene does not impact the presence of the interfacial electric field with the direction from graphene to MXene. Contrary to G_MO_G, no interfacial electric field appears within the interface in MO_MOs while the MXene still becomes more negatively charged due to the interfacial electron transfer.

5.S8 Radial distribution function (RDF) of O_{water}-O_{MXene}

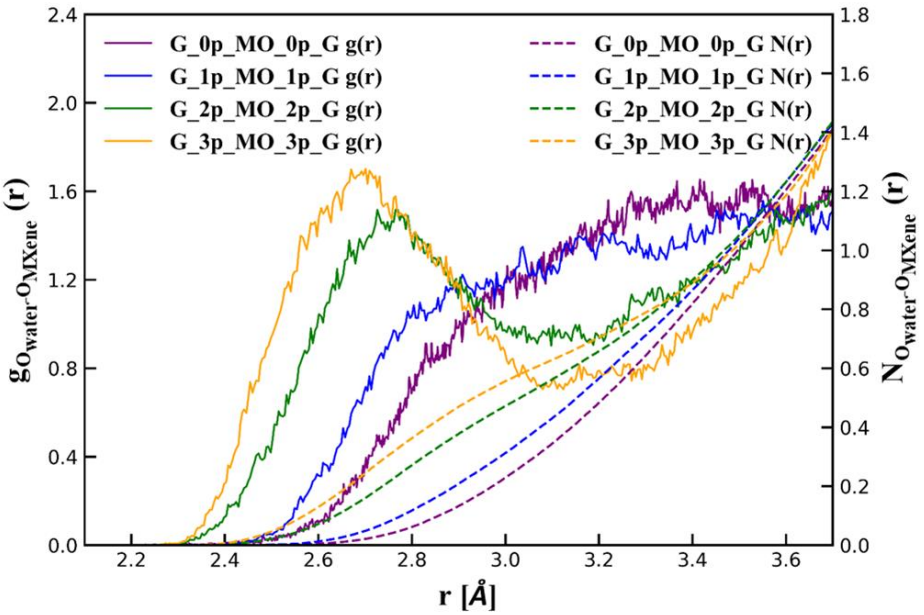

Figure 5.S6 The radial distribution function (RDF) g(r) and coordination number N(r) of O_{water}-O_{MXene} for G_MO_Gs.

Figure 5.S6 displays the radial distribution function (RDF) g(r) and coordination number N(r) of the distance between the O from water (O_{water}) and the surface-O from MXene (O_{MXene}) for different G_MO_Gs. The left-shift peak in terms of additional intercalated-proton suggests a reduced O_{water}-O_{MXene} distance. Hence, the water layer comes closer to the MXene surface, leading to a higher possibility for protons to transfer between water and MXene surface.

5.S9 The distribution of θ and β in MO_(2-3)p_MO

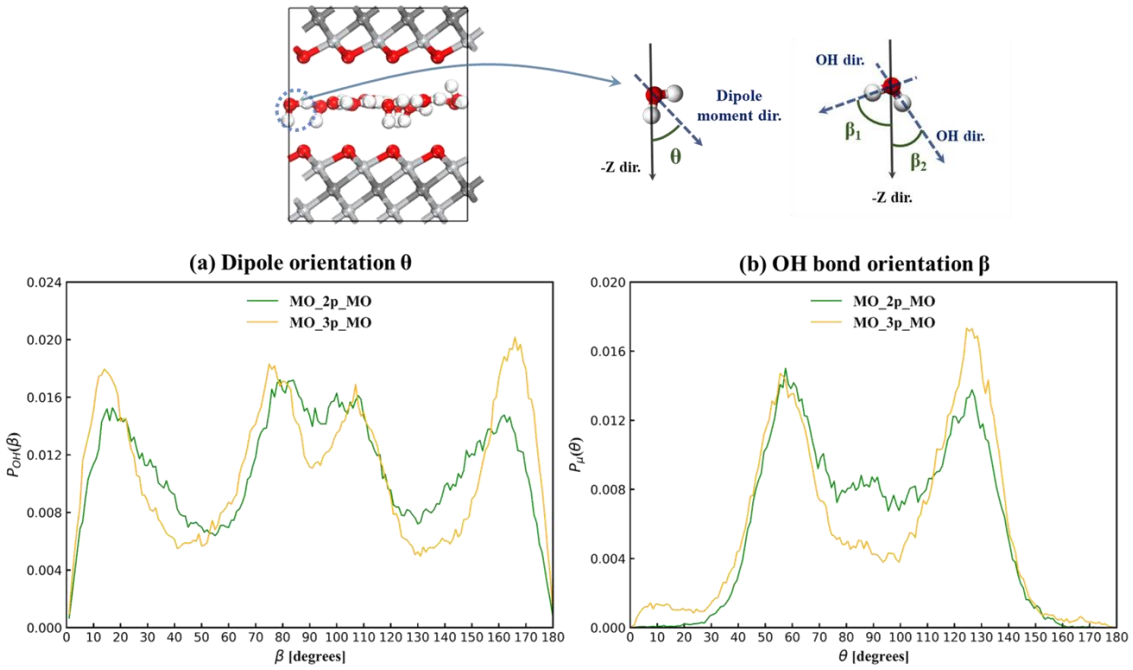

Figure 5.S7 The normalized distribution of **(a)** the dipole orientation θ and **(b)** OH bond orientation β for water molecules (exclude the hydronium ion) for MO_(2-3)p_MOs. A schematic of water orientations for θ and β is illustrated in the top plots. The -Z-dir directed perpendicularly from the upper to the lower MXene surface.

The normalized distribution plots (Figure 5.S7) for MO_(2-3)p_MO suggests that with increasing intercalated-proton number, more distinct 2 θ (water dipole orientation) peaks and 4 β (OH bond orientation) peaks will present. This phenomenon indicates that the interfacial water molecules are attracted by either side of the MXene surface, leading to the interfacial water layer separations. Furthermore, more oriented water molecules will present since the peaks become more apparent within the regions: $50^{o}<\theta<70^{o}$, $115^{o}<\theta<135^{o}$ and $10^{o}<\beta<30^{o}$, $150^{o}<\beta<170^{o}$. This means that one OH bond from water molecule is more inclined to point toward the MXene surface and the other points parallelly to XY-plane. Hence, similar to the case in G_MO_Gs, the water configurations become more directional in MO_MOs.

5.S10 Snapshots of the proton position in MO_(2-3)p_MO

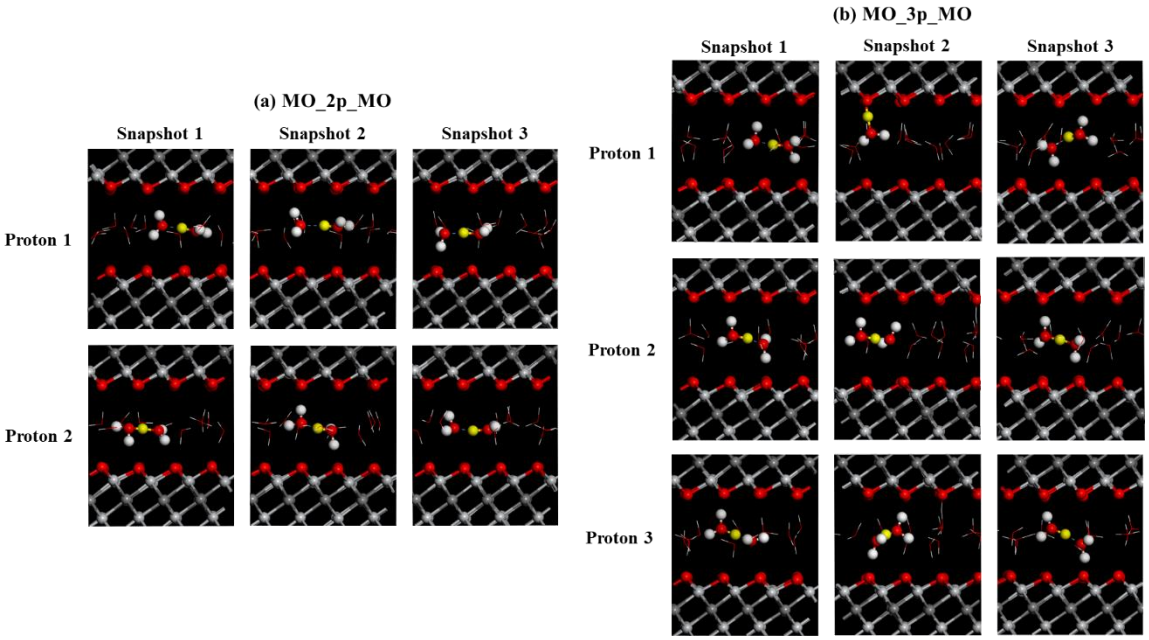

Figure 5.S8 Three-snapshot structures of the proton-involved H_3O^+/-OH group and the nearest water molecule for **(a)** MO_2p_MO and **(b)** MO_3p_MO. The proton is highlighted in yellow. Light gray, Ti; dark gray, C; red, O; white, H

In MO_MOs, the interface is exposed to both-sides of MXene surfaces. According to the interfacial electron transfer analysis above, the more the intercalated-proton, the stronger the interactions between the interface ("Upper/Lower Protons+Water Layer") and MXene. From MO_2p_MO to MO_3p_MO, the water molecules move towards either side of the MXene surfaces, resulting in the inner water-layer separation. Figure 5.S8 schematically shows the structures of the proton-involved H_3O^+/-OH group and the nearest water molecules from three randomly chosen snapshots. In comparison with MO_2p_MO, protons in MO_3p_MO are more favorable to serve as the bridge connecting water molecules from the inner separated water-layers.

5.S11 Bader charge analysis for proton in water and on MXene surface

In our proton transport studies, the proton can either bind with the water molecule to form hydronium ion (H_3O^+) or bind with the surface-O from MXene to form the hydroxyl group (-OH). One may wonder, "will there be any difference for the interfacial electron transfer under these two different proton binding circumstances". To address this problem, we further sort out the snapshots from the trajectory. Note that we have systems with different intercalated-proton numbers. Using the complicated G_MO_Gs for an explanation, at lower intercalated-proton concentration, the protons are all staying with water molecules. With additional proton being intercalated, multiple reversible surface redox reactions take place, whereas not all protons run into the MXene surface at the same time. When it comes to the higher intercalated-proton concentration, by inspecting the trajectory, at least two protons are binding with the MXene surface-O simultaneously for every snapshot (Figure 5S.9). Hence, we will classify the snapshot into "Several protons bind with MXene surface-O (-OH)" category whenever at least one proton forms -OH on MXene surface, and the other category would be "All protons bind with water (H_3O^+)".

We randomly selected 10 snapshots for each proton binding situation, the corresponding averaged bader charge value with standard deviation for each building block is depicted in Figure 5.S10. With respect to increasing intercalated-proton numbers, the occurrence of the proton surface-redox will not impact the general trends of the bader charge for each building block. Even for G_2p_MO_2p_G and MO_3p_MO in which both proton binding situations are involved along trajectories, the bader charge difference between those two situations is almost negligible.

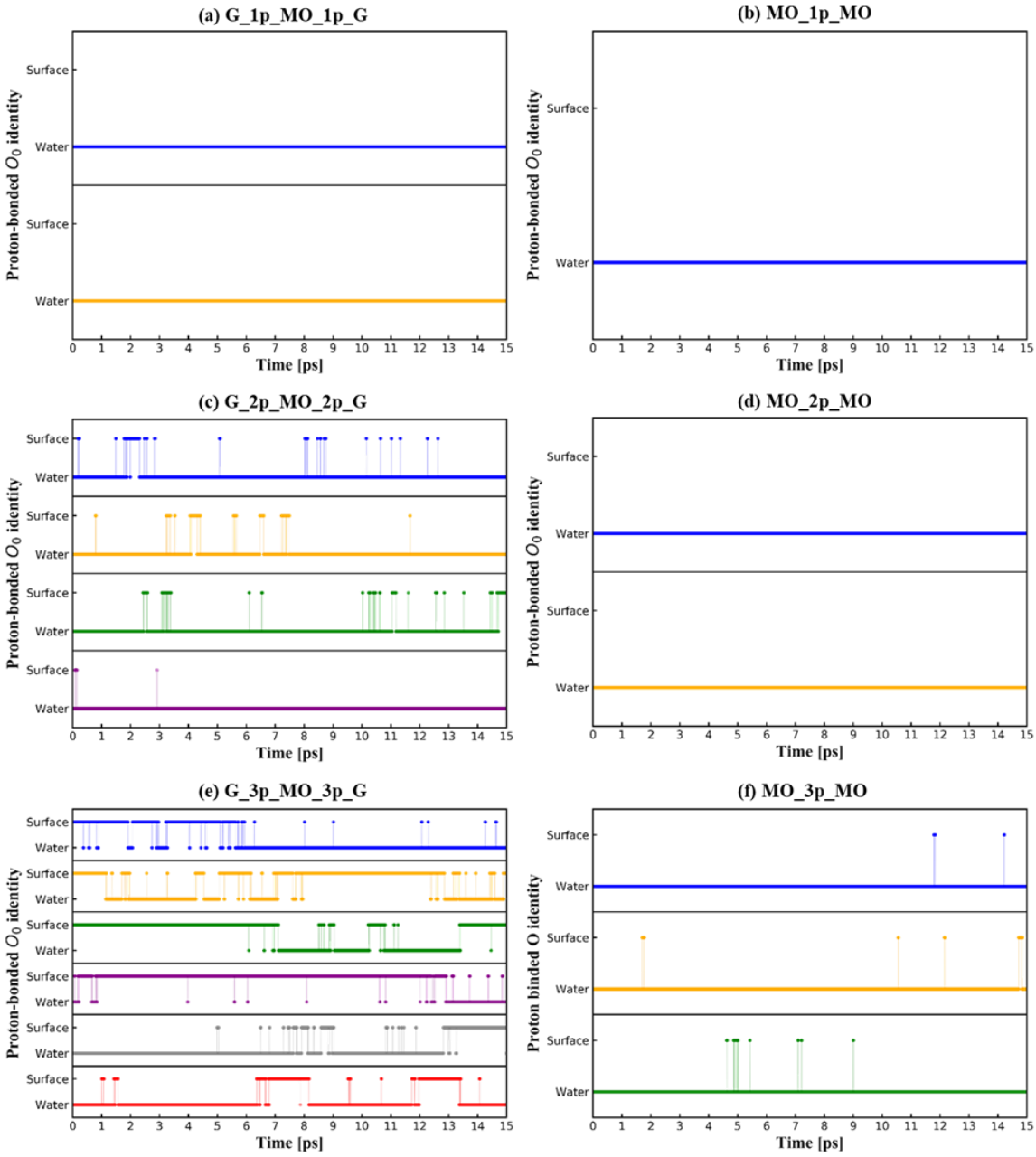

Figure 5.S9 The identity of the proton-bonded O_0 along trajectories for different **(a)**, **(c)**, **(e)** G_MO_Gs, and **(b)**, **(d)**, **(f)** MO_MOs. "Surface" in the y-axis denotes that the proton is bonding with a surface-O from MXene, while "water" represents that the proton is bonding with the O in a water molecule. Different color denotes different proton-bonded O_0.

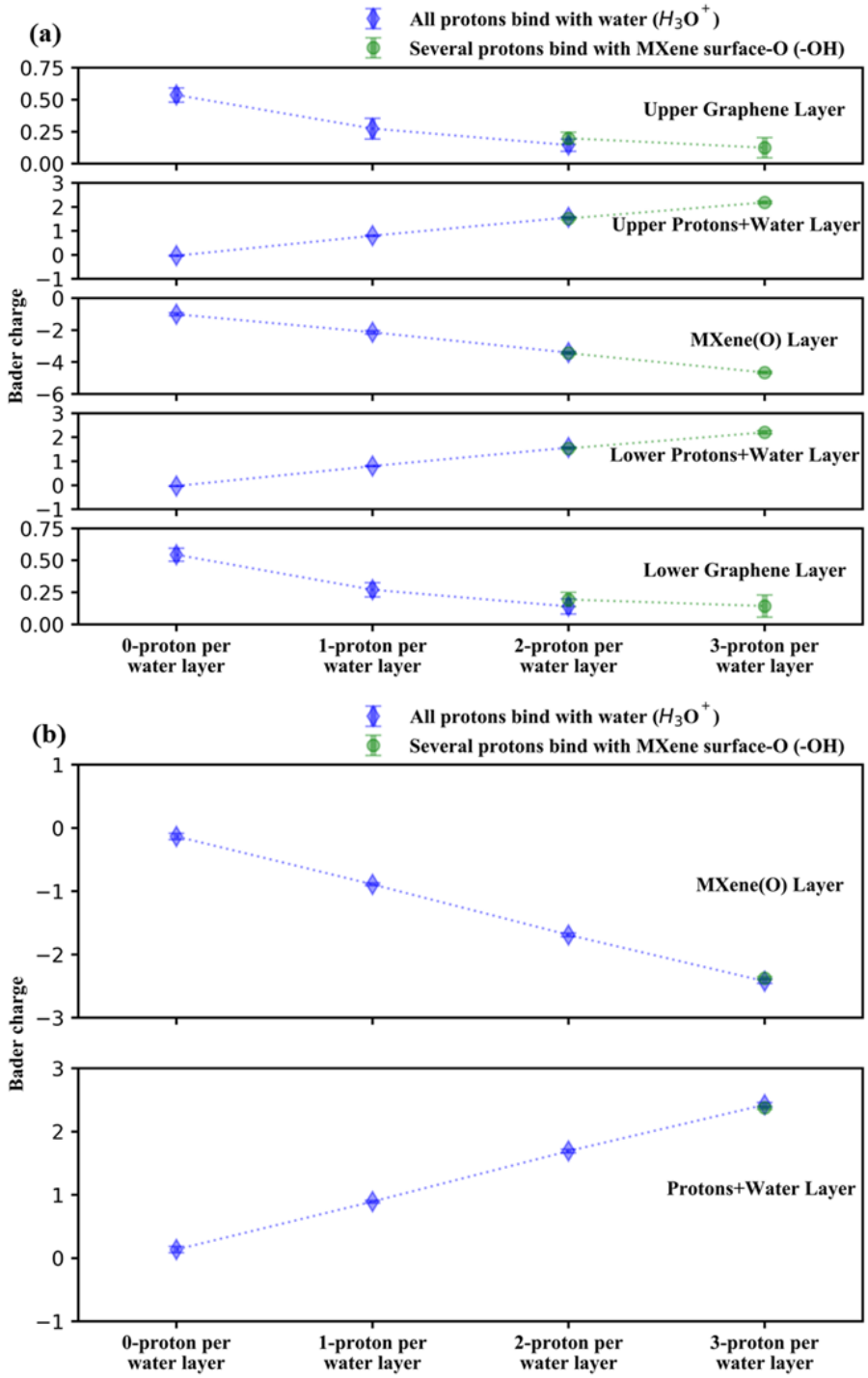

Figure 5.S10 The averaged bader charge per unit cell (from 10 randomly selected snapshots) of each building block in **(a)** G_MO_Gs, **(b)** MO_MOs for two different proton binding situations: "All protons bind with water (H_3O^+)" and "Several protons bind with MXene surface-O (-OH)". Note that the y-axis range is different for different building blocks. See Figure 5.1 for the names of different building blocks.

5.S12 Water intercalation of layered graphene-MXene heterostructure

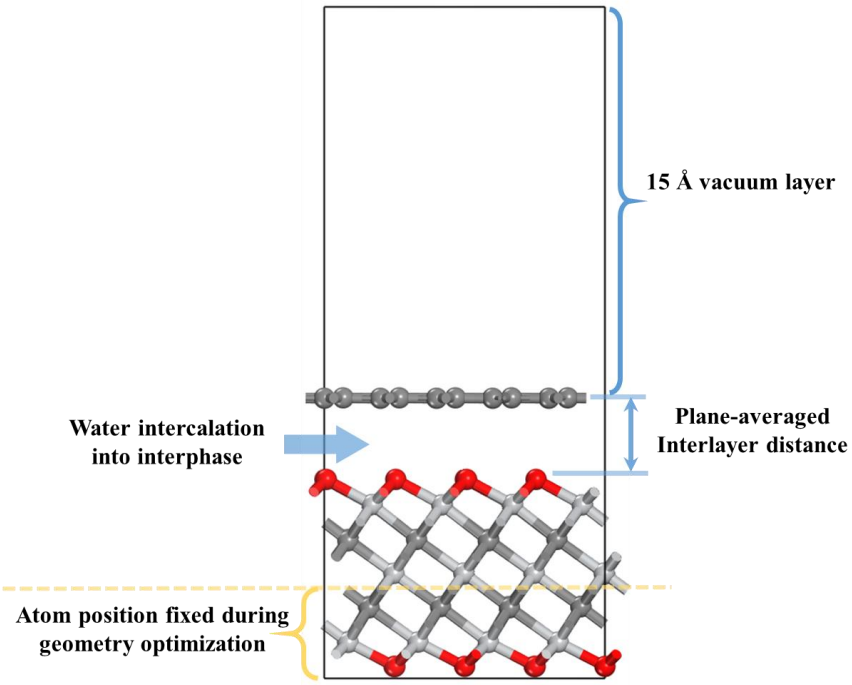

Figure 5.S11 A schematic of Graphene-MXene slab construction.

Before examining the proton dynamic behavior within the confined single water layer above, we explored the effect from the water-intercalation to the interfacial properties of the graphene-MXene system. The computational details are in common with that described in section 5.3 except for the building of the unit-cell. Here, we construct a slab (Figure 5S.11) that a 4×4 supercell of $Ti_3C_2O_2$ is matched to a 5×5 supercell of graphene with a lattice mismatch ~1.3%. A 15 Å vacuum layer is applied above the graphene layer to minimize the interaction due to the periodic images along Z-direction. During geometric optimization, the relaxation is only allowed to the graphene and the upper 4 atom-layers of MXene.

5.S12.1 Effects from water intercalation to interface distance

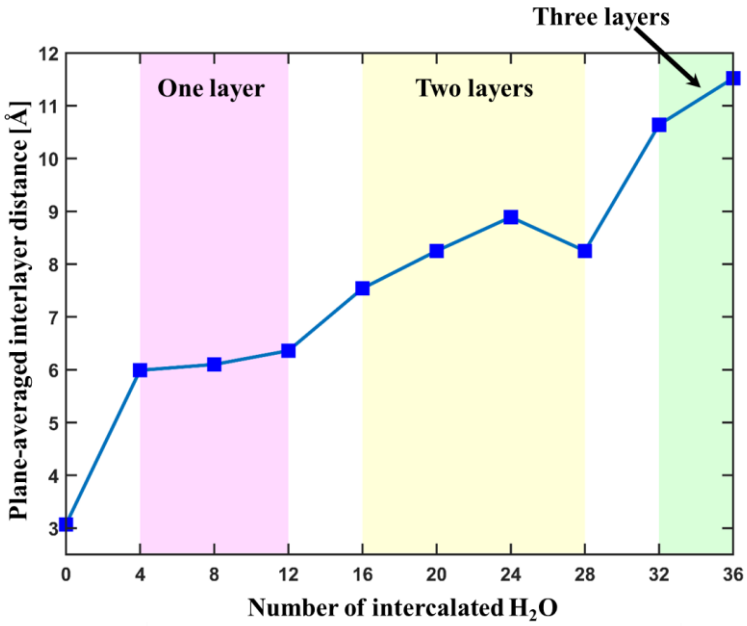

Figure 5.S12 Change in the plane-averaged interlayer distance between the graphene and its nearby surface-O from MXene as a function of the number of intercalated-H_2O molecules.

As the first step, we explore the effects of water intercalation on the interface distance. We estimate the number of molecules needed to form one, two or three water layers at interfaces through gradually introducing water molecules. With an incrementing number 4 each time from 0 to 36, we plotted the plane-averaged interlayer distance (Figure 5S.11) between the graphene and the nearby MXene surface-O layer as a function of the intercalated-H_2O number in Figure 5S.12. The corresponding optimal slab configurations are provided in Figure 5S.13. We found that the single water layer can contain up to 12 H_2O molecules. Further increase in the number of H_2O results in the onset of the second layer formation. Afterwards, the third water layer can be obtained when reaching 32 H_2O molecules. (The exact plane-averaged interlayer distances and the corresponding water

densities are summarized in Table 5.S3.) What is even more interesting is that the OH bond in water prefers to point toward MXene surface, especially for mono-layer water cases (4 to 12 intercalated H_2O). This phenomenon should be ascribed to the interfacial properties within the graphene-MXene heterostructure.

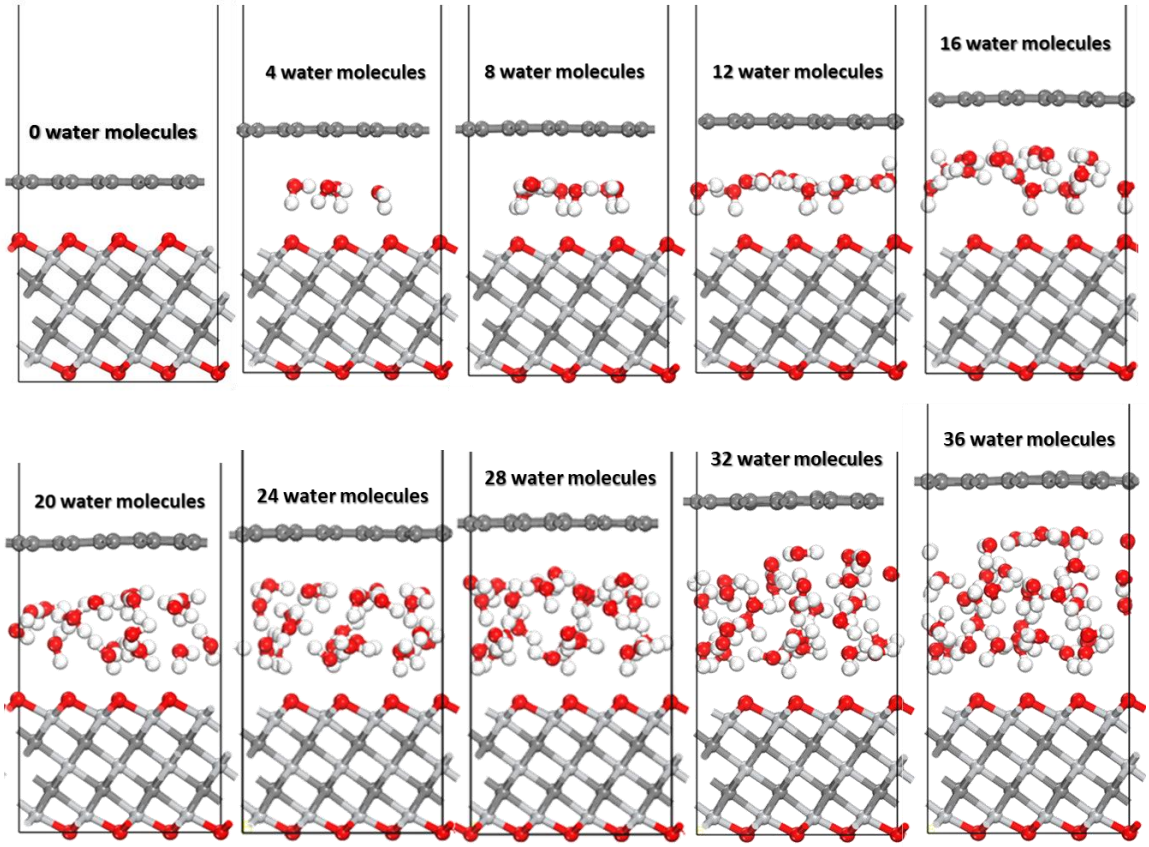

Figure 5.S13 The optimal slab configurations for the different number of intercalated H_2O systems.

Table 5.S3 The plane-averaged interlayer distances and the corresponding water densities for different systems with different intercalated-H_2O numbers.

	Number of intercalated-H_2O									
	0	4	8	12	16	20	24	28	32	36
Plane-averged interlayer distance [Å]	3.07	5.99	6.10	6.36	7.54	8.25	8.89	8.25	10.64	11.52
Water density [g/cm^3]	-	0.32	0.61	0.84	0.83	0.89	0.96	1.25	0.98	0.99

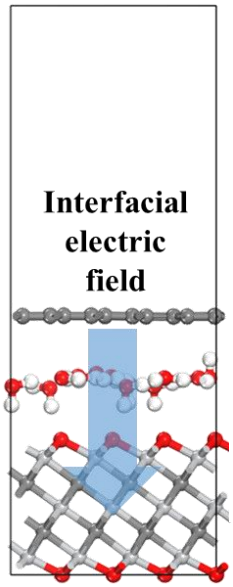

Table 5.S4 The bader charge per unit cell of different building blocks for different intercalated-H_2O number systems. The left plot shows the interfacial electric field with the direction from graphene to MXene.

Bader charge per unit cell	Number of intercalated H_2O									
	0	4	8	12	16	20	24	28	32	36
Graphene	0.60	0.54	0.69	0.61	0.62	0.64	0.46	0.70	0.66	0.83
Protons+Water Layer	0	-0.04	-0.08	-0.06	-0.07	-0.05	-0.02	-0.05	-0.05	-0.07
MXene	-0.60	-0.50	-0.61	-0.55	-0.55	-0.59	-0.44	-0.65	-0.61	-0.76

5.S12.2 Interfacial electronic properties with different intercalated-H_2O numbers

We carried out bader charge analysis of different building blocks (graphene, water layer, MXene) for the systems with different H_2O-intercalation numbers. The result has been tabulated into Table 5.S4. The appearance of the water molecules does not influence electron transfer from graphene to MXene ($Ti_3C_2O_2$), and a slight amount of the electrons (about 10%) will be transferred to the water layer no matter the H_2O-intercalation numbers. Hence, the interfacial electric field still exists. Those interfacial properties help to attract the water molecules and align the inner OH bonds.

5.S12.3 Interfacial H-bonding configurations

Since the -O surface terminations for MXene are used in this heterostructure study, there are mainly two types of H-bonding involved within interfaces. One is the H-bonding within water layer, the other is between the water layer and the MXene surface-O (Figure 5S.14). Those multiple interfacial H-bonding provide opportunities for protons to transfer within the hydrogen-bonded network and make the proton surface redox processes possible. Therefore, we explored the proton transport/dynamics at the beginning of Chapter 5.

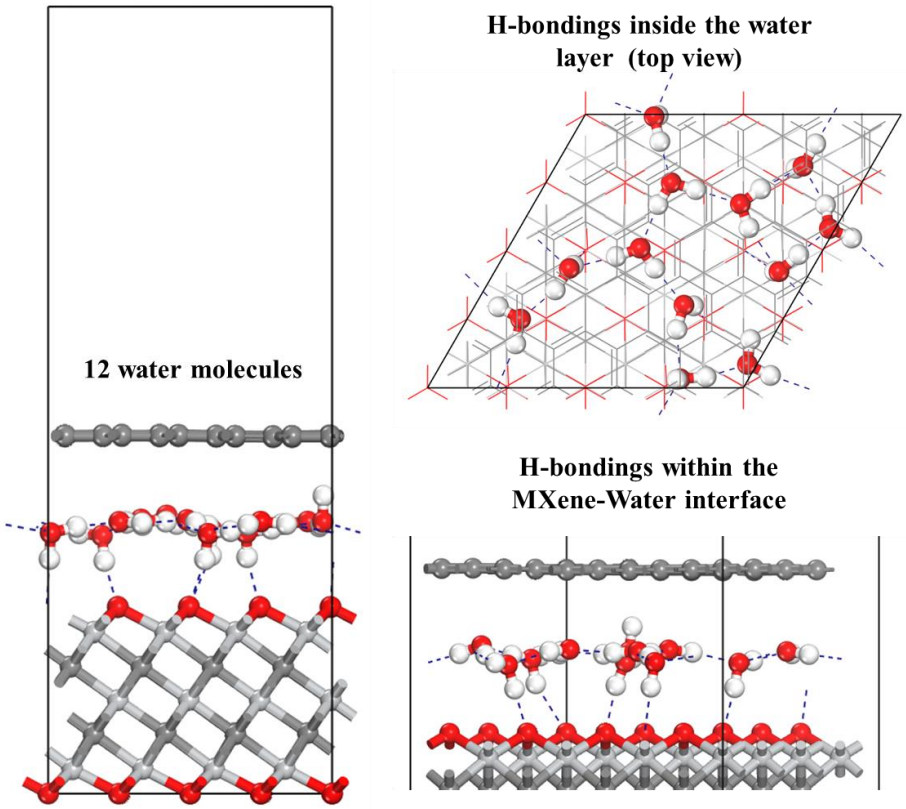

Figure 5.S14 Two types of H-bonding within interfaces using the 12 intercalated-H_2O system as an example. The dark blue dashed lines denote the H-bonding.

5.S13 Abbreviations

AIMD	*Ab initio* molecular dynamics
2D	Two-dimensional
PAN	Polyaniline
rGO	reduced graphene oxide
DFT	Density functional theory
TMO	Transition metal oxide
vDW	van der Waals

NVT	canonical ensemble
MSD	Mean square displacement
RDF	Radial distribution function
2D	Two-dimensional
1D	One-dimensional

References

(1) Naguib, M.; Kurtoglu, M.; Presser, V.; Lu, J.; Niu, J.; Heon, M.; Hultman, L.; Gogotsi, Y.; Barsoum, M. W. Two-dimensional Nanocrystals Produced by Exfoliation of Ti3AlC2. *Advanced materials* **2011**, *23* (37), 4248–4253. https://doi.org/10.1002/adma.201102306.

(2) Butler, S. Z.; Hollen, S. M.; Cao, L.; Cui, Y.; Gupta, J. A.; Gutiérrez, H. R.; Heinz, T. F.; Hong, S. S.; Huang, J.; Ismach, A. F. Progress, Challenges, and Opportunities in Two-Dimensional Materials beyond Graphene. *ACS nano* **2013**, *7* (4), 2898–2926. https://doi.org/10.1021/nn400280c.

(3) Xu, S.; Dall'Agnese, Y.; Li, J.; Gogotsi, Y.; Han, W. Thermally Reduced Graphene/MXene Film for Enhanced Li-ion Storage. *Chemistry–A European Journal* **2018**, *24* (69), 18556–18563. https://doi.org/10.1002/chem.201805162.

(4) Liang, X.; Garsuch, A.; Nazar, L. F. Sulfur Cathodes Based on Conductive MXene Nanosheets for High-performance Lithium–Sulfur Batteries. *Angewandte Chemie International Edition* **2015**, *54* (13), 3907–3911. https://doi.org/10.1002/anie.201410174.

(5) Li, H.; Hou, Y.; Wang, F.; Lohe, M. R.; Zhuang, X.; Niu, L.; Feng, X. Flexible All-solid-state Supercapacitors with High Volumetric Capacitances Boosted by Solution Processable MXene and Electrochemically Exfoliated Graphene. *Advanced Energy Materials* **2017**, *7* (4), 1601847. https://doi.org/10.1002/aenm.201601847.

(6) Yan, J.; Ren, C. E.; Maleski, K.; Hatter, C. B.; Anasori, B.; Urbankowski, P.; Sarycheva, A.; Gogotsi, Y. Flexible MXene/Graphene Films for Ultrafast Supercapacitors with Outstanding Volumetric Capacitance. *Advanced Functional Materials* **2017**, *27* (30), 1701264. https://doi.org/10.1002/adfm.201701264.

(7) Ahmed, B.; Anjum, D. H.; Hedhili, M. N.; Gogotsi, Y.; Alshareef, H. N. H_2O_2 Assisted Room Temperature Oxidation of Ti_2C MXene for Li-Ion Battery Anodes. *Nanoscale* **2016**, *8* (14), 7580–7587. https://doi.org/10.1039/C6NR00002A.

(8) Ding, L.; Wei, Y.; Wang, Y.; Chen, H.; Caro, J.; Wang, H. A Two-dimensional Lamellar Membrane: MXene Nanosheet Stacks. *Angewandte Chemie International Edition* **2017**, *56* (7), 1825–1829. https://doi.org/10.1002/anie.201609306.

(9) Ding, L.; Wei, Y.; Li, L.; Zhang, T.; Wang, H.; Xue, J.; Ding, L.-X.; Wang, S.; Caro, J.; Gogotsi, Y. MXene Molecular Sieving Membranes for Highly Efficient Gas Separation. *Nature communications* **2018**, *9* (1), 1–7. https://doi.org/10.1038/s41467-017-02529-6.

(10) Lei, Y.; Zhao, W.; Zhang, Y.; Jiang, Q.; He, J.-H.; Baeumner, A. J.; Wolfbeis, O. S.; Wang, Z. L.; Salama, K. N.; Alshareef, H. N. A MXene-Based Wearable Biosensor System for High-Performance In Vitro Perspiration Analysis. *Small* **2019**, *15* (19), 1901190. https://doi.org/10.1002/smll.201901190.

(11) Anasori, B.; Shi, C.; Moon, E. J.; Xie, Y.; Voigt, C. A.; Kent, P. R.; May, S. J.; Billinge, S. J.; Barsoum, M. W.; Gogotsi, Y. Control of Electronic Properties of 2D Carbides (MXenes) by Manipulating Their Transition Metal Layers. *Nanoscale Horizons* **2016**, *1* (3), 227–234. https://doi.org/10.1039/C5NH00125K.

(12) Tang, Q.; Zhou, Z.; Shen, P. Are MXenes Promising Anode Materials for Li Ion Batteries? Computational Studies on Electronic Properties and Li Storage Capability of Ti_3C_2 and $Ti_3C_2X_2$ (X= F, OH) Monolayer. *Journal of the American Chemical Society* **2012**, *134* (40), 16909–16916. https://doi.org/10.1021/ja308463r.

(13) Wang, K.; Lou, Z.; Wang, L.; Zhao, L.; Zhao, S.; Wang, D.; Han, W.; Jiang, K.; Shen, G. Bioinspired Interlocked Structure-Induced High Deformability for Two-Dimensional Titanium Carbide (MXene)/Natural Microcapsule-Based Flexible Pressure Sensors. *ACS Nano* **2019**, *13* (8), 9139–9147. https://doi.org/10.1021/acsnano.9b03454.

(14) Muckley, E. S.; Naguib, M.; Wang, H.-W.; Vlcek, L.; Osti, N. C.; Sacci, R. L.; Sang, X.; Unocic, R. R.; Xie, Y.; Tyagi, M. Multimodality of Structural, Electrical, and Gravimetric Responses of Intercalated MXenes to Water. *ACS nano* **2017**, *11* (11), 11118–11126. https://dx.doi.org/10.1021/acsnano.7b05264.

(15) Wu, L.; Lu, X.; Wu, Z.-S.; Dong, Y.; Wang, X.; Zheng, S.; Chen, J. 2D Transition Metal Carbide MXene as a Robust Biosensing Platform for Enzyme Immobilization and Ultrasensitive Detection of Phenol. *Biosensors and Bioelectronics* **2018**, *107*, 69–75. https://doi.org/10.1016/j.bios.2018.02.021.

(16) Rasheed, P. A.; Pandey, R. P.; Rasool, K.; Mahmoud, K. A. Ultra-Sensitive Electrocatalytic Detection of Bromate in Drinking Water Based on Nafion/$Ti_3C_2T_x$ (MXene) Modified Glassy Carbon Electrode. *Sensors and Actuators B: Chemical* **2018**, *265*, 652–659. https://doi.org/10.1016/j.snb.2018.03.103.

(17) Shi, X.; Wang, H.; Xie, X.; Xue, Q.; Zhang, J.; Kang, S.; Wang, C.; Liang, J.; Chen, Y. Bioinspired Ultrasensitive and Stretchable MXene-Based Strain Sensor via Nacre-Mimetic Microscale "Brick-and-Mortar" Architecture. *ACS Nano* **2019**, *13* (1), 649–659. https://doi.org/10.1021/acsnano.8b07805.

(18) Wang, F.; Yang, C.; Duan, M.; Tang, Y.; Zhu, J. TiO_2 Nanoparticle Modified Organ-like Ti_3C_2 MXene Nanocomposite Encapsulating Hemoglobin for a Mediator-Free Biosensor with Excellent Performances. *Biosensors and Bioelectronics* **2015**, *74*, 1022–1028. https://doi.org/10.1016/j.bios.2015.08.004.

(19) Seh, Z. W.; Fredrickson, K. D.; Anasori, B.; Kibsgaard, J.; Strickler, A. L.; Lukatskaya, M. R.; Gogotsi, Y.; Jaramillo, T. F.; Vojvodic, A. Two-Dimensional Molybdenum Carbide (MXene) as an Efficient Electrocatalyst for Hydrogen Evolution. *ACS Energy Letters* **2016**, *1* (3), 589–594. https://doi.org/10.1021/acsenergylett.6b00247.

(20) Zhou, S.; Yang, X.; Pei, W.; Liu, N.; Zhao, J. Heterostructures of MXenes and N-Doped Graphene as Highly Active Bifunctional Electrocatalysts. *Nanoscale* **2018**, *10* (23), 10876–10883. https://doi.org/10.1039/C8NR01090K.

(21) Liu, Y.; Luo, R.; Li, Y.; Qi, J.; Wang, C.; Li, J.; Sun, X.; Wang, L. Sandwich-like Co_3O_4/MXene Composite with Enhanced Catalytic Performance for Bisphenol A Degradation. *Chemical Engineering Journal* **2018**, *347*, 731–740. https://doi.org/10.1016/j.cej.2018.04.155.

(22) Zhang, H.; Li, M.; Cao, J.; Tang, Q.; Kang, P.; Zhu, C.; Ma, M. 2D A-Fe_2O_3 Doped Ti_3C_2 MXene Composite with Enhanced Visible Light Photocatalytic Activity for Degradation of Rhodamine B. *Ceramics International* **2018**, *44* (16), 19958–19962. https://doi.org/10.1016/j.ceramint.2018.07.262.

(23) Hu, M.; Cui, C.; Shi, C.; Wu, Z.-S.; Yang, J.; Cheng, R.; Guang, T.; Wang, H.; Lu, H.; Wang, X. High-Energy-Density Hydrogen-Ion-Rocking-Chair Hybrid Supercapacitors Based on $Ti_3C_2T_x$ MXene and Carbon Nanotubes Mediated by Redox Active Molecule. *ACS nano* **2019**, *13* (6), 6899–6905. http://dx.doi.org/10.1021/acsnano.9b01762.

(24) Lukatskaya, M. R.; Bak, S.-M.; Yu, X.; Yang, X.-Q.; Barsoum, M. W.; Gogotsi, Y. Probing the Mechanism of High Capacitance in 2D Titanium Carbide Using in Situ

X-ray Absorption Spectroscopy. *Advanced Energy Materials* **2015**, *5* (15), 1500589. https://doi.org/10.1002/aenm.201500589.

(25) Lukatskaya, M. R.; Kota, S.; Lin, Z.; Zhao, M.-Q.; Shpigel, N.; Levi, M. D.; Halim, J.; Taberna, P.-L.; Barsoum, M. W.; Simon, P. Ultra-High-Rate Pseudocapacitive Energy Storage in Two-Dimensional Transition Metal Carbides. *Nature Energy* **2017**, *2* (8), 17105. https://doi.org/10.1038/nenergy.2017.105.

(26) Hu, M.; Li, Z.; Hu, T.; Zhu, S.; Zhang, C.; Wang, X. High-Capacitance Mechanism for $Ti_3C_2T_x$ MXene by in Situ Electrochemical Raman Spectroscopy Investigation. *ACS nano* **2016**, *10* (12), 11344–11350. https://dx.doi.org/10.1021/acsnano.6b06597.

(27) Sun, Y.; Zhan, C.; Kent, P. R. C.; Naguib, M.; Gogotsi, Y.; Jiang, D. Proton Redox and Transport in MXene-Confined Water. *ACS Appl. Mater. Interfaces* **2020**, *12* (1), 763–770. https://doi.org/10.1021/acsami.9b18139.

(28) Wu, S.; Wang, H.; Li, L.; Guo, M.; Qi, Z.; Zhang, Q.; Zhou, Y. Intercalated MXene-Based Layered Composites: Preparation and Application. *Chinese Chemical Letters* **2020**, *31* (4), 961–968. https://doi.org/10.1016/j.cclet.2020.02.046.

(29) Pomerantseva, E.; Gogotsi, Y. Two-Dimensional Heterostructures for Energy Storage. *Nature Energy* **2017**, *2* (7), 1–6. https://doi.org/10.1038/nenergy.2017.89.

(30) Novoselov, K. S.; Mishchenko, A.; Carvalho, A.; Neto, A. C. 2D Materials and van Der Waals Heterostructures. *Science* **2016**, *353* (6298), aac9439. https://doi.org/10.1126/science.aac9439.

(31) Geim, A. K.; Grigorieva, I. V. Van Der Waals Heterostructures. *Nature* **2013**, *499* (7459), 419–425. https://doi.org/10.1038/nature12385.

(32) Xu, S.; Wei, G.; Li, J.; Han, W.; Gogotsi, Y. Flexible MXene–Graphene Electrodes with High Volumetric Capacitance for Integrated Co-Cathode Energy Conversion/Storage Devices. *J. Mater. Chem. A* **2017**, *5* (33), 17442–17451. https://doi.org/10.1039/C7TA05721K.

(33) Yang, Q.; Xu, Z.; Fang, B.; Huang, T.; Cai, S.; Chen, H.; Liu, Y.; Gopalsamy, K.; Gao, W.; Gao, C. MXene/Graphene Hybrid Fibers for High Performance Flexible Supercapacitors. *J. Mater. Chem. A* **2017**, *5* (42), 22113–22119. https://doi.org/10.1039/C7TA07999K.

(34) Aïssa, B.; Ali, A.; Mahmoud, K. A.; Haddad, T.; Nedil, M. Transport Properties of a Highly Conductive 2D $Ti_3C_2T_x$ MXene/Graphene Composite. *Appl. Phys. Lett.* **2016**, *109* (4), 043109. https://doi.org/10.1063/1.4960155.

(35) Fu, J.; Yun, J.; Wu, S.; Li, L.; Yu, L.; Kim, K. H. Architecturally Robust Graphene-Encapsulated MXene Ti_2CT_x@Polyaniline Composite for High-Performance Pouch-Type Asymmetric Supercapacitor. *ACS Appl. Mater. Interfaces* **2018**, *10* (40), 34212–34221. https://doi.org/10.1021/acsami.8b10195.

(36) Gan, L.-Y.; Zhao, Y.-J.; Huang, D.; Schwingenschlögl, U. First-Principles Analysis of MoS_2/Ti_2C and MoS_2/Ti_2CY_2 (Y=F and OH) All-2D Semiconductor/Metal Contacts. *Phys. Rev. B* **2013**, *87* (24), 245307. https://doi.org/10.1103/PhysRevB.87.245307.

(37) Du, Y.-T.; Kan, X.; Yang, F.; Gan, L.-Y.; Schwingenschlögl, U. MXene/Graphene Heterostructures as High-Performance Electrodes for Li-Ion Batteries. *ACS Appl. Mater. Interfaces* **2018**, *10* (38), 32867–32873. https://doi.org/10.1021/acsami.8b10729.

(38) Li, R.; Sun, W.; Zhan, C.; Kent, P. R. C.; Jiang, D. Interfacial and Electronic Properties of Heterostructures of MXene and Graphene. *Phys. Rev. B* **2019**, *99* (8), 085429. https://doi.org/10.1103/PhysRevB.99.085429.

(39) Zhong, C.; Deng, Y.; Hu, W.; Qiao, J.; Zhang, L.; Zhang, J. A Review of Electrolyte Materials and Compositions for Electrochemical Supercapacitors. *Chem. Soc. Rev.* **2015**, *44* (21), 7484–7539. https://doi.org/10.1039/C5CS00303B.

(40) Kresse, G.; Furthmüller, J. Efficiency of *Ab-Initio* Total Energy Calculations for Metals and Semiconductors Using a Plane-Wave Basis Set. *Computational Materials Science* **1996**, *6* (1), 15–50. https://doi.org/10.1016/0927-0256(96)00008-0.

(41) Kresse, G.; Furthmüller, J. Efficient Iterative Schemes for *Ab Initio* Total-Energy Calculations Using a Plane-Wave Basis Set. *Phys. Rev. B* **1996**, *54* (16), 11169–11186. https://doi.org/10.1103/PhysRevB.54.11169.

(42) Blöchl, P. E. Projector Augmented-Wave Method. *Phys. Rev. B* **1994**, *50* (24), 17953–17979. https://doi.org/10.1103/PhysRevB.50.17953.

(43) Kresse, G.; Joubert, D. From Ultrasoft Pseudopotentials to the Projector Augmented-Wave Method. *Phys. Rev. B* **1999**, *59* (3), 1758–1775. https://doi.org/10.1103/PhysRevB.59.1758.

(44) Perdew, J. P.; Burke, K.; Ernzerhof, M. Generalized Gradient Approximation Made Simple. *Phys. Rev. Lett.* **1996**, *77* (18), 3865–3868. https://doi.org/10.1103/PhysRevLett.77.3865.

(45) Grimme, S.; Ehrlich, S.; Goerigk, L. Effect of the Damping Function in Dispersion Corrected Density Functional Theory. *Journal of computational chemistry* **2011**, *32* (7), 1456–1465. https://doi.org/10.1002/jcc.21759.

(46) Grimme, S.; Antony, J.; Ehrlich, S.; Krieg, H. A Consistent and Accurate *Ab Initio* Parametrization of Density Functional Dispersion Correction (DFT-D) for the 94 Elements H-Pu. *The Journal of chemical physics* **2010**, *132* (15), 154104. https://doi.org/10.1063/1.3382344.

(47) Becke, A. D.; Johnson, E. R. A Density-Functional Model of the Dispersion Interaction. *The Journal of chemical physics* **2005**, *123* (15), 154101. https://doi.org/10.1063/1.2065267.

(48) Monkhorst, H. J.; Pack, J. D. Special Points for Brillouin-Zone Integrations. *Phys. Rev. B* **1976**, *13* (12), 5188–5192. https://doi.org/10.1103/PhysRevB.13.5188.

(49) Nosé, S. A Unified Formulation of the Constant Temperature Molecular Dynamics Methods. *The Journal of chemical physics* **1984**, *81* (1), 511–519. https://doi.org/10.1063/1.447334.

(50) Shuichi, N. Constant Temperature Molecular Dynamics Methods. *Progress of Theoretical Physics Supplement* **1991**, *103*, 1–46. https://doi.org/10.1143/PTPS.103.1.

(51) Bylander, D. M.; Kleinman, L. Energy Fluctuations Induced by the Nosé Thermostat. *Physical Review B* **1992**, *46* (21), 13756. http://dx.doi.org/10.1103/PhysRevB.46.13756

(52) Zhan, C.; Lian, C.; Zhang, Y.; Thompson, M. W.; Xie, Y.; Wu, J.; Kent, P. R. C.; Cummings, P. T.; Jiang, D.; Wesolowski, D. J. Computational Insights into Materials and Interfaces for Capacitive Energy Storage. *Advanced Science* **2017**, *4* (7), 1700059. https://doi.org/10.1002/advs.201700059.

Chapter 6

Conclusions

In this dissertation, the first-principles methodologies were employed to explore material properties and proton transport of various 2-dimensional (2D) MXene-based composites and transition metal oxides (TMO). Through our investigations, we address two significant issues or challenges the energy storage materials may confront: (1) Finding potential electrode materials with outstanding material properties to achieve the goal of both high energy density and high power density; (2) Probing fundamental understandings on electrolyte transport within complexed systems to better analyze the rationales behind.

Chapter 3-4 illustrate the electric, geometric, and energetic properties of various transition metal oxides (TMO) or complex MXene-based composites using density

functional theory (DFT) approaches. To understand hydrogen in various transition metal perovskites ABO_3, we calculated the hydrogen absorption energy (HAE). We further found that the ICOHP of B-O bond (from bonding analysis) was a useful chemical descriptor that correlates with HAE. The weaker the strength of the B-O bonding, the more reactive the oxygen will be toward hydrogen. The low potential barriers of H diffusion processes make hydrogen migrations within different O-sites in bulk perovskites possible. Our work helps to provide further perceptions for future studies on hydrogen intercalation and transport within perovskites. For the MXene-based composites, we mainly discover the interfacial properties of MXene/anatase TiO_2(101) heterostructures. By tuning the MXene surface functional group, the interfacial adhesion energy will differ. Meanwhile, the amount of the interfacial electron transfer will change dramatically, leading to an induced interfacial electric field. Through doping TiO_2 with N element or changing MXene terminated group, the electrical properties change from a semiconductor (Ti_2CO_2/TiO_2) to a conductor ($Ti_2CF_{0.2}O_{1.8}/TiO_2$ or $Ti_2CO_2/(N)TiO_2$). The geometric changes due to N doping will be our future research direction.

In Chapter 5, we carried on comprehensive studies on water and proton intercalations in two different confined interfaces, $Ti_3C_2O_2$-$Ti_3C_2O_2$, and graphene-$Ti_3C_2O_2$. We explore the proton transport mechanism within these interfaces in the acidic environment through *ab initio* molecular dynamic (AIMD) simulations. We found that the denser hydrogen-bonded network with directional water configurations (induced by the interfacial electric field) contributes to frequent proton surface redox and fast proton mobilities. The intercalated-proton concentration and repulsions will also influence the

proton transport and diffusion behavior. The comparison between the proton transport/diffusion behaviors within two different confined interfaces provides additional understandings on the energy storage mechanisms.

Appendix A

Home-made Computer Codes

This appendix contains several source Python3 codes used in Chapter 5. More codes can be found in my Github (https://github.com/LibbyXu/AIMD_DISS_CODING).

These codes can be applied to any cases that satisfy the following requirements:

i) VASP[1] outputs (Vienna *Ab initio* Simulation Package)

ii) Water molecules will not dissociate along the whole trajectories

iii) Protons and water molecules are the main interface medias

iv) The surfaces are mainly or partially covered by O terminations (the "partially" means that other terminated functional groups are inertia to the active media in ii).

To use these codes, we need the following operating environment, and some already installed packages:

i) LINUX operating systems

ii) Python 3 environment

iii) VTSTSCRIPTS-933[2,3] package (We will call some functions from this package during our coding analysis. The path to the executables should be written into the environmental variables.)

A.1 Proton bonded O_0 trajectory

The labeled O_0 has already been illustrated in Chapter 5. From the following codes, you will obtain the proton bonded O_0 paths as well as its surrounding H-atom positions– three H atoms for the hydronium ion (H_3O^+) and only one H atom for the hydroxyl group (-OH) on MXene surfaces. We type the following command: "./**Pro_O_coores_H.sh**"

Pro_O_coores_H.sh:

```
1. ############################################################
2. ############Obtaining info about proton-bonded O############
3. ############################################################
4.
5. ############Needed input files############
6. ############i)POSCAR#####################
7. ############ii)XDATCAR####################
8.
9. ########################################
10. ##########Setting parameters##########
11. ########################################
12. #####Number of the protons#####
13. total_proton_num=`echo 2`  #You can modify
14.
15. #####O indexes on Surface#####
16. ###If indexes have order
```

```
Sur_O_St=`echo 33`  #You can modify
Sur_O_En=`echo 64`  #You can modify
interger_SO=`echo 1`  #You can modify
echo "${Sur_O_St}" >> index_SO_temp
for ((i=${Sur_O_St}+${interger_SO}; i<=${Sur_O_En}; i+=${interger_SO}))
do
  echo ",$i" >> index_SO_temp
done
cat index_SO_temp | xargs > index_SO
SO_temp=(`echo $(grep "," index_SO)`)
SurfaceO=`echo ${SO_temp[@]} | sed 's/ //g'`
rm index_SO index_SO_temp
###If indexes do not have an order
#SurfaceO=(83,89,91,97,99,101,109,111,113)  #You can modify

#####O indexes in water#####
###If indexes have order
Wat_O_St=`echo 65`   #You can modify
Wat_O_En=`echo 76`   #You can modify
interger_WO=`echo 1`  #You can modify
echo "${Wat_O_St}" >> index_WO_temp
for ((i=${Wat_O_St}+${interger_WO}; i<=${Wat_O_En}; i+=${interger_WO}))   #
i+
do
  echo ",$i" >> index_WO_temp
done
cat index_WO_temp | xargs > index_WO
WO_temp=(`echo $(grep "," index_WO)`)
WaterO=`echo ${WO_temp[@]} | sed 's/ //g'`
rm index_WO index_WO_temp
###If indexes do not have an order
#WaterO=(115,117,121,122,123,126)  #You can modify

#####Initial index of Hydrogen (H)#####
First_H_index=`echo 125`  #You can modify

#####Total steps along trajectory (XDATCAR)#####
num_XDATCAR=`echo 15000`  #You can modify

#####Total number of water molecules#####
num_water=`echo ${WaterO[0]} | awk -F "," '{print NF}'`

#####Last index of Hydrogen (H)######
Final_H_index=`echo ${First_H_index}'+'2'*'${num_water}'+'${total_proton_nu
m}'-'1 | bc`


#####################################
##########Python codes lists##########
#####################################

########################
```

```
###Python_one.py code###
########################
#############################################################################
###Sorted the distance between the O (Surface or Water) to the same H###
#############################################################################
cat << EOF > Python_one.py

import numpy as np
import math

#Define water-O and surface-O indexes
Surface_O_index=[${SurfaceO[@]}]
Water_O_index=[${WaterO[@]}]
#Load data
data_H_temp_list = np.genfromtxt('H_temp_list', delimiter='')

index_order = data_H_temp_list[:,0]
atom_index_distance = data_H_temp_list[:,1:3]
atom_index_position = data_H_temp_list[:,3:7]
len_step = len(index_order)
#The distance from 2nd-
end rows are between the atom in that row and the 1st row--H position
H_corres_index = atom_index_distance[0,0]
H_corres_position = atom_index_position[0,:]

#Obtain the nearest O atom to the H
#O identity: surface-O: 0, water-O: 1
ii = 0
Two_O_connected = np.zeros(shape=((len_step-1),7))


for i in range(1,len_step):
    temp_one = int(atom_index_distance[i,0])
    if temp_one in Surface_O_index:
            Two_O_connected[ii,0] = H_corres_index
            Two_O_connected[ii,1:3] = atom_index_distance[i,:]
            Two_O_connected[ii,3:6] = atom_index_position[i,:]
            Two_O_connected[ii,6] = 0
            ii = ii+1
       elif temp_one in Water_O_index:
            Two_O_connected[ii,0] = H_corres_index
            Two_O_connected[ii,1:3] = atom_index_distance[i,:]
            Two_O_connected[ii,3:6] = atom_index_position[i,:]
            Two_O_connected[ii,6] = 1
            ii = ii+1

   #Format for Two_O_connected
   #H index, O index, O-H distance, O X-coord, O Y-coord, O Z-
coord, O identity

   #Save datafile
   np.savetxt("near_O_list", Two_O_connected, fmt="%s", delimiter='   ')
```

```
117.
118.   EOF
119.   ##########################
120.   ###End of Python_one.py###
121.   ##########################
122.
123.
124.   ########################
125.   ###Python_two.py code###
126.   ########################
127.   ######################################################################
128.   ###Locate each H (water) and find the possible proton-like H###
129.   ######################################################################
130.   cat << EOF > Python_two.py
131.
132.   import numpy as np
133.   import math
134.
135.   #Define water-O and surface-O indexes
136.   Surface_O_index=[${SurfaceO[@]}]
137.   Water_O_index=[${WaterO[@]}]
138.   #Load data
139.   data_O_list = np.genfromtxt('Sorted_Two_O_list_current_step_final', deli
   miter='')
140.   iH_iO_dist = data_O_list[:, 0:3]
141.   H_position = data_O_list[:, 3:6]
142.   S_or_W_O = data_O_list[:, 6]
143.   length_file = len(S_or_W_O)
144.
145.   #H2O in water, -OH on surface, or others
146.   twoH_water_O = np.zeros(shape=(length_file,7))
147.   oneH_surf_O = np.zeros(shape=(length_file,7))
148.   OtherH_O = np.zeros(shape=(length_file,7))
149.   i_s = 0
150.   i_w = 0
151.   i_other = 0
152.
153.   for i in range(0,length_file):
154.       temp_O_index = int(iH_iO_dist[i,1])  #In comparison with the previou
   s one
155.       ###Surface-O
156.       if temp_O_index in Surface_O_index:
157.           oneH_surf_O[i_s,0:3] = iH_iO_dist[i,0:3]
158.           oneH_surf_O[i_s,3] = S_or_W_O[i]
159.           oneH_surf_O[i_s,4:7] = H_position[i,0:3]
160.           i_s = i_s+1
161.       ###Water-O
162.       elif temp_O_index in Water_O_index: #Water-O
163.           if (i-1) != -1: #i is not the first line
164.               temp_Oi = int(iH_iO_dist[(i-1),1])
165.               if temp_O_index != temp_Oi:
166.                   twoH_water_O[i_w,0:3] = iH_iO_dist[i,0:3]
```

```
                    twoH_water_O[i_w,3] = S_or_W_O[i]
                    twoH_water_O[i_w,4:7] = H_position[i,0:3]
                    i_w = i_w+1
                    num_wO = 1
                elif temp_O_index == temp_Oi:
                    if num_wO < 2:  #Grab two H that corresponding to the water-O
                        twoH_water_O[i_w,0:3] = iH_iO_dist[i,0:3]
                        twoH_water_O[i_w,3] = S_or_W_O[i]
                        twoH_water_O[i_w,4:7] = H_position[i,0:3]
                        i_w = i_w+1
                        num_wO = num_wO+1
                    elif num_wO >= 2:  #Others H
                        OtherH_O[i_other,0:3] = iH_iO_dist[i,0:3]
                        OtherH_O[i_other,3] = S_or_W_O[i]
                        OtherH_O[i_other,4:7] = H_position[i,0:3]
                        i_other = i_other+1
                        num_wO = num_wO+1
            elif (i-1) == -1:  #i is the first line
                twoH_water_O[i_w,0:3] = iH_iO_dist[i,0:3]
                twoH_water_O[i_w,3] = S_or_W_O[i]
                twoH_water_O[i_w,4:7] = H_position[i,0:3]
                i_w = i_w+1
                num_wO = 1

    #Delete all-0 rows
    oneH_surf_O_temp = np.delete(oneH_surf_O,[i for i in range(i_s,length_file)],0)
    OtherH_O_temp = np.delete(OtherH_O,[i for i in range(i_other,length_file)],0)
    twoH_water_O_temp = np.delete(twoH_water_O,[i for i in range(i_w,length_file)],0)

    #Possible proton-like index and positions
    surface_other_Combin = np.vstack((oneH_surf_O_temp,OtherH_O_temp))

    #Format for surface_other_Combin and twoH_water_O_temp
    #H Iindex, O index, H-O distance, O-identity surface-O(0)/water-O(1), O X-coord, O Y-coord, O Z-coord,

    #Save datafiles
    np.savetxt('Sur_Other_O_binding_H', surface_other_Combin, fmt="%s", delimiter='   ')
    np.savetxt('Water_O_binding_2H', twoH_water_O_temp, fmt="%s", delimiter='   ')

    EOF
    ############################
    ###End of Python_two.py###
    ############################
```

```
###########################
###Python_three.py code###
###########################
#############################################################################################
###########################################
###Finding all the proton-bonded O indexes and bonded H index (3 for H3O+/1 for -OH) as well as each O-H distance###
#############################################################################################
###########################################
cat << EOF > Python_three.py

import numpy as np
import math

#Define water-O and surface-O indexes
Surface_O_index=[${SurfaceO[@]}]
Water_O_index=[${WaterO[@]}]
proton_A=${total_proton_num}
Water_num = ${num_water}
First_H_fixed = ${First_H_index}
First_H = ${First_H_index}
#Load data
Water_O_Hd_data = np.genfromtxt('Water_O_Hd', delimiter='')
Water_O_Od_data = np.genfromtxt('Water_O_Od', delimiter='')
SaOther_O_data = np.genfromtxt('SaOther_O', delimiter='')
len_WH = len(Water_O_Hd_data[:,0])

#Finding the proton indexes first
lack_H_index = np.zeros(proton_A)

ii = 0
if len_WH == Water_num*2:
    for i in range(0,len_WH):
        if Water_O_Hd_data[i,0] == First_H:
            First_H = First_H + 1
        elif Water_O_Hd_data[i,0] != First_H:
            temp_nss=int(Water_O_Hd_data[i,0]-First_H)
            for iii in range(0,temp_nss):
                lack_H_index[ii] = First_H+iii
                ii = ii+1
            First_H = Water_O_Hd_data[i,0] + 1
    time_left = int((First_H_fixed+2*Water_num+proton_A-1) - Water_O_Hd_data[len_WH-1,0])
    if time_left <= proton_A and time_left > 0:
        for t in range(0,time_left):
            lack_H_index[(proton_A-time_left+t)] = First_H_fixed+2*Water_num+proton_A-time_left+t
elif len_WH != 2*Water_num:
    print('Problem! Water amount and 2*H amount are not match!')

#Finding the index and position for proton bonded O
```

```
len_other=len(SaOther_O_data[:,0])
Proton_O=np.zeros(proton_A)
Proton=np.zeros(proton_A)

for ww in range(0,len_other):
    Proton_temp = SaOther_O_data[ww,0]
    if Proton_temp in lack_H_index:
        start_st=ww
        break

Proton_temp_all=np.zeros(proton_A)
Proton_temp_all[0]=Proton_temp
Proton_O[0]=SaOther_O_data[start_st,1]
Proton[0]=SaOther_O_data[start_st,0]
right_sever_position=np.zeros(shape=(proton_A,7))
right_sever_position[0,:]=SaOther_O_data[start_st,:]
tem_num=start_st+1

for pp in range(1,proton_A):
    for yy in range(tem_num,len_other):
        Proton_t = SaOther_O_data[yy,0]
        if (Proton_t not in Proton_temp_all) and (Proton_t in lack_H_ind
ex) :
            Proton_O[pp]=SaOther_O_data[yy,1]
            Proton[pp]=SaOther_O_data[yy,0]
            Proton_temp_all[pp] = SaOther_O_data[yy,0]
            right_sever_position[pp,:]=SaOther_O_data[yy,:]
            tem_num=1+tem_num
            break

#Obtain the H index and position to proton-bonded O
#3H in H30+ in water molecules
#1H in -OH on surface, other 2H are empty
proton_writen_infile = np.zeros(shape=(proton_A*3,7))

iii = 0
if np.array_equal(lack_H_index,sorted(Proton)) == True:
    for aa in range(0,proton_A):
        temp_O_index = Proton_O[aa]
        proton_writen_infile[iii,:] = right_sever_position[aa,:]
        iii = iii + 1
        if temp_O_index in Water_O_index:
            for bb in range(0,len_WH):
                if Water_O_Od_data[bb,1] == temp_O_index:
                    proton_writen_infile[iii,:] = Water_O_Od_data[bb,:]

                    iii = iii + 1
        elif temp_O_index in Surface_O_index:
            for cc in range(0,2):
                proton_writen_infile[iii,:] = np.zeros(7)
                iii = iii + 1
elif np.array_equal(lack_H_index,sorted(Proton)) == False:
```

```
308.       print("Problem! Please recheck the proton indexes!")
309.
310.   #Format for H_and_corresponding_O:
311.   #3-row form a group and corresponds to the same proton-bonded O;
312.   #In each group, the first row is alwasy the proton related row
313.   #H Iindex, O index, H-O distance, O-identity surface-O(0)/water-
   O(1), O X-coord, O Y-coord, O Z-coord,
314.
315.   #Save datafile
316.   np.savetxt('H_and_corresponding_O', proton_writen_infile, fmt="%s", deli
   miter='    ')
317.
318.   EOF
319.   ############################
320.   ###End of Python_three.py###
321.   ############################
322.
323.
324.   ##########################################################################
   #
325.   ##########Linux commands used to connect different Python codes#########
   #
326.   ##########################################################################
   #
327.
328.   ########################################
329.   #####The two nearest O to the same H#####
330.   ########################################
331.   for ((s=1; s<=${num_XDATCAR}; s++))
332.   do
333.     ###Handle trajectory step by step
334.     xdat2pos.pl 1 $s  #xdat2pos.pl from VTSTSCRIPTS-
   933, the output is POSCAR$s.out
335.     mv POSCAR$s.out CONTCAR
336.
337.     ###Handling with all H indexes
338.     for ((a=${First_H_index}; a<=${Final_H_index}; a++))
339.     do
340.       neighbors.pl CONTCAR $a  #neighbors.pl from VTSTSCRIPTS-
   933, the output is neighdist.dat
341.       ###Format: index, atom_index, distace, X-coord, Y-coord, Z-coord
342.       awk '{printf("%4d %4d %15.8f %15.8f %15.8f %15.8f\n",$1, $2, $7, $3,
    $4, $5)}' neighdist.dat > H_temp_list
343.       sed -i '10,$d' H_temp_list
344.       ###Python3 environment
345.       python Python_one.py >> First_python.log
346.       sed '3,$d' near_O_list >> Two_O_list_current_step
347.       rm H_temp_list neighdist.dat near_O_list
348.     done
349.
350.     ###Format: index, atom_index, distace, X-coord, Y-coord, Z-
   coord, surface-O(0)/water-O(1)
```

```
    awk '{printf("%4d %4d %15.8f %15.8f %15.8f %15.8f %4d\n", $1, $2, $3, $4, $5, $6, $7)}' Two_O_list_current_step > Two_O_list_current_step_final

    ###Sorted firstly by O index and secondly by the H-O distance
    sort -n -k2 -k3 Two_O_list_current_step_final > Sorted_Two_O_list_current_step_final
    rm Two_O_list_current_step Two_O_list_current_step_final

  ######################################################################
  #####Locate each H (water) and find possible proton-like H######
  ######################################################################
    python Python_two.py >> Second_python.log

    ###Format: H Iindex, O index, H-O distance, O-identity surface-O(0)/water-O(1), O X-coord, O Y-coord, O Z-coord,
    awk '{printf("%4d %4d %15.8f %4d %15.8f %15.8f %15.8f\n", $1, $2, $3, $4, $5, $6, $7)}' Sur_Other_O_binding_H > Sur_Other_O_binding_H_temp
    awk '{printf("%4d %4d %15.8f %4d %15.8f %15.8f %15.8f\n", $1, $2, $3, $4, $5, $6, $7)}' Water_O_binding_2H > Water_O_Od  #Sorted by O index
    sort -n -k3 Sur_Other_O_binding_H_temp > SaOther_O  #Sorted by O index
    sort -n -k1 Water_O_Od > Water_O_Hd  #Sorted by H index
    rm Sur_Other_O_binding_H_temp Sur_Other_O_binding_H Water_O_binding_2H Sorted_Two_O_list_current_step_final

  ######################################################################
  #####Find proton-bonded O index, bonded H index, O-H distance#####
  ######################################################################
    python Python_three.py >> Third_python.log
    rm Water_O_Hd Water_O_Od SaOther_O

    numL_combine=`echo 3'*'${total_proton_num} | bc`
    #Format: Proton-bonded O index, O odentity surface-O(0)/water-O(1), bonded Proton/H index, H-O distance
    awk '{printf("%4d %4d %4d %12.8f\n", $2, $4, $1, $3)}' H_and_corresponding_O > Order_list
    #Combine same Proton-bonded O index into one row
    awk 'ORS=NR%'${numL_combine}'?"   ":"\n"{print}' Order_list >> final_H_list_temp
    rm H_and_corresponding_O Order_list CONTCAR
  done

  ##############################
  #####The final datafiles#####
  ##############################
  total_co=`echo 12`

  ###################################################
  ###With O identity surface-O(0)/water-O(1) list###

  #Format for with_proton_bonded_Oid_H_list
  #i) each row represents each step
```

```
392.   #ii) every 8-column have the information for same proton-bonded O
393.   #iii) 1st column: Proton-bonded O index
394.   #     2nd column: The identity of this O surface-O(0)/water-O(1)
395.   #     3-4th columns: proton index and O-H distance
396.   #     5-8th columns:
   The other 2H bonding with the O index (empty means surface O)
397.
398.   touch with_Proton_bonded_Oid_H_list
399.   for ((On=1; On<=${total_proton_num}; On++))
400.   do
401.     awk '{printf("%4d %2d\n",$('${total_co}'*('$On'-
   1)+1),$('${total_co}'*('$On'-1)+2));}' final_Hlist_temp > Oxygen_$On
402.     awk '{printf("%4d %12.8f %4d %12.8f %4d %12.8f\n",$('${total_co}'*('$O
   n'-1)+3),$('${total_co}'*('$On'-1)+4),$('${total_co}'*('$On'-
   1)+7),$('${total_co}'*('$On'-1)+8),$('${total_co}'*('$On'-
   1)+11),$('${total_co}'*('$On'-1)+12));}' final_Hlist_temp > proton_$On
403.     paste Oxygen_$On proton_$On > with_Oid_H_list_temp_$On
404.     paste with_Proton_bonded_Oid_H_list with_Oid_H_list_temp_$On > with_Oi
   d_H_list_temp
405.     cp with_Oid_H_list_temp with_Proton_bonded_Oid_H_list
406.     rm with_Oid_H_list_temp
407.   done
408.   rm *Oxygen_* *with_Oid_H_list_temp_*
409.
410.   ##############################
411.   ###Without O identity list###
412.
413.   #Format for proton_bonded_O_H_list
414.   #i) each row represents each step
415.   #ii) every 7-column have the information for same proton-bonded O
416.   #iii) 1st column: Proton-bonded O index
417.   #     2-3rd columns: proton index and O-H distance
418.   #     4-7th columns:
   The other 2H bonding with the O index (empty means surface O)
419.
420.   touch Proton_bonded_O_H_list
421.   for ((On=1; On<=${total_proton_num}; On++))
422.   do
423.     awk '{printf("%4d\n",$('${total_co}'*('$On'-
   1)+1));}' final_Hlist_temp > Oxygen_$On
424.     paste Oxygen_$On proton_$On > H_list_temp_$On
425.     paste Proton_bonded_O_H_list H_list_temp_$On > H_list_temp
426.     cp H_list_temp Proton_bonded_O_H_list
427.     rm H_list_temp
428.   done
429.   rm *H_list_temp_* *proton_* *Oxygen_* *.py* final_Hlist_temp
```

The file "**Proton_bonded_O_H_list"** contains all the information related to the proton-bonded O_0. Then, we need to reorganize this file to make the proton-bonded O_0 trajectories continuous.

We perform the command: **./Continueous_proton_bonded_O_list.sh**

Continueous_proton_bonded_O_list.sh

```
1. ############################################################
2. ############Reordering the proton-bonded O list############
3. ############################################################
4.
5. ############Needed input files############
6. ############i)Proton_bonded_O_H_list######
7.
8. ########################################
9. ##########Setting parameters###########
10. ########################################
11. #####Number of the protons#####
12. total_proton_num=`echo 2`  #You can modify
13.
14.
15. ####################################
16. ##########Python codes lists##########
17. ####################################
18.
19. ############################
20. ###Python_fourth.py code###
21. ############################
22. ############################################################
23. ###Reorder proton-bonded O list, making it continuous###
24. ############################################################
25. cat << EOF > Python_fourth.py
26.
27. import numpy as np
28. import math
29.
30. #Define parameters
31. proton_Num=${total_proton_num}
32. #Load data
33. data_H_list=np.genfromtxt('Proton_bonded_O_H_list', delimiter='')
34. len_file=len(data_H_list[:,0])
35.
36. #Original proton-bonded O list
37. ProtonH_index=np.zeros(shape=(len_file,proton_Num))
38. P_H=np.zeros(shape=(len_file,proton_Num*6))
39.
```

```
for i in range(0,proton_Num):
    ProtonH_index[:,i]=data_H_list[:,7*i]  #All proton-bonded O indexes
    P_H[:,(i*6):((i+1)*6)]=data_H_list[:,(7*i+1):(7*(i+1))]  #The surroundi
ng H info (incldуing proton)

#Reordering the proton-bonded O list
data_HOrder_list=np.zeros(shape=(len_file,proton_Num))
PH_up=np.zeros(shape=(len_file,(6*proton_Num)))

PH_up[0,:]=P_H[0,:]
temp_num=ProtonH_index[0,:]
data_HOrder_list[0,:]=temp_num

for ii in range(1,len_file):
    count_times=0
    for aa in range(0,proton_Num):
        temp_H=ProtonH_index[ii,aa]
        tem_sum=0
        for bb in range(0,proton_Num):
            if temp_H==temp_num[bb]:
               data_HOrder_list[ii,bb]=temp_H
               PH_up[ii,(bb*6):((bb+1)*6)]=P_H[ii,(aa*6):((aa+1)*6)]
               tem_sum=tem_sum+1
        if tem_sum==0:
            temp_PH=P_H[ii,(aa*6):((aa+1)*6)]
            temp_sumup=0
            for cc in range(0, 3):
                for ee in range(0, proton_Num):
                    for dd in range(0,3):
                        if (temp_PH[2*cc]==PH_up[(ii-
1),(6*ee+2*dd)]) and (temp_PH[2*cc] != 0):
                            temp_sumup=temp_sumup+1
                            PH_up[ii,(ee*6):((ee+1)*6)]=temp_PH
                            data_HOrder_list[ii,ee]=temp_H
                            temp_num[ee]=temp_H
            if temp_sumup != 1:
                count_times=count_times+1
                remaining_PH=temp_PH
                remaining_O=temp_H
                step_problem=ii+1
               #print("Something wrong happened with the input list at step
 {}!".format(ii+1))
    if count_times==1:
        for nn in range(0,proton_Num):
            if data_HOrder_list[ii,nn]==0:
                data_HOrder_list[ii,nn]=remaining_O
                temp_num[nn]=remaining_O
                PH_up[ii,(nn*6):((nn+1)*6)]=remaining_PH
                break
    elif count_times>=1:
        print("Please check the trajectory at step {}, at leat two protons
jump far away!".format(step_problem))
```

```
88.
89. #Format for data_HOrder_list:
90. #proton-bonded O indexes (continues)
91.
92. #Format for PH_up:
93. #3H bonded to proton-bonded O (H/proton index, H-O distance)
94. #After the first column, each 6-column corresponds to one proton-
    bonded O in data_HOrder_list
95.
96. #Save datafiles
97. np.savetxt('proton_bonded_O_reorder_list',data_HOrder_list,fmt="%s",delimit
    er='    ')
98. np.savetxt('proton_bonded_O_nearest_three_H_list',PH_up,fmt="%s",delimiter=
    '    ')
99.
100.   EOF
101.   ##############################
102.   ###End of Python_fourth.py###
103.   ##############################
104.
105.
106.   ##########################################################################
    #
107.   ##########Linux commands used to connect different Python codes#########
    #
108.   ##########################################################################
    #
109.
110.   ########################################################
111.   #####Final continuous proton-bonded O index list#####
112.   ########################################################
113.   python Python_fourth.py > Fourth_python.log
114.
115.   #Format for data_HOrder_list:
116.   #Step index, proton-bonded O indexes (continues)
117.   touch Final_proton_bonded_O_reorder_list
118.   for ((gg=1; gg<=${total_proton_num}; gg++))
119.   do
120.     awk '{printf("%6d\n",$('$gg'))}' proton_bonded_O_reorder_list > temp_O

121.     paste Final_proton_bonded_O_reorder_list temp_O > Final_proton_bonded_
    O_reorder_list_temp
122.     mv Final_proton_bonded_O_reorder_list_temp Final_proton_bonded_O_reord
    er_list
123.     rm temp_O
124.   done
125.   cat -
    n Final_proton_bonded_O_reorder_list > Final_proton_bonded_O_reorder_list_F
    inal
126.
127.   #Format for PH_up:
```

```
#Step index, 3H bonded to proton-bonded O (H/proton index, H-O distance)
#After the first column, each 6-column corresponds to one proton-bonded O in data_HOrder_list
touch Final_proton_bonded_O_nearest_three_H_list
for ((pp=1; pp<=${total_proton_num}; pp++))
do
  awk '{printf("%6d %14.10f %6d %14.10f %6d %14.10f\n",$(('$pp'-1)*6+1),$(('$pp'-1)*6+2),$(('$pp'-1)*6+3),$(('$pp'-1)*6+4),$(('$pp'-1)*6+5),$('$pp'*6))}' proton_bonded_O_nearest_three_H_list > temp_H
  paste Final_proton_bonded_O_nearest_three_H_list temp_H > Final_proton_bonded_O_nearest_three_H_list_temp
  mv Final_proton_bonded_O_nearest_three_H_list_temp Final_proton_bonded_O_nearest_three_H_list
  rm temp_H
done
cat -n Final_proton_bonded_O_nearest_three_H_list > Final_proton_bonded_O_nearest_three_H_list_Final

rm proton_bonded_O_nearest_three_H_list Final_proton_bonded_O_nearest_three_H_list Final_proton_bonded_O_reorder_list proton_bonded_O_reorder_list Final_reduced_H_list *.py*
```

The file "**Final_proton_bonded_O_reorder_list_Final**" provides all the continuous proton-bonded O_0 index trajectories. And the other file, "**Final_proton_bonded_O_nearest_three_H_list_Final**", contains the H/proton indexes (3H if the proton bonds with water to form H_3O^+ or 1H if the proton bonds with the surface-O to from -OH group) and the corresponding O-H distances. Each row corresponds to one step along the trajectories. (The details of the format for each file are explained in the relevant coding file.)

A.2 Surface redox rate constants

We will count proton transfer time along trajectories. There are several possible transferring cases: i) Proton transfer from water to another water molecule; ii) Proton

transfer from water to surface O; iii) Proton transfer from surface O to water; iv) Proton transfers from surface O to another surface O; v) Proton stays with the same water molecule; vi) Proton stays with the same surface O. The proton surface-redox reactions involved two cases here, the iii and iv. Thus, we can calculate the surface redox rate constant using the following expression:

$$rate\ constant = \frac{number\ of\ times\ for\ proton\ transfer}{Time\ period * Proton\ concentration * Area} \quad \text{(A.2.1)}$$

by performing the command: "**./Surface_redox_rate_calcu.sh"**.

Surface_redox_rate_calcu.sh

```
1. ###################################################################
2. ############calculating surface redox rate constant############
3. ###################################################################
4.
5. ############Needed input files###############################
6. ############i)Final_proton_bonded_O_reorder_list_Final######
7.
8. ########################################
9. ##########Setting parameters###########
10. ########################################
11. #####Number of the protons#####
12. total_proton_num=`echo 2`  #You can modify
13.
14. #####time per step#####
15. time_step=`echo 1`  #fs (femto second) and You can modify
16.
17. #####O indexes on Surface#####
18. ###If indexes have order
19. Sur_O_St=`echo 33`  #You can modify
20. Sur_O_En=`echo 64`  #You can modify
21. interger_SO=`echo 1`  #You can modify
22. echo "${Sur_O_St}" >> index_SO_temp
23. for ((i=${Sur_O_St}+${interger_SO}; i<=${Sur_O_En}; i+=${interger_SO}))
24. do
25.   echo ",$i" >> index_SO_temp
26. done
27. cat index_SO_temp | xargs > index_SO
28. SO_temp=(`echo $(grep "," index_SO)`)
29. SurfaceO=`echo ${SO_temp[@]} | sed 's/ //g'`
30. rm index_SO index_SO_temp
```

```
###If indexes do not have an order
#SurfaceO=(83,89,91,97,99,101,109,111,113)  #You can modify

#####O indexes in water#####
###If indexes have order
Wat_O_St=`echo 65`   #You can modify
Wat_O_En=`echo 76`   #You can modify
interger_WO=`echo 1`  #You can modify
echo "${Wat_O_St}" >> index_WO_temp
for ((i=${Wat_O_St}+${interger_WO}; i<=${Wat_O_En}; i+=${interger_WO}))   #
i+
do
  echo ",$i" >> index_WO_temp
done
cat index_WO_temp | xargs > index_WO
WO_temp=(`echo $(grep "," index_WO)`)
WaterO=`echo ${WO_temp[@]} | sed 's/ //g'`
rm index_WO index_WO_temp
###If indexes do not have an order
#WaterO=(115,117,121,122,123,126)  #You can modify

#####Unit-cell parameters#####
#The a-,b-,c-lattice directions
AxisO=(12.1003999709999999,0.0000000000000000,0.0000000000000000)  #You can
 modify
AxisT=(6.0494949460000003,10.4798920380999991,0.00000000000000)  #You can m
odify
AxisR=(0.0000000000000000,0.0000000000000000,13.0000000000000000)  #You can
 modify

#####Unit-cell C-lattice constant#####
#Without water and protons C-lattice constant
No_water_hight=`echo 9.75`  #You can modify
#With water and protons C-lattice constant
With_WP_hight=`echo 13.0`  #You can modify

#####Total number of water molecules#####
num_water=`echo ${WaterO[0]} | awk -F "," '{print NF}'`

#####Total time for the trajectory in pico seconds#####
Num_traj=`wc -l Final_proton_bonded_O_reorder_list_Final | cut -d' ' -f1`
time_period=`echo ${Num_traj}$'*'${time_step}'/'1000 | bc`  # ps (pico seco
nd)


#####################################
##########Pthon codes lists##########
#####################################

############################
###Python_fifth.py code###
############################
```

```
78. ###########################################################
79. ###Reorder proton-bonded O list, making it continuous###
80. ###########################################################
81. cat << EOF > Python_fifth.py
82. 
83. import numpy as np
84. import math
85. 
86. #Define parameters
87. proton_num = ${total_proton_num}
88. Surface_O_index = [${SurfaceO[@]}]
89. Water_O_index =[${WaterO[@]}]
90. 
91. #Load data
92. data_proton=np.genfromtxt('Final_proton_bonded_O_reorder_list_Final', delim
    iter='')
93. 
94. #Calculate the surface redox rate constants
95. len_step=len(data_proton[:,0])
96. proton_total = data_proton[:,1:(proton_num+1)]
97. print('The total steps invovled in our calculations is: ', len_step)
98. 
99. #We have the following cases:
100.   #1: ss; 2: sw; 3: ws; 4: ww; 0: no change
101.   ss_total = np.zeros(proton_num)
102.   sw_total = np.zeros(proton_num)
103.   ws_total = np.zeros(proton_num)
104.   ww_total = np.zeros(proton_num)
105.   nochange_stayW = np.zeros(proton_num)
106.   nochange_stayS = np.zeros(proton_num)
107.   count_num_proton = np.zeros(shape=(len_step-1,proton_num))
108. 
109.   for nn in range(0,proton_num):
110.       for i in range(0,len_step-1):
111.           temp_proton_cal_f = int(proton_total[i,nn])
112.           temp_proton_cal_s = int(proton_total[i+1,nn])
113.           if (temp_proton_cal_f in Surface_O_index) and (temp_proton_cal_s
    in Water_O_index):
114.               count_num_proton[i,nn] = 2
115.               sw_total[nn] = sw_total[nn]+1
116.           elif (temp_proton_cal_f in Water_O_index) and (temp_proton_cal_s
    in Surface_O_index):
117.               count_num_proton[i,nn] = 3
118.               ws_total[nn] = ws_total[nn]+1
119.           elif (temp_proton_cal_f in Surface_O_index) and (temp_proton_cal
    _s in Surface_O_index):
120.               if temp_proton_cal_f != temp_proton_cal_s:
121.                   count_num_proton[i,nn] = 1
122.                   ss_total[nn] = ss_total[nn]+1
123.               else:
124.                   count_num_proton[i,nn] = 0
125.                   nochange_stayS[nn] = nochange_stayS[nn]+1
```

```
            elif (temp_proton_cal_f in Water_O_index) and (temp_proton_cal_s in Water_O_index):
                if temp_proton_cal_f != temp_proton_cal_s:
                    count_num_proton[i,nn] = 4
                    ww_total[nn] = ww_total[nn]+1
                else:
                    count_num_proton[i,nn] = 0
                    nochange_stayW[nn] = nochange_stayW[nn]+1

        if ws_total[nn]+sw_total[nn]+ww_total[nn]+ss_total[nn]+nochange_stayS[nn]+nochange_stayW[nn] == len_step-1:
            print('\nCalculations for proton number {} are right!'.format(nn+1))
        else:
            print('\nError happened for proton number {}!'.format(nn+1))

      #print('The matrix for the transfer of proton {} is: {}'.format(nn+1, count_num_proton[:,nn]))
        print('Count  times for the transfer of proton number {} : '.format(nn+1))
        print('Surface-Surface number: {}'.format(int(ss_total[nn])))
        print('Water-Surface number: {}'.format(int(ws_total[nn])))
        print('Surface-Water number: {}'.format(int(sw_total[nn])))
        print('Water-Water number: {}'.format(int(ww_total[nn])))
        print('Stay in same water-O: {}'.format(int(nochange_stayW[nn])))
        print('Stay in same surface-O: {}'.format(int(nochange_stayS[nn])))

    ###############################################
    #Calculate the rate constant for all protons#
    ###############################################
    #Define parameters
    Avogadro_constant = 6.022140857*10**23
    one_axis = (${AxisO})
    two_axis = (${AxisT})
    three_axis = (${AxisR})
    no_water_lattice = ${No_water_hight}
    With_water_lattice = ${With_WP_hight}
    Lactice_z_change = With_water_lattice-no_water_lattice

    #The area of the surface
    def calc_area(p1, p2, p3):
            (x1, y1, z1),(x2, y2, z2),(x3, y3, z3) = p1,p2,p3
            return abs(x1*y2-x2*y1+x2*y3-x3*y2+x3*y1-x1*y3)
    area_angstrom = calc_area(one_axis, two_axis, three_axis)
    area_m = area_angstrom*(10**-10)**2

    #Total proton surface redox times
    time_total_surface_redox = sum(sw_total)
    time_redox = time_total_surface_redox/Avogadro_constant
    proton_mol = proton_num/Avogadro_constant
    fs_total_s = len_step*10**(-15)  #unit:s
```

```
172.
173.   #Proton concentration
174.   volumn = Lactice_z_change*area_m*(10**-10)  #unit m^3
175.   concentration_proton = proton_mol/volumn
176.
177.   #Water density
178.   water_density = ${num_water}/Avogadro_constant*18.0153/volumn/1000000
179.   print('\nWater density in my system (g*cm-3) is: ',water_density)
180.   #Surface redox rate constant
181.   rate = time_redox/(2*area_m)/fs_total_s/concentration_proton
182.   print('\nThe surface redox rate constant (unit: m*s-1) is: ',rate)
183.
184.   EOF
185.   ############################
186.   ###End of Python_fifth.py###
187.   ############################
188.
189.
190.   ##########################################################################
      #
191.   ##########Linux commands used to connect different Python codes#########
      #
192.   ##########################################################################
      #
193.
194.   ##########################################################################

195.   #####Performing python script and get surface redox rate constants#####

196.   ##########################################################################

197.   python Python_fifth.py > Fifth_python.log
198.
199.   rm Python_fifth.py
```

The file "**Fifth_python.log"** contains the calculated surface redox rate constant, water density, and the number of transfer processes (i, ii, iii, iv, v, vi) for each continuous proton behavior.

Supporting Information

A.S1 Formulas

Num.	Formula
A.2.1	$rate\ constant = \frac{number\ of\ times\ for\ proton\ transfer}{Time\ period * Proton\ concentration * Area}$

References

(1) Kresse, G.; Furthmüller, J. Efficient Iterative Schemes for *Ab Initio* Total-Energy Calculations Using a Plane-Wave Basis Set. *Physical review B* **1996**, *54* (16), 11169. http://dx.doi.org/10.1103/PhysRevB.54.11169.

(2) Sheppard, D.; Terrell, R.; Henkelman, G. Optimization Methods for Finding Minimum Energy Paths. *The Journal of chemical physics* **2008**, *128* (13), 134106. https://doi.org/10.1063/1.2841941.

(3) Henkelman, G.; Uberuaga, B. P.; Jónsson, H. A Climbing Image Nudged Elastic Band Method for Finding Saddle Points and Minimum Energy Paths. *The Journal of chemical physics* **2000**, *113* (22), 9901–9904. https://doi.org/10.1063/1.1329672.